Institute of Earth and Environmental Science

Analysis and Modeling of Transient Earthquake Patterns and Their Dependence on Local Stress Regimes

by

OLGA ZAKHAROVA

Cumulative dissertation

in fulfilment of the requirements for the degree of
"doctor rerum naturalium" (Dr. rer. nat.)
for the scientific discipline "Geophysics"

submitted to the
Faculty of Mathematics and Natural Sciences
University of Potsdam

December 7, 2015

Published online at the
Institutional Repository of the University of Potsdam:
URN urn:nbn:de:kobv:517-opus4-86455
http://nbn-resolving.de/urn:nbn:de:kobv:517-opus4-86455

"Now, you say,
"Oh great!, with this theory we make quantum nucleodynamics
using the pions just like Yukawa wanted to do,
and see if it works, and everything will be explained."
Bad luck."

Richard Feynman

ABSTRACT

Investigations in the field of earthquake triggering and associated interactions, which includes aftershock triggering as well as induced seismicity, is important for seismic hazard assessment due to earthquakes destructive power. One of the approaches to study earthquake triggering and their interactions is the use of statistical earthquake models, which are based on knowledge of the basic seismicity properties, in particular, the magnitude distribution and spatiotemporal properties of the triggered events.

In my PhD thesis I focus on some specific aspects of aftershock properties, namely, the relative seismic moment release of the aftershocks with respect to the mainshocks; the spatial correlation between aftershock occurrence and fault deformation; and on the influence of aseismic transients on the aftershock parameter estimation. For the analysis of aftershock sequences I choose a statistical approach, in particular, the well known Epidemic Type Aftershock Sequence (ETAS) model, which accounts for the input of background and triggered seismicity. For my specific purposes, I develop two ETAS model modifications in collaboration with Sebastian Hainzl. By means of this approach, I estimate the statistical aftershock parameters and performed simulations of aftershock sequences as well.

In the case of seismic moment release of aftershocks, I focus on the ratio of cumulative seismic moment release with respect to the mainshocks. Specifically, I investigate the ratio with respect to the focal mechanism of the mainshock and estimate an effective magnitude, which represents the cumulative aftershock energy (similar to Bath's law, which defines the average difference between mainshock and the largest aftershock magnitudes). Furthermore, I compare the observed seismic moment ratios with the results of the ETAS simulations. In particular, I test a restricted ETAS (RETAS) model which is based on results of a clock advanced model and static stress triggering.

To analyze spatial variations of triggering parameters I focus in my second approach on the aftershock occurrence triggered by large mainshocks and the study of the aftershock parameter distribution and their spatial correlation with the coseismic/postseismic slip and interseismic locking. To invert the aftershock parameters I improve the modified ETAS (m-ETAS) model, which is able to take the extension of the mainshock rupture into account. I compare the results obtained by the classical approach with the output of the m-ETAS model.

My third approach is concerned with the temporal clustering of seismicity, which might not only be related to earthquake-earthquake interactions, but also to a time-dependent background rate, potentially biasing the parameter estimations. Thus, my coauthors and I also applied a modification of the ETAS model, which is able to take into account time-dependent background activity. It can be applicable for two different cases: when an aftershock catalog has a temporal incompleteness or when the background

seismicity rate changes with time, due to presence of aseismic forces.

An essential part of any research is the testing of the developed models using observational data sets, which are appropriate for the particular study case. Therefore, in the case of seismic moment release I use the global seismicity catalog. For the spatial distribution of triggering parameters I exploit two aftershock sequences of the Mw8.8 2010 Maule (Chile) and Mw 9.0 2011 Tohoku (Japan) mainshocks. In addition, I use published geodetic slip models of different authors. To test our ability to detect aseismic transients my coauthors and I use the data sets from Western Bohemia (Central Europe) and California.

Our results indicate that: (1) the seismic moment of aftershocks with respect to mainshocks depends on the static stress changes and is maximal for the normal, intermediate for thrust and minimal for strike-slip stress regimes, where the RETAS model shows a good correspondence with the results; (2) The spatial distribution of aftershock parameters, obtained by the m-ETAS model, shows anomalous values in areas of reactivated crustal fault systems. In addition, the aftershock density is found to be correlated with coseismic slip gradient, afterslip, interseismic coupling and b-values. Aftershock seismic moment is positively correlated with the areas of maximum coseismic slip and interseismically locked areas. These correlations might be related to the stress level or to material properties variations in space; (3) Ignoring aseismic transient forcing or temporal catalog incompleteness can lead to the significant under- or overestimation of the underlying trigger parameters. In the case when a catalog is complete, this method helps to identify aseismic sources.

ZUSAMMENFASSUNG

Untersuchungen im Bereich der Erdbebennukleation, sowie der Erdbebeninteraktion und induzierter Seismizität, sind wegen des enormen Zerstörungspotenzials von Erdbeben besonders wichtig für seismische Gefährdungsanalysen.

In meiner Doktorarbeit fokussiere ich mich auf einige Eigenschaften von Nachbeben, insbesondere auf deren freigesetztes seismisches Moment in Relation zum Hauptbeben, die räumliche Korrelation zwischen der Nachbebenaktivität und der Deformationsgeschichte der Verwerfung und den Einfluss von aseismischen Transienten auf die Bestimmung von Nachbebenparametern. Ich habe einen statistischen Ansatz für die Analyse der Nachbebensequenzen gewählt. Das sogenannte *Epidemic Type Aftershock Sequence (ETAS)* Modell berücksichtigt sowohl Hintergrundseismizität als auch getriggerte Erdbebenaktivität. Für meine Zwecke habe ich zusammen mit Sebastian Hainzl zwei Modifikationen für dieses ETAS Modell entwickelt. Mittels dieser Ansätze habe ich die statistischen Parameter der Nachbebenaktivität bestimmt und Simulationen von Nachbebensequenzen durchgeführt.

Im Falle des freigesetzten seismischen Moments von Nachbeben habe ich das Verhältnis des kummulativen Moments der Nachbeben in Bezug zum Hauptbeben untersucht. Im Speziellen betrachte ich das Verhältnis in Bezug auf den Herdmechanismus des Hauptbebens und bestimme eine effektive Magnitude, welche die kummulative Nachbebenenergie darstellt (ähnlich zu Bath's Gesetz, welches den durchschnittlichen Unterschied zwischen der Hauptbebenmagnitude und der Magnitude des größten Nachbebens beschreibt). Desweiteren vergleiche ich das Verhältnis des beobachteten seismischen Moments mit den Ergebnissen von ETAS-basierten Simulationen. Dabei teste ich ein *Restricted ETAS* (RETAS) Modell, welches auf den Resultaten eines *Clock-Advance* Modells und den durch das Hauptbeben ausgelösten statischen Spannungsänderungen basiert.

Um die räumliche Variation der Trigger-Parameter zu analysieren, fokussiere ich mich in meinem zweiten Modellansatz auf das Auftreten von Nachbeben infolge von großen Hauptbeben, sowie die Verteilung von Nachbebenparametern und deren räumliche Korrelation mit ko-/post-seismischen Verschiebungen und inter-seismischer Verhakung. Zum Bestimmen der Nachbebenparameter habe ich ein modifiziertes ETAS (m-ETAS) Modell analysiert, welches die räumliche Ausdehnung des Hauptbebenbruches berücksichtigen kann. Ich vergleiche die Ergebnisse des klassischen Ansatzes mit denen des m-ETAS Modells.

Mein dritter Versuch beschäftigt sich mit dem zeitlichen Clustern der Seismizität, welche nicht nur auf Erdbeben-Erdbeben-Interaktion zurückzuführen ist, sondern auch auf eine zeitabhängige Hintergrundrate, die die Parameterabschätzung verfälschen kann. Meine Koautoren und ich haben dem ETAS Modell darum eine weitere Modifikation

hinzugefügt, welche in der Lage ist, eine zeitabhängige Hintergrundaktivität einzubeziehen. Dieses Modell kann auf zwei Fälle angewendet werden, einerseits wenn ein Erdbebenkatalog zeitlich unvollständig ist und andererzeits wenn sich die Hintergrundseismizität, durch Vorhandensein aseismischer Kräfte, zeitlich verändert.

Ein wichtiger Teil dieser Forschung ist es die entwickelten Modelle anhand von beobachteten Daten zu testen. Darum benutze ich im Falle des freigesetzten seismischen Moments einen globalen Erdbebenkatalog. Zur Bestimmung der räumlichen Verteilung von Trigger-Parametern untersuche ich zwei Nachbebensequenzen, die des 2010er Maule (Chile) Mw8.8 Erdbebens und die des 2011er Tohoku (Japan) Mw9.0 Erdbebens. Zusätzlich benutze ich publizierte geodätische Verschiebungsmodelle verschiedener Autoren. Um die Detektionsfähigkeit für aseismische Transienten zu testen, benutzen meine Koautoren und ich Daten aus West-Böhmen (Zentraleuropa) und Kalifornien.

Unsere Ergebnisse zeigen: (1) Das Verhältnis des kumulativen seismischen Moments der Nachbeben zum Hauptbeben ist von den statischen Spannungsänderung abhängig und ist maximal in Spannungsregimen dominiert von Abschiebungen, mittel für Überschiebungen und minimal für Blattverschiebungen, wobei das RETAS Modell eine gute Korrelation mit unseren Ergebnissen zeigt. (2) Die mit dem m-ETAS Modell erhaltene räumliche Verteilung von Nachbebenparametern zeigt ungewöhnliche Werte in Gebieten reaktivierter krustaler Verwerfungssysteme. Zusätzlich fanden wir heraus, dass die Nachbebendichte mit dem ko-seismischen Verschiebungsgradienten, Nachkriechen, inter-seismischer Kopplung und b-Werten korreliert. Das seismische Moment untersuchter Nachbeben ist positiv korreliert mit Bereichen maximaler koseismischer Verschiebungen und interseismisch blockierten Bereichen. Diese Korrelation könnte dem Spannungsniveau oder räumlicher Variation der Materialeigenschaften geschuldet sein. (3) Wenn man aseismische transiente Kräfte oder zeitliche Katalogunvollständigkeit ignoriert, kann das zu signifikantem Unter- oder Überschätzen der zugrunde liegenden Seismizitäts-Parametern führen. Im Fall eines kompletten Katalogs kann diese Methode helfen, aseismische Quellen zu identifizieren.

ABBREVIATIONS AND SYMBOLS

Abbreviations

ETAS	Epidemic Type Aftershock Sequence
RETAS	Restricted Epidemic Type Aftershock Sequence
m-ETAS	modified Epidemic Type Aftershock Sequence
AIC	Akaike Information Criterion
JMA	Japan Meteorological Agency
USGS	United States Geological Survey
PDE	Preliminary Determination of Epicenters
GCMT	Global Centroid Moment Tensor
CSEP	Collaboratory for the Study of Earthquake Predictability

ETAS Parameters

K	scaling factor for the number of aftershocks triggered by an event with $\Delta m = 0$
α	parameter, that shows how much the trigger potential scales with the earthquake magnitude
$K_0 = Ke^{\alpha m}$	Omori-Utsu scaling factor for the number of aftershocks or triggering potential
c	parameter, that indicates the time of an catalog incompleteness after a large event
p	aftershock parameter related to the speed of rate changes
q	aftershock rate decay with distance from the mainshock epicenter
d	catalog location error
r	aftershock branching parameter
W	aftershock weighting factor (m-ETAS model)

Variables and Constants

t	time
m	magnitude
m_m	mainshock magnitude
m_{max}	maximum magnitude
m_{min}	minimum magnitude
$m_{m,max}$	magnitude of the largest aftershock
m_{comp}	magnitude of completeness
m_{cut}	cut-off magnitude
Δm	magnitude difference $m - m_{comp}$ or $m - m_{cut}$, where $m_{cut} \geq m_{comp}$
b-value	Gutenberg-Richter b-value
β	similar to b-value of the Gutenberg-Richter law, but related to the base e, that is $\beta = ln(10)b$
N	number of earthquakes
N_a	number of aftershocks
λ	earthquake rate
μ	background rate
M	seismic moment
M_m	seismic moment of the mainshock
M_f	cumulative seismic moment of events before the mainshock
M_a	cumulative seismic moment of events after the mainshock
R	seismic moment ratio
C	correction factor for the seismic moment ratio
R_{corr}	corrected seismic moment ratio
δm_{eff}	effective magnitude difference
$m_{a,eff}$	effective magnitude of the maximum aftershock
m^*	transition magnitude (RETAS model)
D_{seis}	width of the seismogenic zone
dip	dip angle
L	rupture length
D	maximum distance for the aftershock selection
κ	magnification factor
$\mathcal{LL}$	Log-Likelihood function

LIST OF FIGURES

2.1 An example of the frequency-magnitude distribution of earthquakes. . . 6
2.2 An example of the Omori-Utsu law fit to a data set. 7
2.3 Spatial distribution of aftershocks. 8
2.4 The empirical Båth law. 9

5.1 Seismicity maps of the Maule and the Tohoku-oki aftershock sequences with coseismic slip contours. 33
5.2 Aftershock rate and cumulative number of events as a function of time for the Maule and the Tohoku-oki earthquakes. 36
5.3 Comparison of the performance of the ETAS and m-ETAS models using the AIC. 37
5.4 Maps of the magnitude of completeness, b-values and b-value uncertainties for the Maule and the Tohoku-oki aftershock sequences. 38
5.5 Distribution of the estimated m-ETAS parameters for the Maule and the Tohoku-oki aftershock sequences. 39
5.6 The estimated spatial variation of the m-ETAS parameters K_0, K, α, c, p, and TP_2 for the Maule aftershock sequence. 40
5.7 The estimated spatial variation of the m-ETAS parameters K_0, K, α, c, p, and TP_2 for the Tohoku-oki aftershock sequence. 41
5.8 Spatial distribution of seismic moment release for the Maule and the Tohoku-oki aftershock activities. 42
5.9 Aftershock density in the case of the Maule and the Tohoku-oki aftershock sequences. 43
5.10 Box plots of aftershock parameter relative uncertainties for the Maule and for the Tohoku-oki aftershock sequences. 44

6.1 The distribution of cluster numbers (PDE catalog) with respect to the magnitude of the mainshock and selection criteria. 55
6.2 Histograms of the number of clusters (PDE + CMT catalog) as a function of the rake of the mainshock and the occurrence time for different selection criteria. 56
6.3 The mean value of the magnitude difference between the mainshock and its largest aftershock for sequences with at least one aftershock. 60
6.4 The average corrected seismic moment ratio $R_{corr}(m)$ and effective magnitude difference Δm_{eff} as a function of the mainshock magnitude. 62
6.5 Dependence of b-value, m_{max}, dip and the seismic moment ratio on the rake of the mainshock. 63

7.1 Examples of tested ETAS simulations: transient triggering with smooth transient forcing and with mainshock-type aseismic forcing. 71
7.2 Inversion results for ETAS-simulations with constant and transient forcing. 73
7.3 Examples of earthquake catalogs artificially corrupted to represent realistic catalog problems. 74
7.4 Western Bohemia swarm activity: the frequency-magnitude distributions, observed magnitudes and inverted background rates as a function of time. 76
7.5 Scatter plot of estimated α-values and the spatially closest heat-flow values in California. 80

A.1 The coseismic slip models for the Maule earthquake. 102
A.2 The postseismic slip models for the Maule earthquake. 102
A.3 The coseismic slip gradient models for the Maule earthquake. 103
A.4 The interseismic coupling model for the Maule earthquake. 103
A.5 The coseismic slip models for the Tohoku-oki earthquake. 104
A.6 The postseismic slip models for the Tohoku-oki earthquake. 104
A.7 The coseismic slip gradient models for the Tohoku-oki earthquake. 105
A.8 The interseismic coupling models for the Tohoku-oki earthquake. 105

LIST OF TABLES

3.1 ETAS model modifications and their main features used in this thesis. . . 15

5.1 List of slip and coupling models related to the Maule and Tohoku-oki earthquakes. 34
5.2 The initial set of the values for the aftershock selection in the subregion A used for the m-ETAS model. 37

7.1 Characteristics and parameters of the ETAS-simulations (related to investigation of the time-dependent backround rate). 71
7.2 Estimated ETAS-parameters for synthetic catalogs with artificially removed events representing typical catalog problems. 74
7.3 Results for the estimated ETAS parameters in the case of the earthquake swarms in Western Bohemia. 77
7.4 Median values and quantiles of the estimated ETAS parameters for the 36 earthquake clusters in California. 79

CONTENTS

1 INTRODUCTION **1**

2 EMPIRICAL PROPERTIES OF BACKGROUND AND AFTERSHOCK ACTIVITY **5**

3 IMPLEMENTATION OF STATISTICAL METHODS **11**

3.1 Methods . . . 11

3.1.1 Epidemic Type Aftershock Sequence Model and its Modifications 11

3.1.2 Aftershock Seismic Moment Release Ratio and Effective Magnitude 15

3.1.3 Likelihood Function . . . 16

3.1.4 Calculation of Uncertainties . . . 17

3.2 Observational Data . . . 17

3.2.1 Catalogs . . . 18

3.2.2 Geodetic Data Sets . . . 18

4 THESIS ORGANIZATION **21**

4.1 Spatial Variation of Aftershock Parameters and Their Relation to Geodetic Slip Models for the 2010 *Mw*8.8 Maule and the 2011 *Mw*9.0 Tohoku Earthquakes . . . 21

4.2 Seismic Moment Ratio of Aftershocks with Respect to Mainshocks . . . 22

4.3 Impact of Aseismic Transients on the Estimation of Aftershock Productivity Parameters . . . 23

5 SPATIAL VARIATION OF AFTRESHOCK PARAMETERS AND THEIR RELATION TO GEODETIC SLIP MODELS FOR THE 2010 *Mw*8.8 MAULE AND THE 2011 *Mw*9.0 TOHOKU EARTHQUAKES **25**

5.1 Abstract . . . 25

5.2 Introduction . . . 26

5.3 Methods . . . 27

5.3.1 ETAS model . . . 27

5.3.2 Modified ETAS Model . . . 27

5.3.3 Combined Aftershock Parameters . . . 29

5.3.4 Log-Likelihood Function . . . 29

5.3.5 Magnitude of Completeness and b-value Calculation . . . 30

5.3.6 Spatial Aftershock Selection . . . 30

5.3.7 Estimation of Parameter Uncertainties . . . 31

5.4 Data . . . 32

5.4.1 Earthquake Catalogs . . . 32

5.4.2 Slip and coupling models derived from geodetic data . . . 34

5.5 Results . . . 34
5.5.1 Model comparison: ETAS versus m-ETAS . . . 34
5.5.2 Magnitude of Completeness and b-value . . . 35
5.5.3 Aftershock Parameter Distribution . . . 36
5.5.4 Aftershock Seismic Moment and Aftershock Density . . . 40
5.5.5 Uncertainties of the Aftershock Parameters . . . 43
5.5.6 Correlations with the Physical Properties . . . 44
5.5.7 Methods limitations . . . 48
5.6 Conclusion . . . 49

6 SEISMIC MOMENT RATIO OF AFTERSHOCKS WITH RESPECT TO MAINSHOCKS 51
6.1 Abstract . . . 51
6.2 Introduction . . . 52
6.3 Methods . . . 53
6.3.1 Observational Data . . . 54
6.3.2 ETAS Simulations . . . 55
6.3.3 Restricted ETAS Simulations . . . 58
6.4 Results . . . 59
6.4.1 Båth's Law . . . 59
6.4.2 Seismic Moment Ratio R and Effective Magnitude Difference Δm . . . 61
6.4.3 Dependence on the Focal Mechanism . . . 63
6.5 Discussion . . . 64
6.6 Conclusion . . . 65

7 IMPACT OF ASEISMIC TRANSIENTS ON THE ESTIMATION OF AFTERSHOCK PRODUCTIVITY PARAMETERS 67
7.1 Abstract . . . 67
7.2 Introduction . . . 68
7.3 Method . . . 69
7.4 Synthetic Tests . . . 70
7.4.1 Effect of Time Dependence . . . 71
7.4.2 Effect of Catalog Errors . . . 72
7.5 Application . . . 75
7.5.1 Western Bohemia Swarms . . . 75
7.5.2 California Clusters . . . 77
7.6 Discussion . . . 79
7.7 Conclusion . . . 80

8 CONCLUSION AND OUTLOOK 83
8.1 Summary of Main Conclusions . . . 83
8.1.1 Spatial Distribution of Aftershock Parameters on a Scale of One Aftershock Sequence . . . 83
8.1.2 Seismic Moment Release of Aftershocks . . . 84
8.1.3 Influence of Aseismic Forces and Different Types of Catalog Incompleteness on the Aftershock Parameter Estimation . . . 85

8.2 Suggestions for Further Work 86

BIBLIOGRAPHY **89**

APPENDIX A Slip And Coupling Models Derived From Geodetic Data **101**

ACKNOWLEDGEMENTS **107**

1

INTRODUCTION

The main principle of earthquakes occurrence is known as an elastic rebound theory and states that the stress in the crust is accumulated by tectonic loading and released by a sudden coseismic unloading (*Reid*, 1910). Though this principle was introduced more than one century ago, it is still not possible to predict the occurrence of individual events, due to our poor knowledge of crustal heterogeneities and fault interaction. In spite of the presence of the large uncertainties and leak of in-situ data from the seismicity depth, this study area remains a field of interest, due to significant life and economic losses during large earthquakes.

The energy released by large sudden destructive earthquakes are mainly built up by a tectonic loading. However, the tectonic loading is not the only mechanism of seismic event triggering. In general it is possible to classify all earthquakes based on the triggering mechanism or event-event interaction in the following way:

- **Independent events.** A particular seismic event is not affected by the previous events. In other words, the history of the seismicity does not play a role in the event nucleation. The Poisson process[1], one of the simplest mathematical models, can be applied for a description of such seismic events. Examples of independent seismic events are background seismicity[2] and seismicity induced by aseismic transient formation, such as magma intrusion (*Dieterich et al.*, 2000; *Passarelli et al.*, 2012, e.g.), fluid/gas injection in the crust (*McGarr*, 2014, e.g.) or even rainfall (*Hainzl et al.*, 2013, e.g.).

- **Dependent events.** Earthquakes are triggered by preceding events. In this case the history of the previous seismicity does play a key role in the nucleation of the events. An example of triggered earthquakes is aftershock activity. Aftershock activity can be represented by the Omori-Utsu decay and the ETAS model, which will be introduced below and is the main subject of my thesis.

Though we can easily introduce a classification of seismic events in theory, the distinction of the event type is in practice is a more difficult task (*Dahm et al.*, 2012, e.g.). For instance, a mainshock, which is determined as the largest event in a sequence, is not necessarily an independent background event, but can also be a triggered one.

In the case of triggered seismicity we have better knowledge of its features, than for the background seismicity, due to the availability of rich datasets spanning the entire

[1] Poisson process is a stochastic point process model (*Zhuang et al.*, 2012, e.g.). It represents a sequence of independent events in a certain time, space or time-space interval. The interevent time in the Poisson process has an exponential distribution.

[2] Background seismicity - the seismicity due to the tectonic loading.

duration of a sequence. For example, aftershock sequences are strongly clustered in time and space with power law characteristics. In addition, the knowledge of the mainshock rupture properties allow us to constrain with more certainty the stress changes in the area of interest, which is very often impossible for the independent events because of limited information about a stress state and stress build up by tectonic loading rate. For these reasons it is possible to revise and improve forecasts at least for the time and space dependent rate of earthquakes after the mainshock occurrence. Moreover, the history has shown the destructive power of aftershock activity, showing the importance of aftershock forecasting. Examples are the Christchurch aftershock triggered by the 2010 Darefield event in New Zealand (Canterbury sequence), and 2012 Emilia aftershock sequences in Italy (*Marzocchi et al.*, 2012, e.g.). The combination of good datasets availability, knowledge of the aftershock properties and potential the destructive power of such events, make the study of the triggered seismicity important for seismic hazard assessment.

For the investigation of aftershock sequences two basic model types are used:

- **Physical models** are built on constitutive physical laws, in particular, on the rate-and-state frictional law (*Dieterich*, 1994) and Coulomb stress changes. These models are useful to understand the physical process of seismicity triggering.

- **Statistical models** are built on empirical properties of aftershocks. These models rely on fitting of aftershock parameters of the empirical laws.

Physical and statistical approaches can be used simultaneously in so called hybrid models.

Physical models can be based on (1) Coulomb stress changes (*Stein et al.*, 1992, e.g.) or (2) Coulomb stress changes and rate-and-state frictional law (*Hainzl et al.*, 2010a; *Cattania et al.*, 2015, e.g.). Unlike the statistical models, which need only seismicity information (seismicity catalogs), physics based models require additional input. In particular, calculations of Coulomb stress changes cannot be done without the knowledge of receiver fault orientation, slip distribution on the event fault and crustal properties (for example, friction coefficient). However, this information is only partially available. Thus, in my work I will use statistical and hybrid models because they are appropriate for the goals of this study.

Statistical models, used for short-term seismicity, are based on the knowledge of the following mainshock/aftershock properties:

1. The Gutenberg-Richter relation for the frequency-magnitude distribution of earthquakes;

2. The Omori-Utsu power law for aftershock rate decay with time;

3. The productivity law, which represents an exponential increase of the aftershock number as a function of the event magnitude;

4. A spatial power law decay of the aftershock activity with distance from the mainshock epicenter.

Although, the empirical relationships of aftershock occurrence are already established, physical processes behind these laws often remain unclear. For example, several physical mechanisms were suggested to explain the Omori-Utsu law, in particular, rate-and-state dependent friction (*Dieterich*, 1994), visco-elastic response (*Hainzl et al.*, 1999, e.g.), postseismic creep (*Schaff et al.*, 1998, e.g.) and so on. However, a contribution of the known physical processes in seismicity patterns is still vague due to their overlapping time scales and their dependence on the local material properties and stress state. A statistical analysis of aftershock activities might illuminate important aspects of aftershocks interaction and a physical nature of their triggering.

In this thesis I focus on the analysis of the triggered seismicity and try to improve its statistical modeling. In particular I try to answer the following questions:

1. How are the aftershock characteristics and parameters variable in space? How are they related to the geological features of the studied area and the structural/stress heterogeneities represented by deformation data?

2. What is the relation between the energy (seismic moment) released by the aftershocks and that of the main event? How does this relation depend on the focal mechanism of the mainshock?

3. What is the influence of the catalog incompleteness and the presence of aseismic transients on estimation of the aftershock parameters? Can we get unbiased estimates, if time-dependent background rates related to aseismic process such as slowslip events or pore-pressure changes are taken into account?

At first, I briefly summarize in Chapter 2 the empirical laws of the seismicity occurrence which are the basis of the statistical models. Then in Chapter 3 I introduce the statistical models and datasets used in my research. In Chapter 4 I briefly discuss the three focuses of my research, summarizing the articles presented in the thesis and my contribution to them. Finally, Chapters 5, 6 and 7 contain the articles "Spatial variations of aftershock parameters and their relation to geodetic slip models for the 2010 Mw8.8 Maule and the 2011 Mw9.0 Tohoku earthquakes", "Seismic moment ratio of aftershocks with respect to mainshocks" and "Impact of aseismic transients on the estimation of aftershock productivity parameters", respectively. In these chapters I show how (1) the spatial distributions of aftershock parameters correlate with geodetic models, (2) the seismic moment ratio of aftershocks depends on a mainshock focal mechanism and its modeling by a hybrid model based on the static stress triggering approach, (3) and how aseismic transients as well as catalog incompleteness can significantly bias the aftershock parameter estimation, if inappropriate statistical models are used.

2

EMPIRICAL PROPERTIES OF BACKGROUND AND AFTERSHOCK ACTIVITY

Empirical laws, which describe principal mainshock and aftershock properties, are used as the basis of statistical modeling. In this chapter I describe these laws in detail.

1. **Magnitude distribution.** The frequency-magnitude distribution of earthquakes can be usually well-described by the Gutenberg-Richter law (*Gutenberg and Richter*, 1944), stating that number of events N with magnitude m is:

$$N(m \geq m_{comp}) = 10^{a-b(m-m_{comp})} = N_{tot}(m \geq m_{comp})10^{-b(m-m_{comp})}, \qquad (2.1)$$

where a is a constant related to the total number of the events (N_{tot}), b is the slope of the function in a logarithmic scale, which characterizes the fraction of the large events with respect to the small ones. The typical b-value of background and aftershock activities is around one. The meaning of the b-value will be discussed in more details in Chapter 5. In Equation (2.1) $m - m_{comp} = \Delta m$ represents the correction for the magnitude of completeness m_{comp} of the catalog, defining the magnitude threshold above which the seismic recording system is able to detect all events. The Gutenberg-Richter relation is only applicable for complete datasets ($m \geq m_{comp}$). The Gutenberg-Richter law holds for background events as well as for earthquake-triggered events. An example of the magnitude frequency distribution for one aftershock sequence in the subduction zone is presented in Figure 2.1.

2. **Time decay.** The occurrence of aftershocks and background earthquakes in time is different. Tectonic background seismicity occurs randomly in time with a constant rate which can be modeled as a Poisson process. In contrast, aftershock activity decays with time according to the empirical Omori-Utsu law (*Utsu and Seki*, 1955; *Utsu et al.*, 1995). This law represents the decrease of the aftershock rate λ with time $\Delta t = t - t_{main}$ relative to the mainshock:

$$\lambda(\Delta t) = \frac{K_0}{(c + \Delta t)^p}, \qquad (2.2)$$

where K_0, c and p are constants. The p-value determines the speed of the rate change (how fast an aftershock activity will decay with time) and has a typical value around 1. One of the c-value interpretations is a medium response time on applied stress (*Narteau et al.*, 2009). However, the c-value can also have a non-physical meaning. In particular, it represents the time, when the ability of a seis-

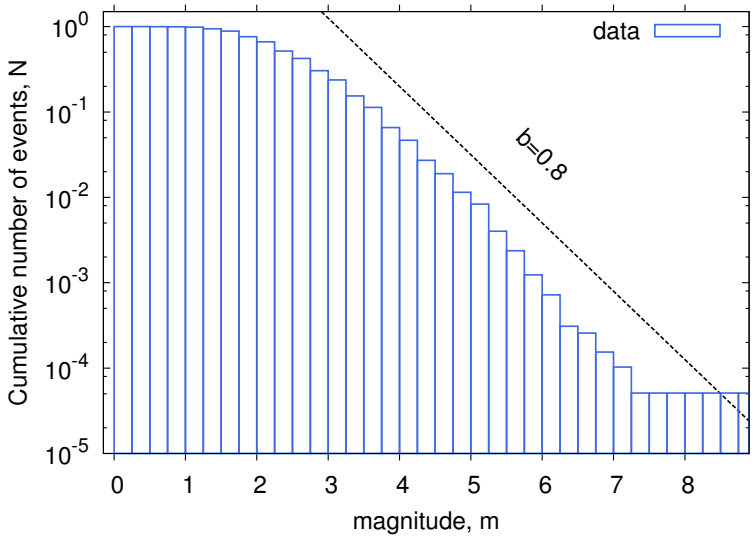

Figure 2.1: *Histogram of normalized cumulative number of events of the aftershock sequence after the 2010 Mw8.8 Maule earthquake in Chile (the mainshock is included). The Gutenberg-Richter law with $b = 0.8$ (dashed line) fits the distribution quite well. The b-value smaller than one is typical for subduction zones. The catalog is strongly incomplete for the magnitudes smaller than 2.5.*

mic network to register events with a particular magnitude after the mainshock reaches again a certain magnitude of completeness (*Kagan*, 2004). c-value is usually smaller than 1 day. From a mathematical point of view, $c \neq 0$ is necessary to avoid a singularity at a zero time. I will discuss the meaning of the K_0-value in the following paragraph. As an example, I present the fit of the Omori-Utsu law in Figure 2.2 for the case the Tohoku aftershock sequence, which occurred in the March 2011 off-shore of Japan.

3. **Triggering potential.** All types of seismic events have the potential to trigger subsequent events, which can be quantified by the two parameters K and α, $K_0 = Ke^{\alpha\Delta m}$ (*Utsu and Seki*, 1955; *Helmstetter*, 2005). The α-value shows how much the trigger potential scales with the earthquake magnitude.

   Assuming infinite aftershock triggering, the total number of triggered events is on average:

$$N = \int_0^\infty \lambda(t)dt = \int_0^\infty \frac{Ke^{\alpha\Delta m}}{(c+t)^p}dt = \frac{c^{1-p}}{(1-p)}Ke^{\alpha\Delta m}, \tag{2.3}$$

   where $p > 1$ and K-value is proportional to N.

4. **Spatial distribution.** Although, the spatial distribution of background seismicity and aftershocks is still not understood in detail, we can emphasize some of its general properties. Independent background events, which are a consequence of the static stress changes due to the tectonic plate motion, distribute almost uniformly in the areas of plate boundaries or in the collision zones. In contrast, aftershock activity strongly decays with distance from the mainshock rupture plane.

   Eneva and Pavlis (1991) show one of the first attempts to investigate the spatial

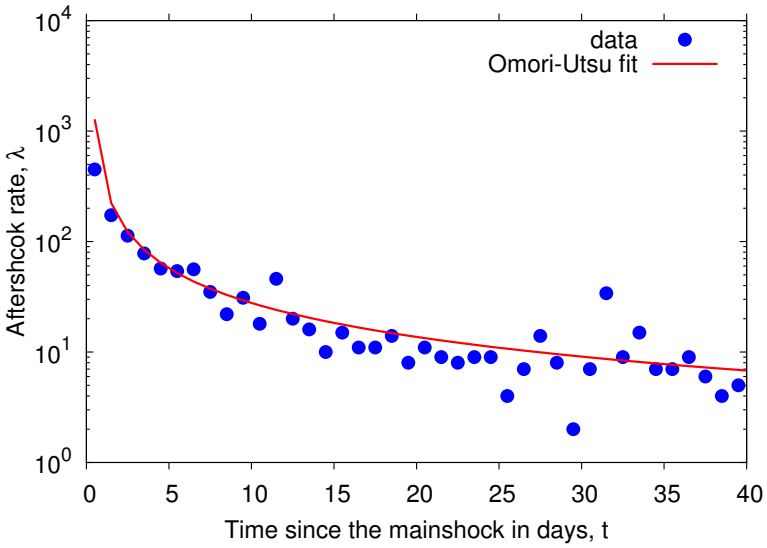

Figure 2.2: *The decay of the aftershock rate λ with time t after the 2011 Mw9.0 Tohoku mainshock, Japan (blue dots). I fit the Omori-Utsu law to this data using a simple approach of the grid search algorithm (read line). The fitted aftershock parameters are $c = 0.2$ [days], $p = 1.0$ and $K = 270.0$ [event/day]. The cut-off magnitude m_{cut} (the smallest magnitude in the used data set) is 4.5, where $m_{cut} > m_{comp}$.*

distribution of aftershocks. These authors demonstrate that aftershocks have a nonrandom spatial distribution. Later *Felzer and Brodsky* (2010), investigating the influence of the dynamic stress changes on aftershock triggering, demonstrate that the aftershock linear density decays with distance form the mainshock hypocenter according to r^{-y}, where y varies between 1.2 and 1.4. However, *Richards-Dinger et al.* (2010) showed evidence that this result was party based on erroneous aftershock selection.

More recent studies show that the aftershock density has a scale breaking at approximately one rupture length (*Lippiello et al.*, 2009, e.g). Later *Hainzl et al.* (2010b) find another break of scaling at intermediate distances (lager that one rupture length) and explain it by the effect of the free surface and the seismogenic width. Recently, *Moradpour et al.* (2014) obtained a functional form for the aftershock density decay with distance from the mainshock epicenter. This functional form accounts for a short distance aftershock increase as well as for a break in scaling at around 10 km from the mainshock epicenter (the value of 10 km is obtained using the Californian data set). The simulations of *Hainzl et al.* (2014) based on static stress triggering (*Hainzl et al.*, 2010b) and adapted for the Californian cases study confirm the suggestions of *Moradpour et al.* (2014), that the second transition is related to the seismogenic width and the free surface. Furthermore, *Hainzl et al.* (2014) show that the extended depth range gives more dramatic effect on the aftershock decay with distance than the free surface.

In general it is possible to distinguish three main scaling regimes for the probability density function of aftershocks with the mainshock epicentral distance (see Figure 2.3):

- linear aftershock density increases at *short distances* (up to one rupture length from the mainshock epicenter);
- aftershock density decreases according to $r^{1.35}$ at *intermediate distances*;
- *far field regime* shows a decay of the aftershock density with $r^{2.2}$ at the distances larger than the seismogenic width.

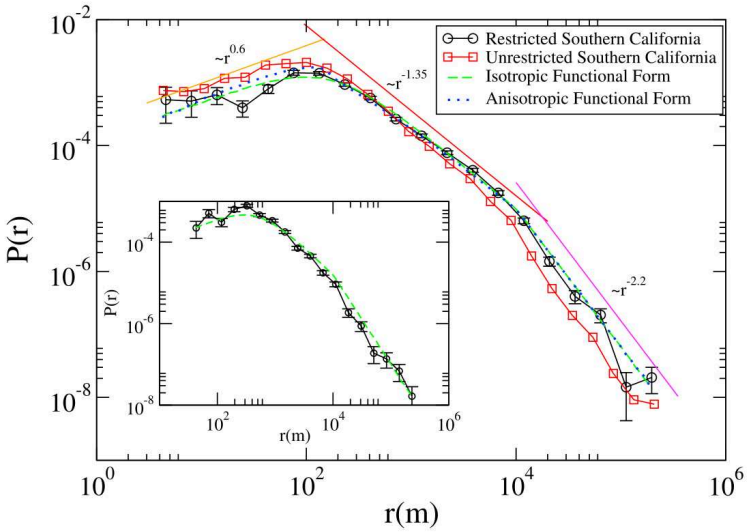

Figure 2.3: *Spatial distribution of aftershocks or aftershock density $P(r)$ using epicentral distances $r(m)$ for mainshock magnitudes in the range $3.0 < m < 4.0$ for Southern California considering all aftershocks (squares) and considering only aftershocks that occurred within one hour of their mainshock (circles). Three separate power law regimes can be identified in both cases. For comparison, the spatial distribution obtained by simulations with isotropic (dashed line) and anisotropic (dotted line) functional forms. Both agree very well with the time-restricted data. As the inset shows for mainshock magnitudes in the range $4.0 < m < 5.0$, the functional form also agrees well with the spatial distribution in other magnitude ranges.* ***Taken from Moradpour et al. (2014).***

Moreover, due to the change of the material properties change with depth from brittle to ductile, the distribution of background events as well as aftershocks has different dependence on depth than on the horizontal distance. I am focusing on the epicentral distribution in my work, ignoring the depth dependence because of the large uncertainties of the earthquake depth location.

5. **The magnitude of the largest aftershock.** A large number of aftershocks follows each big earthquake. In particular the empirical Båth law (*Bath*, 1965) states that on average the magnitude of the largest aftershock $m_{a,max}$ in an aftershock sequence is 1.2 magnitude less than the mainshock magnitude m_m:

$$m_m - m_{a,max} \approx 1.2. \tag{2.4}$$

However, the difference $m_m - m_{a,max}$ has a large deviation form the average value of 1.2 (see Figure 2.4). Using the Gutenberg-Richter law and the aftershock properties it is possible to derive the expected magnitude of the largest aftershock $m_{a,max}$ (*Helmstetter and Sornette*, 2003), which is related to Båth's law.

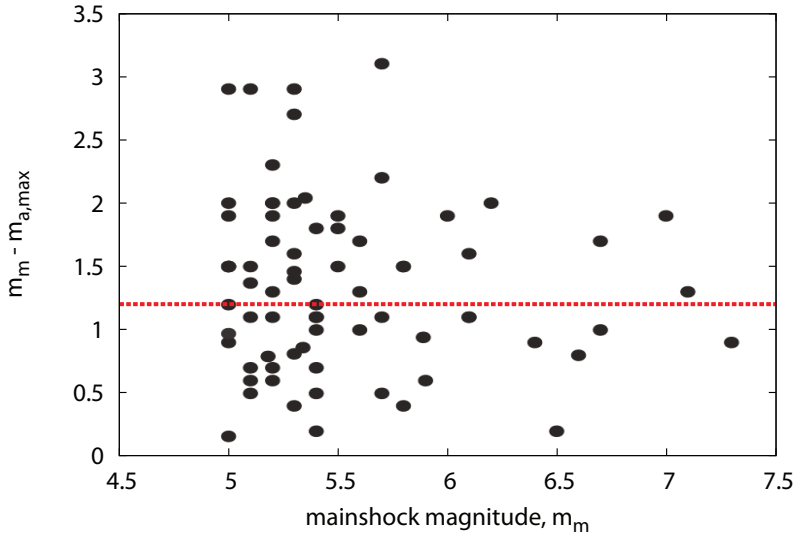

Figure 2.4: *Mainshock magnitude m_m plotted against the difference between the mainshock and the largest aftershock magnitudes $m_m - m_{a,max}$ for California-Nevada data set.* ***Taken from Felzer et al. (2002).***

The properties mentioned above can be applied in statistical models to describe earthquakes occurrences. The more properties are taken into account in the model, the more detailed will be a data fit. However, depending on the goal of the research, some of the earthquake properties can be neglected. Simple models allows to see the trend related to the particular seismicity property more clearly. In the present work I am using statistical models of different complexity, depending on my goals. I describe the models applied in this work in Section 3.1.

3

IMPLEMENTATION OF STATISTICAL METHODS

3.1 Methods

3.1.1 Epidemic Type Aftershock Sequence Model and its Modifications

There are two main groups of models that are used to represent seismicity: statistical and physics-based. Moreover, the models that include both approaches, so called hybrid models, have been recently developed as well. On one hand, statistical models use as an input the seismicity observed before the time of the interest and are based on the Gutenberg-Richer, Omori-Utsu and aftershock productivity laws (see Chapter 2). On the other hand, physical models are usually based on dynamic/static stress changes (*King et al.*, 1994) and the frictional rate-and-state dependent response of faults (*Dieterich*, 1994). Physics-based models need the additional information of the fault geometry and slip distribution of the mainshock. Both approaches, statistical as well as physics-based, have their pros and cons. Although statistical models are missing an "understanding" of ongoing physical processes, they are generally superior in explaining clustering properties (*Woessner et al.*, 2011). Thus I use in my work statistical models for data analysis. In this section I focus on the statistical Epidemic Type Aftershock Sequence (ETAS) model, its modifications and cases of their possible applications.

Classical ETAS model

The ETAS model is a powerful statistical model well-suited and applicable for sequences of seismic events. The spatial dependent ETAS model was introduced by *Ogata* (1998) and it estimates an evolution of seismicity rate λ with time t:

$$\lambda(t, \vec{x}) = \mu(\vec{x}) + \sum_{t_i<t} \frac{Ke^{\alpha \Delta m_i}}{(t - t_i + c)^p} f(\vec{x}_i, m_i), \tag{3.1}$$

where μ is a background rate due to the tectonic loading, $f(\vec{x}_i, m_i)$ is a function related to the spatial decay of aftershocks with respect to the mainshock epicenter and α, K, c and p are aftershock parameters (their meaning is discussed in Chapter 2).

It can be seen from the Equation 3.1 that the ETAS model takes into account all the basic properties of seismicity (see Chapters 1 and 2). Dependent and independent events in this model are presented by the first and the second terms in Equation 3.1, respectively. The ETAS model takes potential aftershock triggering of all earthquakes into account, independently whether they triggered or background events. Further-

more, the model assumes the independence of magnitude distribution, which means that triggered events can have a larger magnitude than its mother event. The spatial decay function $f(\vec{x}_i, m_i)$ might have different forms, the main approaches are presented in the *Ogata* (1998).

The ETAS model was successfully applied in many case studies () and has two main applications:

- parameter fitting using an existing catalog to characterize the regional properties;
- simulation of synthetic catalogs using given parameters for testing and forecasting.

In the present work we use one or both of these applications depending on the task.

ETAS model for one aftershock sequence (spatial aftershock distribution)

The classical ETAS model (Equation 3.1) takes into account aftershock decay in space as a function of the distance from the mainshock epicenter that means, it assumes an isotropic aftershock distribution. Therefore, the classical approach is valid only, if at least one of two conditions is fulfilled: (1) the mainshock rupture length can be neglected due to the large scale of the region of the interest or (2) the mainshock magnitude is small and can be well approximated by a point source. However, on a local scale, when the mainshock rupture extension cannot be represented using only the hypocenter information, the classical ETAS model is not anymore appropriate. To investigate the aftershock parameters distribution in space on a local scale, by taking into account the mainshock rupture extension, we modify the standard ETAS model for our purposes. In particular, we separate the mainshock contribution (index im) from the sum in Equation 3.1. Consequently, the modified ETAS (m-ETAS) models has the following formula:

$$\lambda_A(t) = \mu + \frac{K_0}{(t - t_{im} + c)^p} + \sum_{i:t_i<t, i\neq im} W_i \frac{K e^{\alpha \Delta m_i}}{(t - t_i + c)^p}, \tag{3.2}$$

with the aftershock weighting factor, which represents the fraction of triggered events in area A which is related to event i

$$W_i = \int_A f(\vec{x} - \vec{x}_i) dS = \int_A \frac{q}{\pi} d^{2q} (|\vec{x} - \vec{x}_i|^2 + d^2)^{-(1+q)} dS. \tag{3.3}$$

where dS shows an integration over an area. The parameters q and d are constants. In our study q and d parameters are fixed during the whole parameter inversion process. We select the standard value of 0.5 for q; the parameter d is represented by the location error of events in a catalog.

The whole set of parameters in the Equation 5.4 is related to one specific subarea A. In general all parameters in the Equation 5.4 are allowed to vary, for example, $K_0 = K_0(\vec{x})$, however, we omit these notations in order to keep a simple form of the equation. Due to the unconstrained shape of the spatial triggering function related to the mainshock, the m-ETAS model is able to represent the anisotropic distribution of aftershocks triggered directly by an extended mainshock rupture (primary aftershocks) in more efficient way than the classical ETAS.

We apply the m-ETAS model to two individual aftershock sequences, triggered by the mainshocks with the magnitude larger than 8.5. As we look at a relatively short time and relatively small area, we neglect rate changes due to tectonic loading, that is $\mu = 0$. More details and the application of the m-ETAS model can be found in Chapter 5.

RETAS - ETAS model restricted by static stress changes

Recent research of *Hainzl et al.* (2010b) shows that the number of triggered aftershocks N_a is proportional to static stress changes induced by a mainshock. In addition, N_a depends on the rupture shape, which is governed by the extension of the seismogenic layer. In particular, the results show the number of aftershocks can be presented as a function of mainshock magnitude m in the following mathematical form:

$$N_a(m) = \begin{cases} 2\frac{10^{9.1+1.5m}}{\langle M \rangle}, & \text{if } m < m^* \\ N_a(m^*)10^{1.07(m-m^*)}, & \text{if } m \geq m^* \end{cases} \tag{3.4}$$

with a transition magnitude m^* of related to the mainshock dip angle and the width of the seismogenic zone D_{seis}

$$m^* = \frac{log(\frac{D_{seis}}{4sin(dip)})^2 + 3.49}{0.91}. \tag{3.5}$$

Evidently m^* acts like a scale breaking factor for the potential number of triggered aftershocks N_a. $\langle M \rangle$ in Equation 3.4 is the average seismic moment release per earthquake, which can be estimated using catalog information (*Hainzl et al.*, 2010b) according to

$$\langle M \rangle \equiv 10^{9.1+1.5m_{min}} \frac{b}{1.5-b} \frac{10^{(1.5-b)(m_{max}-m_{min})} - 1}{1 - 10^{-b(m_{max}-m_{min})}} \text{ [Nm]}. \tag{3.6}$$

Based on these results, we develop the Restricted ETAS (RETAS) model:

$$\lambda_R(t, \vec{x}) = \mu(\vec{x}) + \sum_{i:t_i<t} \frac{N_a(m_i)}{\int_0^\infty (c+t-t_i)^{-p} dt} (c+t-t_i)^{-p} f(\vec{x}_i, m_i). \tag{3.7}$$

In essence, the term $Ke^{\alpha\Delta m}$ in the classical model (Equation 3.1) is replaced by $\frac{N_a(m_i)}{\int_0^\infty (c+t-t_i)^{-p} dt}$. In my work I applied the model only in the space-independent version which corresponds to the integrated effect in the whole space. Here we also consider that background rate μ is constant in time.

The RETAS model is able to take into account the number of aftershocks N_a according to the focal mechanism of the mainshock (dip value). I apply this model to the earthquake catalog with available focal mechanisms on a global scale and investigate the seismic moment release of the aftershocks according to mainshock rake angle (Chapter 6).

ETAS model constrained by the branching ratio

A key parameter of the ETAS model is the branching parameter which is decisive for the aftershock fraction and the model stability during simulations. In particular, the

branching parameter or branching ratio r characterizes the average number of aftershocks triggered per earthquake. According to the value of r it is possible to distinguish two main regimes of aftershock occurrence: $0 \leq r \leq 1$ - stationary regime (aftershocks decay with time or number of aftershocks remains constant) and $r < 1$ non-stationary regime (number of events explodes with time). In general the ETAS model constrained by the branching ratio has the same form as the classical ETAS model in Equation 3.1, however, parameter K_0 depends on r, that is $K_0 = f(r)$.

The branching ratio itself can be estimated using the following form:

$$r = \int_{m_{min}}^{m_{max}} \text{pdf}(m) N_a(m) dm, \tag{3.8}$$

where $N_a(m)$ is the average number of direct aftershocks per mainshock with magnitude m and $\text{pdf}(m)$ is a probability density function of earthquake magnitudes. Here we leave our choice on the doubly truncated Gutenberg-Richer distribution as the probability density function:

$$\text{pdf}(m) = \frac{\beta e^{-\beta(m-m_{min})}}{1 - e^{-\beta(m_{max}-m_{min})}} \ , \tag{3.9}$$

where $\beta = ln(10)b$.

The average number of direct aftershocks can be calculated by the integration of the aftershock number over time:

$$N_a(m) \quad = \quad K e^{\alpha(m-m_{min})} \int_0^\infty (c + t - t_i)^{-p} dt = \frac{K e^{\alpha(m-m_{min})} c^{1-p}}{p-1} \quad (p > 1) \ . \tag{3.10}$$

The branching ratio based on the magnitude dependent average number of events $N_a(m)$ and the aftershock distribution over magnitudes $\text{pdf}(m)$ is related to the ETAS model parameters as

$$r = K \frac{c^{1-p}}{p-1} \frac{\beta}{\alpha - \beta} \frac{1 - e^{(\alpha-\beta)(m_{max}-m_{min})}}{1 - e^{-\beta(m_{max}-m_{min})}}, \text{if } \alpha \neq \beta; \tag{3.11}$$

$$r = K \frac{c^{1-p}}{p-1} \frac{\beta(m_{max} - m_{min})}{1 - e^{-\beta(m_{max}-m_{min})}}, \text{if } \alpha = \beta. \tag{3.12}$$

I use the ETAS model with a branching ratio in my study for simulations only. In particular, I compare the results obtained using simulated and real catalogs in the cases of the Bath's law, effective magnitude difference and seismic moment release ratio in Chapter 6.

ETAS model with a time-dependent background rate

Parameter inversion. For aftershock parameter inversion with time dependent background seismicity, we use for simplicity a space-independent model version of Equation 3.1 and obtain:

$$\lambda(t) = \mu(t) + \sum_{t_i < t} \frac{K e^{\alpha \Delta m_i}}{(t - t_i + c)^p}. \tag{3.13}$$

The presence of a time dependent background rate $\mu(t)$ demands additional steps

for a parameter inversion (*Marsan et al.*, 2013). In particular, an iterative approach is necessary starting form parameter inversion with a constant background rate and estimate of the probability that events belong to background activity. Then $\mu(t)$ is estimated using the n-nearest neighbors. This procedure is repeated until convergence of the ETAS parameters including the background rate and the number n of nearest neighbors used for calculating $\mu(t)$ is chosen by the Akaike Information Criterion (AIC). More details of the procedure can be found in Chapter 7.

Simulations. We follow two main steps to create a synthetic catalog with time dependent background rate: (1) simulations of the time dependent background seismicity; (2) using simulated time dependent background seismicity as the input (potential mainshocks) and calculate the triggered seismicity. Strictly saying, the time dependent forcing rate consists of two main parts: a constant background rate and an additional transient background activity. During the step (1) we restrict the fraction of events related to in constant background seismicity to 30% and the time-dependent part to 70%. For the time dependent part of the simulations we apply two different background behavior: (a) background seismicity changes with a gradual onset and (b) a background rate with rapid onset followed by a subsequent decay similar to expected effects of slow slip earthquakes.

All main features of the altered ETAS models used in this work are summarized in Table 3.1.

	Application		Dependency		Seismicity
Model	simulations	parameter inversion	time	space	background rate
Classical ETAS model	✗	✓	✓	✓	$\mu = const$
ETAS model for one aftershock sequence (m-ETAS)	✗	✓	✓	✓	$\mu = const$
RETAS (ETAS model restricted by the static stress triggering)	✓	✗	✓	✗	$\mu = const$
ETAS model based on branching ratio	✓	✗	✓	✗	$\mu = const$
ETAS model with a time dependent background rate	✓	✓	✓	✗	$\mu = f(t)$

Table 3.1: *ETAS model modifications and their main features used in this study.*

3.1.2 Aftershock Seismic Moment Release Ratio and Effective Magnitude

To show what is the fraction of energy released by all aftershocks with respect to the mainshock, which triggered them, we estimate the seismic moment ratio release

$$R = \frac{M_a - M_f}{M_m}, \tag{3.14}$$

where $M_f = \sum_{i:t_i<t_m} M(m_i)$ and $M_a = \sum_{i:t_i>t_m} M(m_i)$ is the cumulative seismic moment of events before and after the mainshock in a particular time interval and M_m is the seismic moment of the mainshock. We estimate the difference $M_a - M_f$ for the correction of seismic moment related to background activity. It is possible to neglect the seismic moment release of direct foreshocks because of the low probability of foreshock occurrence (*Christophersen and Smith*, 2008, e.g.). We calculate the seismic moment release based on

its dependency on the moment magnitude m: $M(m) = 10^{9.1+1.5m}$ (*Hanks and Kanamori*, 1979). In theory seismic moment ratio estimation works well, but in practice we should deal with a magnitude of completeness, which might be high for some data sets. To take into account the input of events with magnitudes smaller than m_{comp}, we correct the seismic moment ratio by the factor

$$C(m_m) = \frac{\int_{-\infty}^{m_m} 10^{9.1+1.5m} 10^{a-bm} dm}{\int_{m_{comp}}^{m_m} 10^{9.1+1.5m} 10^{a-bm} dm} = \frac{1}{1 - 10^{-(1.5-b)(m_m - m_c)}}.$$

Further we use the corrected seismic moment ratio $R_{corr}(m_m) = C(m_m)R(m_m)$ for the estimation of an effective magnitude difference Δm_{eff}. The meaning of the effective magnitude difference is similar to the empirical Bath law, which states, that the magnitude of the largest aftershock is on average 1.2 magnitudes less than the mainshock magnitude ($\overline{\Delta m} = m_m - m_{a,max} = 1.2$). In addition, Δm_{eff} is independent of the sample bias related to the magnitude of completeness, because it takes into account the effect of events with $m < m_{comp}$. An effective magnitude difference is based on the R_{corr} and can be estimated according to

$$\Delta m_{eff} = -\frac{\log_{10}(R_{corr})}{1.5} = m_m - m_{a,eff}, \tag{3.15}$$

where

$$m_{a,eff} = \frac{\log_{10}\left[(M_a - M_f)C(m_m)\right] - 9.1}{1.5}. \tag{3.16}$$

In Chapter 6 we calculate and analyze seismic moment ratio release R and its dependency on the rake of the mainshock using the global data set, and additionally study the effective magnitude difference Δm_{eff}.

3.1.3 Likelihood Function

The likelihood function is a joint probability of events occurrence and events absence in a particular time interval $[t_i, t_i + dt)$, when $dt \to 0$ (*Ogata*, 1983):

$$\mathcal{L} = \lambda(t_1)...\lambda(t_n) e^{-\int_{t_1}^{t_2} \lambda(t)dt} ... e^{-\int_{t_{n-1}}^{t_n} \lambda(t)dt} = \prod_{i=1}^{n} \{\lambda(t_i)\} exp\left\{-\int_{t_1}^{t_n} \lambda(t)dt\right\} \tag{3.17}$$

Consequently, the Log-Likelihood function used for the ETAS parameter estimation in a general case (temporal and spatial dependencies) has the following form:

$$\mathcal{LL} = ln\mathcal{L}(\theta) = \sum_{i=1}^{n} ln\lambda_\theta(t_i, \vec{x}_i) - \int_A \int_{t_{start}}^{t_{end}} \lambda_\theta(t, \vec{x}) dt d\vec{x}. \tag{3.18}$$

To estimated the ETAS parameters we maximize the Log-Likelihood function, so called the maximum likelihood estimation (MLE), which is a common approach for

statistical models. For the problems when the MLE cannot be done analytically, it is still possible to use a numerical approach. In our case of MLE we use a numerical approach, in particular, the Davidon-Fletcher-Powell optimization algorithm (*Press et al.*, 1992). This quasi-Newton method uses a search of the Log-Likelihood function maximum based on gradient vectors.

3.1.4 Calculation of Uncertainties

Uncertainties take place in every measurement and calculation and give a possibility to determine the reliability of obtained results and derived conclusions. In addition, the knowledge of the uncertainties might provide an opportunity for better data selection. Depending on data or methods which were used for the data processing, I apply different approaches for uncertainties calculations:

- **Bootstrapping** is the estimation approach of samples properties based on a random sampling with replacement. In my study I use those samples of the global data set to calculate the standard deviation of the seismic moment release ratio, Båth's law and effective magnitude difference (Section 6.4);

- **Hessian matrix approach.** The Taylor expansion of the likelihood function in the vicinity of the maximum with the assumption, that it has the Gaussian form, allows to estimate uncertainties of the ETAS parameters. The Hessian matrix approach accounts for dependencies between parameters, which prevents the underestimation of the parameter uncertainties. I use the inverse Hessian matrix to estimate the uncertainties of individual ETAS parameters for the specific spatial location in Section 5.3, subsection "Estimation of Parameter Uncertainties";

- **Uncertainties propagation.** The estimation of the combined aftershock parameters (section 5.3) are based on the individual ETAS parameters, which creates difficulties when the uncertainties of these new parameters should be estimated. However the functional dependency between derived and individual parameters gives the possibility to estimate the uncertainty of the combined parameters by the error propagation approach (Section 5.3, subsection "Estimation of Parameter Uncertainties").

3.2 Observational Data

In this work I focus on different aspects of aftershock sequences and deal with their occurrence on different spatial scales. On the one hand, I exploit regional catalogs, geodetic inversion models and heatflow data sets, and on the other hand, I use two types of catalogs for seismicity on a global scale. In the following I provide some details of the data used in my studies.

3.2.1 Catalogs

Global seismicity

To investigate the seismic moment release of aftershocks we focus on seismicity on the global scale and use the Global Centroid Moment Tensor (GCMT) and the U.S. Geological Society Preliminary Determination of Epicenters (PDE) catalogs in a time interval between 1973 and 2011. We choose events with a magnitude of completeness of $m_{comp} = 5.0$ and with the maximal depth of 50 km. We select as the mainshocks the largest events in the catalog and apply the method of *Tahir et al.* (2012) for the foreshocks/aftershocks selection. In particular, we use the time period $[-1, +1]$ year and a maximum distance $D(m) = \kappa L(m)$ from the mainshock epicenter, where $L(m) = 10^{-2.44+0.59m}$ is the rupture length (*Wells and Coppersmith*, 1994) and κ is a magnification factor chosen in the range $\kappa = [1, 3, 5]$.

Regional seismicity

We use different regional seismicity data sets according to the task of research and data applicability. For the spatial investigation of the aftershock properties, I use catalogs of aftershock sequences of two megathrust mainshocks in Chile and Japan. Particularly, I exploit (1) the *Lange et al.* (2012) and GCMT catalogs for the sequence, which followed the Chilean 2010 Mw8.8 Maule earthquake and (2) Japanese Meteorological Agency (JMA) data set for the 2011 Mw9.0 Tohoku (Japan) aftershock activity. For the ETAS aftershock parameter fitting we use the complete time period [32.0 : 106.0] days and [7.4 : 100.0] days for Maule and Tohoku, respectively. The magnitudes of completeness for the whole catalog over these periods are 3.2 for Maule and 4.0 for Tohoku.

For the background seismicity variation in time we choose the catalogs in the areas where aseismic transients are present. In particular, we use the catalogs of the swarm activities in Western Bohemia which occurred in the years 2000 (2450 events), 2008 (2563 events) and might be triggered by CO_2 emanation (*Bräuer et al.*, 2007) and the catalog from Southern California Earthquake Data Center (SCEDC) between 1980 and 2011 (101,930 events). The Bohemian seismicity was observed by the local seismic network WEBNET and has a magnitude of completeness $m_{comp} = 0.5$. In the case of the Californian data set we select events in the area limited by $32.50^\circ - 37.00^\circ$ N and $113.58^\circ - 121.76^\circ$ W with magnitudes $m \geq 2.0$, where we applied the cluster selection introduced by *Enescu et al.* (2009). In addition, we compare obtained aftershock parameters with a heat-flow values (database of USGS).

3.2.2 Geodetic Data Sets

The geodetic inversion models are used to calculate the correlation of spatial aftershock parameters distributions with the slip amount on the mainshock fault plane (coseismic/postseismic and interseimic coupling). We are listing the geodetic data for the Maule and Tohoku earthquakes below.

- **Maule**: Coseismic slip - *Lorito et al.* (2011), *Luttrell et al.* (2011), *Moreno et al.* (2012), *Bedford et al.* (2013), *Hayes et al.* (2013); postseismic slip - Moreno (personal com-

munication, 2011), *Vigny et al.* (2011), *Bedford et al.* (2013); interseismic coupling - *Moreno et al.* (2011).

- **Tohoku**: Coseismic slip - *Yamazaki et al.* (2011), *Wei et al.* (2012), *Hoechner et al.* (2013), *Wang et al.* (2013), *Yue and Lay* (2013), *Perfettini and Avouac* (2014); postseismic slip - *Wang et al.* (2013), *Perfettini and Avouac* (2014); interseismic coupling - *Loveless and Meade* (2011) (with fixed and free trenches used for the inversion).

4

THESIS ORGANIZATION

4.1 Spatial variation of aftershock parameters and their relation to geodetic slip models for the 2010 $Mw8.8$ Maule and the 2011 $Mw9.0$ Tohoku earthquakes

The aftershock spatial distribution is important for the seismic hazard assessment. Though, there are several approximations for the aftershock distribution in space, they are applicable only for the small mainshocks on local scale or for large mainshocks, on a global scale. However, if we look at large events on a regional scale, these approaches do not work effectively. Here we allow for realistic spatial distributions of aftershocks, obtained by the modified ETAS (m-ETAS) model, which takes into account the mainshock rupture extension, and investigate the dependencies between estimated aftershock parameters and physical properties of the crust. In particular, we focus on the correlation coefficients of the spatially distributed m-ETAS parameters and independent properties in the mainshock rupture area, such as slip and interseismic coupling.

To demonstrate quantitatively that the developed m-ETAS model performs better, than the classical one, we compare them using the Akaiki Information Criteria.

Eventually, we obtain the maps of the aftershock parameters distributed in space, based on the m-ETAS estimations. We correlate aftershock parameters in each point with the corresponding spatial point of the available physical model in the mainshock region.

Applying the m-ETAS model, we analyze two aftershock sequences, which both take place in the subduction zones. One aftershock sequence occurred after the $M_w = 8.8$ magnitude mainshock in Chile (the Maule 2010 earthquake). The second earthquake sequence was triggered by the $M_w = 9.0$ mainshock occurred in the eastern off shore region of the Japanese Honshu island (the Tohoku 2011 event). For the m-ETAS parameter inversion we use 106 and 100 days of the seismicity of the Maule (Chile) and Tohoku (Japan) regions respectively.

We find that:

1. In the majority of the locations m-ETAS gives better results than the standard ETAS model.;

2. Areas of high crustal activity (Fukushima, Tohoku and Pichilemu, Maule) correspond to aftershock parameter values which are anomalous;

3. There is no clear dependency between simple individual ETAS parameters and slip amount or interseismic locking;

4. Aftershocks tend to occur in the areas of the highest coseismic slip gradient and interseismic coupling;

5. Seismic moment release is positively correlated with the coseismic slip and seismic coupling;

6. Afterslip might be an important factor for the aftershock triggering.

My contribution: *I improved the m-ETAS model, developed by Sebastian Hainzl, and tested this model. I produced and analyzed the results for the aftershock parameter distribution in space and their correlation with deformational data. I wrote the text for the article and was the correspondent author.*

This work is submitted to *Geophysical Journal International*.

Zakharova, O., S. Hainzl, D. Lange and B. Enescu (2015), Regional dependencies of seismicity parameters and physical properties of the crust, *Geophysical Journal International*, submitted.

4.2 Seismic moment ratio of aftershocks with respect to mainshocks

In this work we focus on two main purposes: (1) to investigate the seismic moment ratio between aftershocks and mainshocks and (2) to test the Restricted Epidemic Type Aftershock Sequence (RETAS) model.

To understand the seismic moment release of the aftershock we study:

- Seismic moment release ratio R of the aftershocks with respect to their mainshocks;
- Seismic moment ratio R as a function of the mainshock rake;
- The correspondent Båth law for the effective magnitude Δm_{eff}, obtained from the seismic moment ratio.

At the same time we test the hybrid RETAS model. The RETAS model is the version of the ETAS model (*Ogata*, 1998), which takes into account the scale breaking of the number of aftershocks N_a, due to the depth limitation of the seismogenic zone. This model is based on the ideas of the earthquake stress interaction and continuous tectonic loading (*Hainzl et al.*, 2010b). The number of the aftershocks N_a is connected to the tectonic loading rate through static Coulomb stress changes and a clock advance concept.

In this work we analyze the global PDE USGS and CMT catalogs. In addition, we use the synthetic catalogs simulated by the ETAS model with a different branching ratios and the RETAS model for different seismogenic width. Finally, we applied the RETAS simulations based on the information, obtained by the real catalogs.

Our analysis shows that:

1. seismic moment release of the aftershock is about 5% of the mainshock;

2. the Båth's law estimated using the seismic moment release (that is the Δm_{eff}) is stable for the whole magnitude range of the catalog;

3. seismic moment ratio R is a maximal for the normal, intermediate for the reverse and minimal for the strike-slip mainshock mechanisms;

4. the results of the RETAS model are comparable to that of the standard ETAS model in the case of rake independent simulations and performs better than the standard ETAS model, when R is analyzed with respect to the mainshock rake angle.

My contribution: *I run the simulations and the error estimation of the results. I produced the figures, wrote the text of the article and was the correspondent author. Furthermore, I performed the analysis for the revision of the manuscript in response to the reviews.*

This work was published in *Journal of Geophysical Research (Solid Earth):* Zakharova, O., S. Hainzl, and C. Bach (2013), Seismic moment ratio of aftershocks with respect to main shocks, *Journal of Geophysical Research: Solid Earth*, *118*(11), 5856–5864, doi: 10.1002/2013JB010191.

4.3 Impact of aseismic transients on the estimation of aftershock productivity parameters

The estimation of seismic activity changes especially on a short term can be very important for the seismic hazard assessment. The time dependence on short term can be characterized by the ETAS aftershock parameters and by the rate of the background activity μ. However, often these parameters are estimated wrongly. In particular, the α-value, which is related to the earthquake-earthquake interaction, is underestimated in many cases.

Here we investigate two possible reasons for the α-value underestimation: (a) the incompleteness of the used catalogs and (b) the ignoring of the background seismicity rate μ changes with time. For testing of both aforementioned problems related to the α-value underestimation, we use synthetic catalogs. Namely, for the problem (a) we introduce catalogs with different types of the incompleteness in time and for the problem (b) we simulate the catalogs using different shape of the background seismicity evolution in time.

We show that α-value underestimation due to the incomplete catalogs, can be easily avoided by the restriction of the Log-Likelihood space. In the case of time dependent background forcing, we fit the ETAS parameters using the standard ETAS model (*Ogata*, 1998) and a modified ETAS model, introduced by *Marsan et al.* (2013), which is able to take into account the background rate changes with time and find that, when the aseismic transient are presented in the catalog: (i) the standard ETAS model leads to the underestimation of the aftershock productivity parameter; (ii) the new model of *Marsan et al.* (2013) helps to obtain almost unbiased α-value; (iii) the modified ETAS can catch the background rate changes of different forms; (iv) the standard as well as the modified ETAS model perform equally well in the case of the constant background rate.

Using the obtained results for synthetic catalogs, we analyze two empirical seismic data sets, which are potentially related to aseismic transients. The first data set is a swarm activity in the Central Europe, in particular, in the West Bohemia area, the second is a clustered activity in the Southern California. In the case of the swarm activity in

Bohemia, we investigate two earthquake swarms of the years 2000 and 2008. We show that the restriction of the Log-Likelihood space to the complete catalog leads to the significant increase of the estimated α-value. Applying the ETAS model with the time-dependent background rate we establish a significant variation of the background rate with time. This is in agreement with previous observations pointing to a dominant role of impulsive fluid migration in this region. In the case of the Californian seismic activity the account for the complete Log-Likelihood space and usage of the modified model increase the estimated α-value as well. Moreover, we show a clear correlation of remaining low α-values with the areas of a high heat flow.

My contribution: *I participated in the discussion and writing of the article.*

This work was published in *Bulletin of the Seismological Society of America:* Hainzl, S., O. Zakharova, and D. Marsan (2013), Impact of Aseismic Transients on the Estimation of Aftershock productivity Parameters, *Bulletin of the Seismological Society of America, 103*(3), 1723-1732, doi: 10.1785/0120120247

5

SPATIAL VARIATION OF AFTRESHOCK PARAMETERS AND THEIR RELATION TO GEODETIC SLIP MODELS FOR THE 2010 *Mw*8.8 MAULE AND THE 2011 *Mw*9.0 TOHOKU EARTHQUAKES

Olga Zakharova[1], Sebastian Hainzl[1], Dietrich Lange[2] and Bogdan Enescu[3,4]

[1] GFZ German Research Centre for Geosciences, Potsdam, Germany
[2] GEOMAR Helmholtz Centre for Ocean Research Kiel, Germany
[3] Earth Evolution Sciences Department, Faculty of Life and Environmental Sciences, University of Tsukuba, Tsukuba, Japan
[4] Institute of Statistical Mathematics, Tohoku, Japan

Submitted to Geophysical Journal International,
14th of June 2015

5.1 Abstract

Recent development in analysis tools and deployments of the geodetic and seismic instruments give an opportunity to investigate aftershock sequences on local scales, which is important for the seismic hazard assessment. In particular, we study the dependencies between aftershock sequences properties and deformational/geological data on a scale of the rupture extension of megathrust earthquakes. For this goal we use, on one hand, published models of inter-, co- and postseismic slip and geological information and, on the other hand, aftershock parameters, obtained by fitting a modified Epidemic Type Aftershock Sequence (ETAS) model. The altered ETAS model takes into account the mainshock rupture extension and it distinguishes between primary and the secondary aftershock triggering involved in the total seismicity rate. We estimate the Spearman correlation coefficients between the spatially distributed aftershock parameters estimated by the modified ETAS model and crustal physical properties for the Maule 2010 Mw8.8 and the Tohoku-oki 2011 Mw9.0 aftershock sequences. We find that: (i) modified ETAS model outperforms the classical one, when the mainshock rupture extension cannot be neglected and represented as a point source; (ii) anomalous aftershock parameters occur in the areas of the reactivated fault systems; (iii) aftershocks, regardless of their generation, tend to occur in the areas of high coseismic slip gradient, afterslip, interseismic coupling and b-values; (iv) aftershock seismic moment releases preferentially in regions of large coseismic slip and interseismically locked areas.

5.2 Introduction

Increased spatial resolution of crustal deformation data, obtained through modern monitoring techniques, demonstrates that seismic slip is non-uniform on faults. Likewise, the interseismic coupling between plate interfaces is heterogeneous (*Chlieh et al.*, 2011; *Loveless and Meade*, 2011; *Moreno et al.*, 2011; *Scholz and Campos*, 2012; *Cheloni et al.*, 2014). One of the main factors which influences the distribution of fault slip and interseismic coupling is crustal inhomogeneity. Other factors include fluids, petrological properties of the plate interface and the pre-stress conditions of the fault system. This factors are expected to influence aftershock occurrence. Aftershock distributions are often correlated with static Coulomb stress changes (*Stein*, 1999). Although static Coulomb stress changes can explain the general distribution of aftershocks, their detailed characteristics, such as spatial features of the distribution on a smaller scale and their productivity, cannot be establish using only the Coulomb stress change approach. For instance, the percentage of the observed seismicity occurring in regions with positive calculated Coulomb stress changes in California is equal to 65% for the Landers earthquake (*Stein et al.*, 1992) and 67% for the Nothridge mainshock (*Reasenberg and Simpson*, 1992). Small scale aftershock characteristics are probably connected to the physical crust properties. For example, *Legrand et al.* (2012) and *Tormann et al.* (2015) showed that areas of strongly locked zones in Chile and along the subduction Pacific plate off Japan, respectively, correspond to small Gutenberg-Richter b-values, indicating an increase of the ratio between large and small events before the earthquake and large b-values afterwards. In agreement, *Schurr et al.* (2014) also observed a spatiotemporal anomaly of low b-values prior to the 2014 M8.2 Iquique (Northern Chile) event, suggesting that the b-value can be used as a "stress-meter" (*Schorlemmer et al.*, 2005; *Scholz*, 2015). *Narteau et al.* (2009) obtained similar results to *Schorlemmer et al.* (2005) and *Scholz* (2015), but for the case of the Omori c-value related to the response time of the aftershock activity. However, the meaning of the c-value remains controversial, because e.g. the studies of *Enescu et al.* (2009) and *Sawazaki and Enescu* (2014) show that this parameter reflects early aftershock incompleteness. *Tahir and Grasso* (2012) investigated the relation between several seismicity parameters (p- and c-values of the modified Omori law, b-value, aftershock density rate and others) and the focal mechanisms of the mainshocks. They suggest that aftershock parameters, such as p-value, can indicate to the heterogeneity of the medium. Nevertheless, the systematic analysis between a set of different aftershock characteristics and seismic slip/coupling is missing.

Here, we study the correlation between aftershock parameters (shape of the Omori law, aftershock triggering potential, b-value, seismic moment release, aftershock density) and local fault deformation data (coseismic and postseismic slip and coupling). We employ the approach of the ETAS model (*Ogata*, 1988, 2011) to investigate the relation between aftershock parameters and coseismic/postseismic slip and interseismic locking models. For that purpose, we extend the standard ETAS model to account for a complex aftershock triggering by the mainshock (related to an extended rupture with heterogeneous slip). We desire to understand whether aftershock sequence properties are correlated with the slip/frictional properties on the plate interface. We use catalogs of the Maule (*Lange et al.*, 2012), Global Centroid Moment Tensor (GCMT) and Tohoku-

oki (Japan Meteorological Agency) aftershock sequences, representing two subduction zones: Maule (Chile) - Nazca and South American plates; Tohoku-oki (Japan) - Pacific and North American plates.

5.3 Methods

5.3.1 ETAS model

The ETAS model proposed by Ogata (*Ogata*, 1988) is widely used in statistical geophysics for simulations and parameter inversions of earthquake catalogs on short time scales. As the ETAS model uses only point-information of the seismic events, the duration and extension of single earthquakes is neglected. This model describes clustering and is based on two fundamental laws of aftershocks: the temporal power-law decay (*Utsu*, 1961; *Utsu et al.*, 1995) and the exponential aftershock productivity (*Utsu and Seki*, 1955; *Helmstetter*, 2005). The empirical Omori-Utsu law describes aftershock decay in time (decrease of the aftershock rate λ) and has the following form:

$$\lambda(t) = \frac{K_0}{(\Delta t + c)^p}, \tag{5.1}$$

where Δt is the time since the mainshock. The constant c is related to the inability of the seismic network to register events directly after the mainshock (*Kagan*, 2004) or the response of the medium (*Narteau et al.*, 2009), while p represents the speed of the aftershock rate decrease, and K_0 is a constant related to the aftershock productivity. The aftershock productivity law is an exponential function of the mainshock magnitude leading to the total aftershock number N as a function of the mainshock magnitude

$$N \propto K_0 = Ke^{\alpha \Delta m}, \tag{5.2}$$

where $\Delta m = m - m_c$ (m - mainshock magnitude, m_c - completeness magnitude of the catalog) and α is a constant, which shows the scaling of the mainshock trigger potential.

The space and time dependent ETAS model includes both relations and can be written as

$$\lambda(t, \vec{x}) = \mu(\vec{x}) + \sum_{i:t_i<t} \frac{Ke^{\alpha \Delta m_i}}{(t - t_i + c)^p} f(\vec{x} - \vec{x}_i), \tag{5.3}$$

where μ is the background rate and t_i, m_i, $\vec{x}$ define the time, magnitude and location of the event with the index i in the catalog. $f(\vec{x} - \vec{x}_i)$ defines the spatial probability density function for the triggered aftershocks with respect to the current spatial point of interest. The spatial decay function is non-unique and can have different analytical forms (*Ogata*, 1988; *Kagan and Jackson*, 2000; *Console*, 2003). Later we introduce one choice of $f(\vec{x} - \vec{x}_i)$, which we use in our research.

5.3.2 Modified ETAS Model

We deal in our work only with individual aftershock sequences triggered by extended mainshock sources. The extended mainshock rupture leads to anisotropic aftershock triggering, which cannot be captured by the classical ETAS model dealing with isotropic

distributions. That is the reason why we modify the ETAS model for our needs. The modified ETAS model (m-ETAS) separates first-order or primary aftershocks, directly related to the mainshock, from all other aftershock generations (secondary aftershocks). In contrast to the mainshock, we model the spatial triggering potential of aftershocks by isotropic distributions because of the relatively small rupture extensions of the aftershocks. In addition, we subdivide the aftershock region in small subareas to account for the extension and heterogeneity of the mainshock source. In theory, accounting for the earthquake depth distribution would be useful, but the hypocenter depth information is neglected due to their relative large uncertainties. Thus we use subareas instead of subvolumes. For each subarea A, the modified model consists of three components related to the background activity μ, the direct aftershocks, and the sum of aftershock sequences triggered by foreshocks and the aftershocks themselves:

$$\lambda(t) = \mu + \frac{K_0}{(t - t_{imain} + c)^p} + \sum_{i:t_i<t, i\neq imain} W_i \frac{Ke^{\alpha \Delta m_i}}{(t - t_i + c)^p}, \tag{5.4}$$

with the aftershock weighting factor W_i which is the fraction of triggered earthquakes (related to event i) occurring in the subregion of interest A

$$W_i = \int_A f(\vec{x} - \vec{x}_i) dS = \int_A \frac{q}{\pi} d^{2q} (|\vec{x} - \vec{x}_i|^2 + d^2)^{-(1+q)} dS. \tag{5.5}$$

The isotropic triggering kernel $f(\vec{x} - \vec{x}_i)$ can be interpreted in analogy to the Omori-Utsu law. The d-value is limited by the location error of the catalog and prevents the equation 5.5 from the divergence when $\vec{x} - \vec{x}_i = 0$. The power law decay represents a long range decay, where the q-parameter shows how aftershocks attenuate with distance. To minimize the impact of location uncertainties, we abstain from using $f(\vec{x} - \vec{x}_i)$ directly and calculate the integrated effect W_i of the i-th events on the region A in equation 5.5, where W_i is normalized - the integration over the infinite area is equal to one.

In the case when aftershocks generations are not separated (standard ETAS model), we use the equation 5.3 with $f(\vec{x} - \vec{x}_i) = W_i$. Here we assume that the mainshock has a point rupture source and triggers aftershocks isotropically (that is the aftershock rate decays radially from the mainshock epicenter). The assumption of isotropy makes sense for small events or on a large scale when the earthquake data set is purely represented (for example the seismicity on a global scale with a high completeness magnitude of a catalog). Nevertheless, the radial decay of the aftershocks from the epicenter of triggering event is physically not meaningful on a local scale, because a point representation of the mainshock rupture area is clearly incorrect. To show the advantage of the developed m-ETAS model, we compare our m-ETAS results to the results obtained by the classical approach (equation 5.3). In particular, we compare the aftershock evolution of the ETAS and m-ETAS model in time and space.

In the equations 5.3 and 5.4, we assume for simplicity that all aftershocks are triggered by the mainshock or the secondary aftershocks (i.e. we set the first term $\mu = 0$), as we are looking for the aftershock sequence in a relatively short time after the mainshock. To reduce the number of parameters in both models, we set $q = 0.5$ leading to a far-field decay according to r^{-3} in agreement with static stress, and d is set to the catalog location

error, which is 1.9 and 1.0 km for Maule and Tohoku-oki respectively.

5.3.3 Combined Aftershock Parameters

We additionally calculate two combined parameters which are particularly easy to interpret. They are determined for each ETAS parameter set $\theta = \{K_0, K, \alpha, c, p\}$ corresponding to a subregion A.

Spatial density of the direct aftershocks D_1 (number of primary aftershocks per unit square):

$$\begin{aligned} D_1 &= \frac{N_{corr}}{A}\int_{t_{start}}^{t_{end}} K_0(t - t_{main} + c)^{-p}dt \\ &= \frac{N_{corr}K_0}{A(1-p)}\left[(t_{end} - t_{main} + c)^{1-p} - (t_{start} - t_{main} + c)^{1-p}\right], \end{aligned} \tag{5.6}$$

where $N_{corr} = 10^{b(m_c - m_{min})}$ is the correction for the spatially varying completeness magnitude, assuming that magnitudes are distributed according to the Gutenberg-Richter law with the estimated b-values. The times $t_{start} \geq t_{main}$ and t_{end} represent the time span for the events used for the ETAS parameter inversion by means of the maximum likelihood method (see Section 5.3.7).

General triggering potential of secondary aftershocks TP_2 for a particular aftershock magnitude m_{fixed}, minimum cut magnitude m_{cut} and time span $[0, T]$

$$TP_2 = Ke^{\alpha(m_{fixed} - m_{cut})}\int_0^T (t + c)^{-p}dt = \frac{Ke^{\alpha(m_{fixed} - m_{cut})}}{(1-p)}\left[(T + c)^{1-p} - c^{1-p}\right]. \tag{5.7}$$

In the following, we use $m_{cut} = 2.5$, $m_{fixed} = 6.0$ and $T = 1.0$ year for the Maule as well as for the Tohoku-oki aftershock analysis.

5.3.4 Log-Likelihood Function

For the ETAS parameter estimation we use the Log-Likelihood function $\mathcal{LL}$ (*Ogata*, 1983). The $\mathcal{LL}$ function has the following form:

$$\mathcal{LL} = ln\mathcal{L}(\theta) = \sum_{i=1}^{n} ln\lambda_\theta(t_i, \vec{x}_i|\mathcal{H}_{t_i}) - \int_A \int_{t_{start}}^{t_{end}} \lambda_\theta(t, \vec{x}|\mathcal{H}_t)dtd\vec{x}, \tag{5.8}$$

where $\mathcal{H}$ is an observational history up to time t, θ is the set of parameters, if $\theta = \{\theta_1, \theta_2, ..., \theta_m\}$ in the subregion A, and t_i is the occurrence time of the earthquakes $(i = 1, ..., n)$. The first term of the equation 5.8 is related to the probability that the events occur in the time intervals $[t_i, t_i + dt)$, the second term is associated with the probability of no events in the time intervals $[t_i + dt, t_{i+1})$. To obtain the best fit of the ETAS parameters during the inversion we use a likelihood estimation with Davidon-Fletcher-Powell optimization algorithm (*Press et al.*, 1992).

5.3.5 Magnitude of Completeness and b-value Calculation

We estimate the magnitude of completeness m_c using the maximum curvature procedure (*Mignan and Woessner*, 2012). Although the maximum curvature approach can underestimate the m_c in the case when data includes strong fluctuations of m_c (for example in global earthquake catalog), *Mignan et al.* (2011) show that in the case of local data sets the magnitude of completeness is correctly estimated.

Based on the estimated magnitude of completeness we calculate the b-value by the maximum likelihood method (*Aki*, 1965; *Utsu*, 1966; *Marzocchi and Sandri*, 2003):

$$b = \frac{log_{10}(e)}{\bar{m} - \left(m_c - \frac{m_{bin}}{2}\right)}, \tag{5.9}$$

where m_{bin} is the width of the magnitude bins and $\bar{m}$ is the average magnitude of events with magnitude $m \geq m_c$.

We use the minimum number of events with the maximum distance of 50 km for the m_c calculation is $N_{min} = 100$. For the b-value N_{min} is not fixed. However, the b-value uncertainties δb include the information about the number of used points ($\delta b = f(N)$, see the equation 5.15). The events are collected in the time periods $[32 : 106.0]$ days for Maule and $[7.4 : 100.0]$ days for Tohoku-oki.

5.3.6 Spatial Aftershock Selection

We use the m-ETAS model for the parameter K_{0_k}, K_k, α_k, c_k and p_k inversion in different subregions A_k of the aftershock zone ($k = 1, ..., M$). The procedure is described by the following steps:

1. Define a spatial grid, the required event number N for each grid point and the maximum allowed distance R_{max} for the ETAS estimation;
2. Calculate for each grid point (x_i, y_i) distances to all events within the radius R_{max};
3. If the number of events within R_{max} is less than N, go to the next grid point and restart with step 2;
4. Estimate a magnitude of completeness m_{c_k} for this grid point, using the events within distances of R_{max};
5. Select events above m_{c_k}. If this number is less than N, go to the next grid point and restart with step 2;
6. Calculate the b-value using equation 5.9;
7. Determine the radius R for the N nearest events above m_{c_k};
8. Estimate parameters of the m-ETAS model (equation 5.4) for A_k: K_{0_k}, K_k, α_k, c_k and p_k. All earthquakes in the catalog are used for the parameters inversion in each grid point. In particular, they give the input in the last term of the equation 5.4, where $W_{i,k}$ is small but non-zero for events occurring outside A_k;

9. Uncertainties are calculated for the obtained parameters following the procedure in section 5.3.7;

10. Continue with next grid point (step 2).

5.3.7 Estimation of Parameter Uncertainties

The estimation of the uncertainties gives the ability to quantify the quality of the estimated model parameters. To determine the magnitude of the uncertainties, we use the Taylor expansion of the log-likelihood function $\mathcal{LL}$ and the second derivatives in the vicinity of its maximum. The second derivative of the $\mathcal{LL}$ function shows its concavity - the more concave the function the better constrained is the value of the estimated parameter θ. Moreover, to be able to estimate the uncertainties of dependent parameter correctly, it is necessary to take into account the changes of all parameters simultaneously. This uncertainty can be evaluated on the basis of the Hessian matrix H.

To estimate the uncertainties of the ETAS parameters, we use the following steps:

1. Calculate the second order derivatives of the $\mathcal{LL}$ function evaluation and the Hessian matrix
$$\mathbf{H}_{i,j} = \frac{\partial^2 \mathcal{LL}}{\partial\theta_i \partial\theta_j}; \tag{5.10}$$

2. Hessian matrix inversion;

3. Error estimation according to a given confidence interval, assuming that the $\mathcal{LL}$-function can be locally approximated by a Gaussian distribution.

Specifically, we apply this algorithm to calculate the uncertainties of the correlated ETAS parameters: K_0, K, α, c and p.

We estimate the uncertainties of the combined aftershock parameters D_1 and TP_2 by the error propagation (*Morgan and Henrion*, 1990). Here the standard deviation s_f is a function $f = f(\theta_1, \theta_2, \ldots, \theta_m)$ of the m variables θ

$$s_f = \sqrt{\sum_{j=1}^{m} \left(\frac{\partial f}{\partial\theta_j} s_{\theta_j}\right)^2 + 2\sum_{j=1}^{m}\sum_{k=j+1}^{m} r_{\theta_j,\theta_k} \left(\frac{\partial f}{\partial\theta_j} s_{\theta_j}\right)\left(\frac{\partial f}{\partial\theta_k} s_{\theta_k}\right)}, \tag{5.11}$$

where s_{θ_j} is the standard deviation of the individual variable θ_j, which is obtained using the Hessian matrix approach. The correlation coefficient r_{θ_j,θ_k} is calculated based on the values at the M different grid point estimations

$$r_{\theta_j,\theta_k} = \frac{cov(\theta_j, \theta_k)}{\sigma_{\theta_j}\sigma_{\theta_k}} \tag{5.12}$$

with the covariance $cov(\theta_j, \theta_k)$ of variables θ_j and θ_k

$$cov(\theta_j, \theta_k) = \frac{1}{M}\sum_{i=1}^{M}(\theta_{j_i} - \bar{\theta}_j)(\theta_{k_i} - \bar{\theta}_k). \tag{5.13}$$

and σ_{θ_j} the standard error with $\bar{\theta}_j$ being the average value of the variable θ_j

$$\sigma_{\theta_j} = \sqrt{\frac{\sum_{i=1}^{M} (\theta_{j_i} - \bar{\theta}_j)^2}{M}}. \tag{5.14}$$

The b-value error δb is related to the confidence level interval of 95% (*Aki*, 1965)

$$\delta b = 1.96 \frac{b}{\sqrt{N}}, \tag{5.15}$$

where N is the number of events used for the b-value estimation.

5.4 Data

Due to the goal of this study, which is to elicit dependencies between spatial aftershock properties and physical models representing slip and interseismic coupling we use two different types of data sets. Particularly, we employ the aftershock point information given in earthquake catalogs, and physical models representing coseismic/postseismic slip and interseismic coupling.

5.4.1 Earthquake Catalogs

As case studies we use the Maule M_w=8.8 2010 and Tohoku-oki M_w=9.0 2011 aftershock data sets. The maps of the aftershock spatial distributions are presented in Figure 5.1 of aftershocks for the Maule and Tohoku-oki events. For both regions local earthquake catalogs based on dense local seismic networks are available together with observations from geodetic observations for the interseismic, coseismic and postseismic slip.

Maule. The Maule mainshock occurred on the 27th of February 2010 in Chile and had a moment magnitude $M_w = 8.8$. This earthquake had a bilateral rupture propagation with the hypocenter at $35.91°S$ $72.73°W$ and depth of 35 km (USGS). We use the Maule aftershock sequence catalog of *Lange et al.* (2012), which is based on up to 130 stations rapidly deployed after the mainshock. For the $\mathcal{LL}$ estimation we use the local seismicity in the time period $[t_{start} = 32.0, t_{end} = 106.0]$ days relative to the mainshock time. We set t_{start} to 32 days because the local aftershock network was not fully operable during the deployment time. For the missing days of local seismicity information we use the GCMT catalog (*Ekström et al.*, 2012).

Tohoku-oki. The Tohoku-oki megathrust event with a moment magnitude of $M_w = 9.0$ occurred on the 11th of March 2011 off-shore Japan. Similarly to the Maule event, the Tohoku-oki earthquake had a bilateral rupture (*Shao et al.*, 2011; *Yamazaki et al.*, 2011, e.g.). The coordinates of the hypocenter were $38.10°N$ $142.86°E$ with depth of 24 km. We use the seismicity catalog from the Japan Meteorological Agency (JMA) in the time span $[t_{start} = 7.4, t_{end} = 100.0]$ days for the $\mathcal{LL}$ estimation. We fix t_{start} in the case of Tohoku-oki aftershock sequence to 7.4 days due to the strong catalog incompleteness during the first days directly after the mainshock (*Lengliné et al.*, 2012). This incompleteness appears as a result of the seismic network inability to detect events with small magnitudes in the

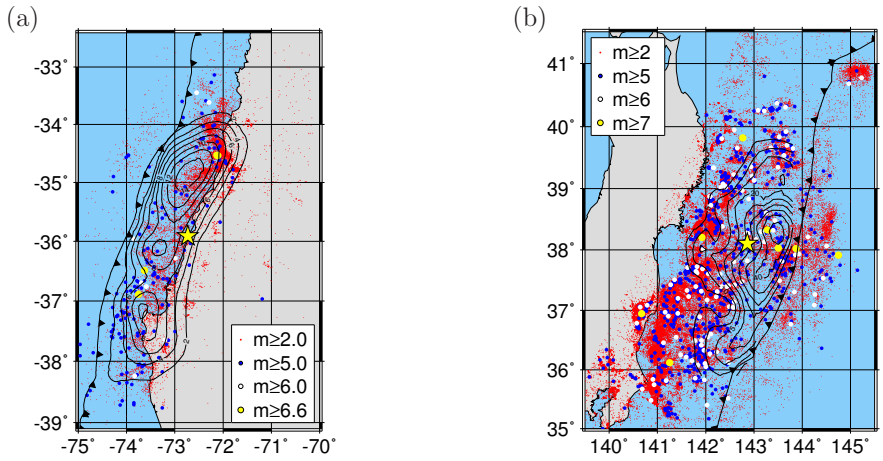

Figure 5.1: *Seismicity maps of the Maule (a) and the Tohoku-oki (b) aftershock sequences with coseismic slip contours of Moreno et al. (2012) and Wei et al. (2012), respectively. The time spans of the presented seismicity are 106 days for the Maule (Lange et al., 2012) and 100 days for the Tohoku-oki (Japan Meteorological Agency) aftershock activity since the mainshock. The mainshocks are presented by the yellow stars, black lines with triangles indicate the trenches. In the case of the Maule aftershock sequence, the two largest aftershocks with magnitudes 6.9 and 7.0 occurred almost simultaneously at the coordinates* $34.5°S$ *and* $72.1°W$.

early phase after the mainshock due to the strongly enhanced aftershock activity.

For both catalogs we use the minimum cut magnitude $m_{min} = 2.0$, consequently events with the magnitude smaller that m_{min} are not used for any calculations in our work. All events, which have magnitudes smaller than magnitude of completeness m_c, and events occurred before the time t_{start}, are used only for the aftershock rate λ calculation, but not for the parameter inversion.

We do not preselect the events according to their distance from the subduction interface in our study: we use the events on the subduction interface as well as crustal ones. The crustal seismicity and the seismicity on the subduction interface are spatially not clearly separated do not have a clear spatially separated clusters in the case of the Maule as well as the Tohoku-oki aftershock sequences. By the selection of the seismicity near the subduction interface using an arbitrary rule we might introduce artifacts, related to missing effects of earthquake-earthquake interaction between both groups. The event-event interaction in the ETAS model takes into account a stochastic nature of the aftershocks during the parameters fitting and might lead to a wrong parameter estimation. In addition, it is shown by *Kato et al.* (2011) and *Imanishi et al.* (2012), that the static stress changes induced by the Tohoku-oki earthquake theoretically is able to trigger the normal faulting events at least in the Ibaraki Prefecture. In the case of the Maule aftershocks activity *Farías et al.* (2011) shows that the triggering of the Pichelemu normal faulting cluster by the mainshock stress changes is possible as well. This shows that the ignoring the crustal seismicity, might lead to the wrong event-event interaction during the aftershock parameter inversion and incorrectly estimated aftershock parameters.

Earthquake	Physical model	Author
Maule	Coseismic slip	*Lorito et al.* (2011)
		Luttrell et al. (2011)
		Moreno et al. (2012)
		Bedford et al. (2013)
		Hayes et al. (2013)
	Postseismic	Moreno (personal communication, 2011)
		Vigny et al. (2011)
		Bedford et al. (2013)
	Interseismic locking	*Moreno et al.* (2011)
Tohoku-oki	Coseismic slip	*Yamazaki et al.* (2011)
		Wei et al. (2012)
		Hoechner et al. (2013)
		Wang et al. (2013)
		Yue and Lay (2013)
		Perfettini and Avouac (2014)
	Postseismic slip	*Wang et al.* (2013)
		Perfettini and Avouac (2014)
	Interseismic coupling	*Loveless and Meade* (2011) (fixed trench)
		Loveless and Meade (2011) (free trench)

Table 5.1: *Physical models related to the fault properties*. In the case of the Hayes et al. (2013) coseismic slip model for the Maule mainshock, we use a fault geometry with 5 patches. * We present the maps of all the listed slip models in the Appendix.*

5.4.2 Slip and coupling models derived from geodetic data

Since the models for slip and interseismic coupling are inversions of geodetic measurements of GPS land stations the models are slightly different due to the geometries, methods and inversion codes used during the inversion. In order to account for the uncertainties of the slip models we take into account a total of 19 slip and coupling models for the Tohoku-oki 2011 and Maule 2010 earthquakes which are listed in the Table 5.1. In previous, studies of the aftershock correlation with coseismic slip (*Das and Henry*, 2003; *Rietbrock et al.*, 2012; *Hayes et al.*, 2013), it was suggested that aftershocks might appear in the areas of maximum coseismic slip gradient. Therefore we also calculated the coseismic slip gradient using the available data sets by the numpy.gradient function (http://docs.scipy.org/doc/numpy/reference/generated/numpy.gradient.html). This function is based on the computation of the second order central differences. The gradient on the boundaries is estimated by the first differences or by the one-side second order differences.

5.5 Results

5.5.1 Model comparison: ETAS versus m-ETAS

The main reason why we separate the direct aftershock triggering (by introducing the local K_0 parameter) is that it better represents the spatial mainshock-aftershock triggering. In this way, the model can take the inhomogeneous triggering of complex extended

mainshock sources into account. To show this, we compare the results of both models: (i) the m-ETAS model based on the equation 5.4 and (ii) the ETAS model based on the equation 5.3. In the case of the ETAS we calculate the corresponding K_0-value using the ETAS parameters and taking into account the spatial integration component W_{imain} related to the mainshock $K_0 = W_{imain} K \exp(\alpha \Delta m_m)$. By testing and comparing these two ETAS models we are trying to answer two questions: (1) "How well does each model explain the aftershock evolution with time?" and (2) "Does the m-ETAS model represent the (primary) aftershock distribution in space significantly better than the ETAS model?".

To see the development of the seismicity in time domain, we calculate the evolution of the aftershock rate and the cumulative number of events for both models. For these estimations we use the magnitude of completeness calculated for the whole catalog. The obtained results for the Maule and Tohoku-oki aftershock sequences are shown in the Figure 5.2. Evidently, the Figure 5.2 (green lines) shows that both models produce similar results for the total aftershock rate changes (a,b) as well as for the total number of events (c,d). The output for the number of the primary aftershock is a bit different (see cyan lines, panels (c,d)). In particular, the percentage of primary aftershocks is equal to 50.2%, 46.5% for the m-ETAS model and 48.5%, 46.7% for the ETAS in the case of the Maule and Tohoku-oki aftershock sequences, respectively. For both sequences, the $\mathcal{LL}$ value is larger for the m-ETAS model, than for the ETAS one. As a consequence the m-ETAS represents the time evolution of aftershock activity better, than the ETAS.

The results in the Figure 5.3 show that for the Maule case the m-ETAS model performs in 76% better than the ETAS and for the Tohoku-oki case in 55%. These results demonstrate, that in general m-ETAS model significantly improves the spatiotemporal fit.

5.5.2 Magnitude of Completeness and b-value

The spatial distributions of the m_c and b-values are presented in the Figure 5.4. We find, that the estimated magnitude of completeness varies significantly in space, between 2.0 and 3.4 for the Maule and between 2.0 and 4.3 for the Tohoku-oki. For both investigated aftershock sequences largest uncertainties m_c are found close to the trench. While we use the local magnitude of completeness values for the inversion of local parameters, we set m_c to 3.2 and 4.0 for the parameters inversion of the whole catalog.

The b-value spatial variation and its standard deviation are shown on the Figure 5.4 panels (c,e) for the Maule and (d,f) for the Tohoku-oki aftershock sequences. In the case of the Maule data set the b-value is relatively large (up to 1.0) in the northern part of the fault and relatively small (down to 0.4) in the southern rupture area. For the Tohoku-oki earthquake, the maximum b-value (up to 1.4) occurs near the trench. Such a positive correlation may indicate that the high b-values after the Tohoku-oki mainshock represent a strong stress release in the mainshock region (*Tormann et al.*, 2015), consistent with the almost complete stress drop reported for the megathrust. The western part of the fault has generally low to intermediate b-values (around 0.7). The b-values estimated for the whole Maule and Tohoku-oki aftershock sequences are 0.76 ± 0.03 and 0.83 ± 0.03 respectively. Obtained b-values are smaller than 1.0, which is typical for subduction

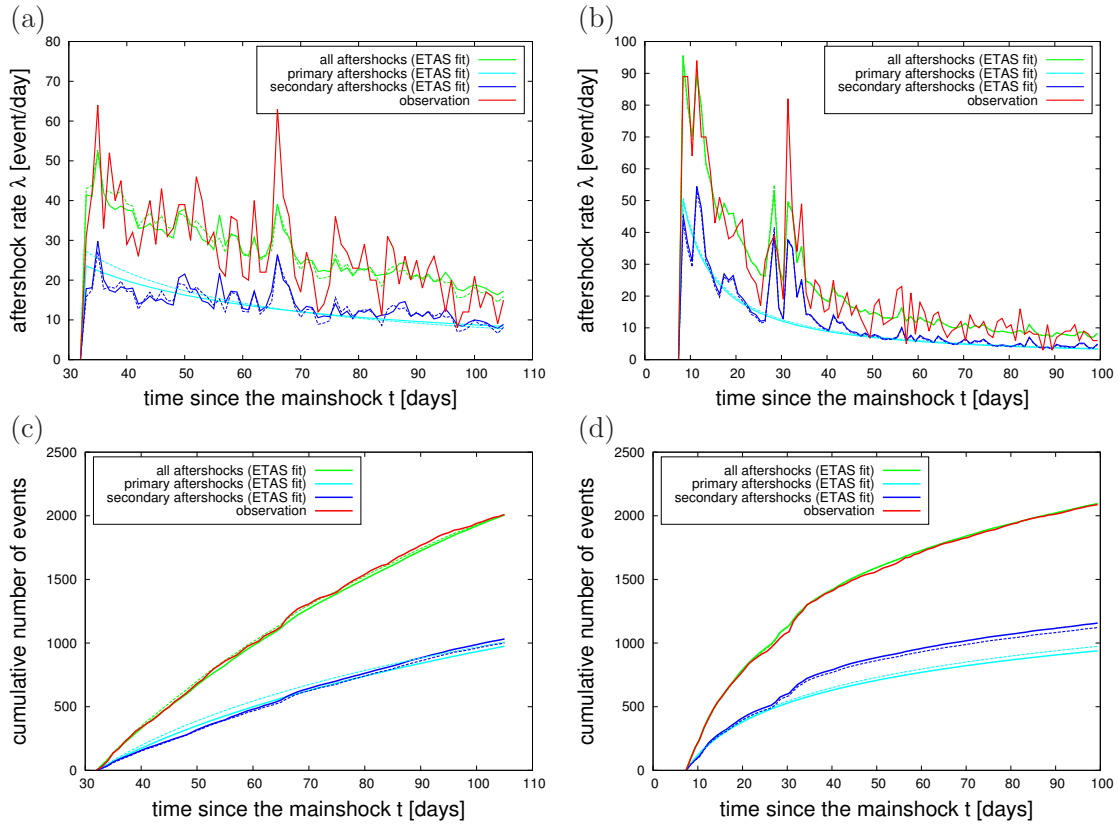

Figure 5.2: *The upper panel represents the aftershock rate as a function of time for the (a) Maule 2010 Mw8.8 and (b) Tohoku-oki 2011 Mw9.0 earthquake sequences. The lower panel shows a cumulative number of aftershocks (c) for the Maule and (d) for the Tohoku-oki aftershock sequences. In all plots red lines indicate the observed values. Green lines shows the estimated values for the total number of aftershocks, blue and cyan lines correspond to the primary and secondary aftershock activity values based on the inverted ETAS parameters respectively, where solid lines correspond to the case of ETAS model and dashed lines represent the result of the m-ETAS model.*

zone thrust events (*Schorlemmer et al.*, 2005).

5.5.3 Aftershock Parameter Distribution

Using the estimated m_c, we inverted the parameters of the m-ETAS model for both aftershock sequences. In the Table 5.2 we specify the values used for the aftershock selection. Although we show the results only for $N = 250$ (Maule) and $N = 350$ (Tohoku-oki), we calculated the estimations for four cases ($N = 150$, $N = 250$, $N = 350$ and $N = 450$) and chose the optimal solution according to the uncertainties values (see Sections 5.3.7 and 5.5.5).

The resulting spatial m-ETAS parameters are presented in the Figures 5.5 (scatter plots) and 5.6, 5.7 (parameter distributions in space). Figure 5.5 shows that K and α estimations are dependent due to their mathematical anticorrelation (see equation 5.2); and p-values are constrained, but slightly correlated with K_0, K and c. The scaling factor of the primary aftershocks, K_0, shows values in the range of 0-10^6 for the Maule and 0-10^4 for the Tohoku-oki case. Nonetheless, the largest part of the K_0-values are in the

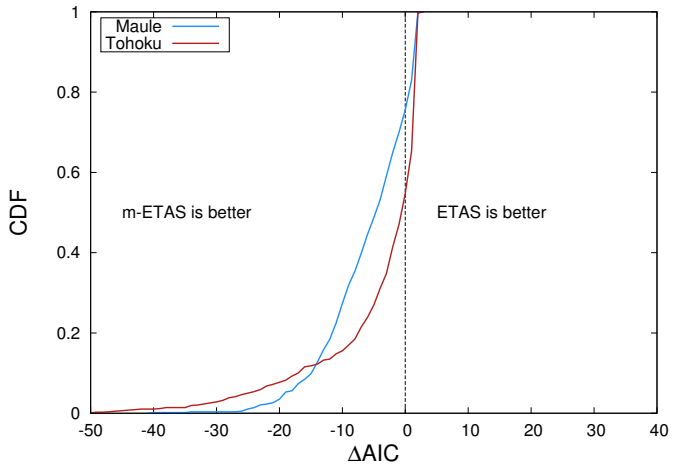

Figure 5.3: *Comparison of the results, obtained for the the spatially distributed aftershock parameters using the ETAS and m-ETAS models, presented as a cumulative distribution function (CDF) of the difference between Akaike Information Criteria* $\Delta AIC = AIC_{m\text{-}ETAS} - AIC_{ETAS}$. *Negative* ΔAIC *values mean that the model fit of the m-ETAS is superior.*

Parameter	Maule	Tohoku-oki
R_{max} [km]	50	50
N [events]	250	350
m_{cutLL} (for the whole catalog)	3.2	4.0
m_{cutLL} (for the subregions)	m_c estimated locally	m_c estimated locally
t_{start} [days]	32.0	7.4
t_{end} [days]	106.0	100.0

Table 5.2: *The initial set of the values for the aftershock selection in the subregion A. The mainshock time is set to zero.*

range of 10^1-10^2 for the Tohoku-oki and around $10^2 - 10^3$ for the Maule sequence. The corresponding scaling factor of the secondary aftershocks is K. However, it is difficult to compare K and K_0, because K_0 implicitly includes K and α-values in combination with the mainshock magnitude. The K-values have a lower boundary of zero for both earthquakes. These K-value distributions has the majority of values between 10^{-3} and 10^{-1}. The α-values referring to the magnitude dependence of the triggering potential of the secondary aftershocks have a range from 0 to 5.0 for Maule and from 0 to 5.5 for Tohoku-oki with the majority between 0.5 and 2.5. The Omori p-values, related to decay rate of the aftershock activity, scatter between 0.5 and about 3.7 for the Tohoku-oki event and 3.0 for the Maule one. Nevertheless, the mode values of the distributions are in both cases close to 1.0 and p-value distributions are well constrained with a small variability over the space. For both aftershock sequence the c-value distribution has a mode value of 10^{-2} days and a range between 10^{-6} and 10^2 days. Large c-values (larger than 1) may indicate that the aftershock rate is constant and not significantly decreasing or that seismicity was activated with some delay. The TP_2-values referring to the theoretical estimation of the number of events, triggered by an aftershock of magnitude 6.0 have mode values of about 10 events for the Maule as well as for the Tohoku-oki case.

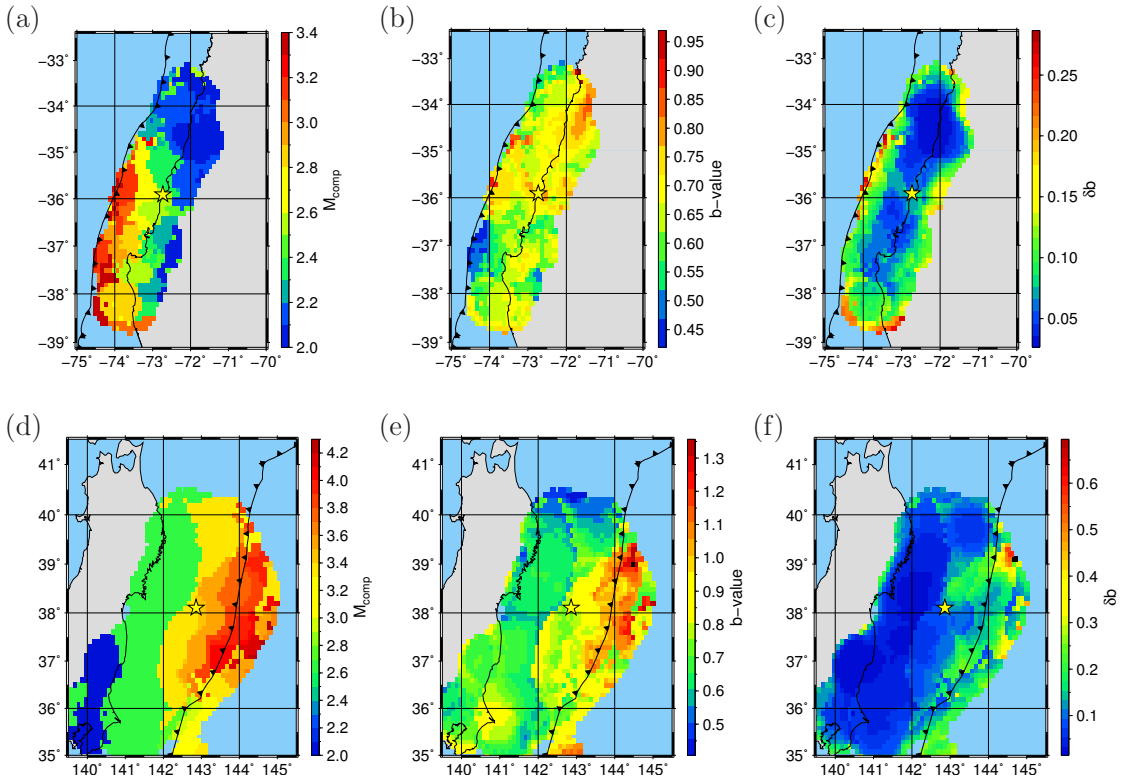

Figure 5.4: *Maps of the magnitude of completeness (a, d), b-value (b, e) and b-value uncertainties δb (c, f) for the Maule and Tohoku-oki aftershock sequences, respectively. Yellow stars indicate mainshock epicenters, black lines with triangles show the trenches.*

Overall, the spatial parameter distributions in the Maule case show four "anomalous" regions:
(1) on-shore area near the coastline between Arauco and Tumbes Peninsulas at 37°S (all parameters);
(2) on- and off-shore areas around 35.0°S,72.0°W (all parameters);
(3) the region to the north from 34.2°S latitudinal line (K_0, α, p and c-values);
(4) region to the south from the mainshock (K and α).

In particular, region (1) at latitudes of the Arauco Peninsula is characterized by complex geology and shows significant crustal faulting (*Melnick et al.*, 2006, 2012). Anomaly (2) is in the Pichilemu normal fault zone (*Melnick et al.*, 2012; *Aron et al.*, 2014, e.g.) which hosted significant normal faulting activity (*Agurto et al.*, 2012) in the continental crust (e.g. *Lange et al.*, 2012). The Pichilemu seismicity cluster aligned offshore develops into an splay fault (*Lieser et al.*, 2014) which was active during the postseismic phase of the Maule 2010 event (3).

Probably, the spatial distribution of ETAS parameters can indicate high/low differential shear stress, stress heterogeneity, variations of pore pressure or coefficient of friction (e.g. *Parsons et al.*, 1999; *Toda*, 2002).

Due to the fact that we have incomplete catalogs during first several days for both catalogs, we should be careful with the c-value interpretation. In particular we know two

common interpretations of c-value: (a) it might show the incompleteness of the catalog due to the disability of the seismic station to register events with small magnitudes

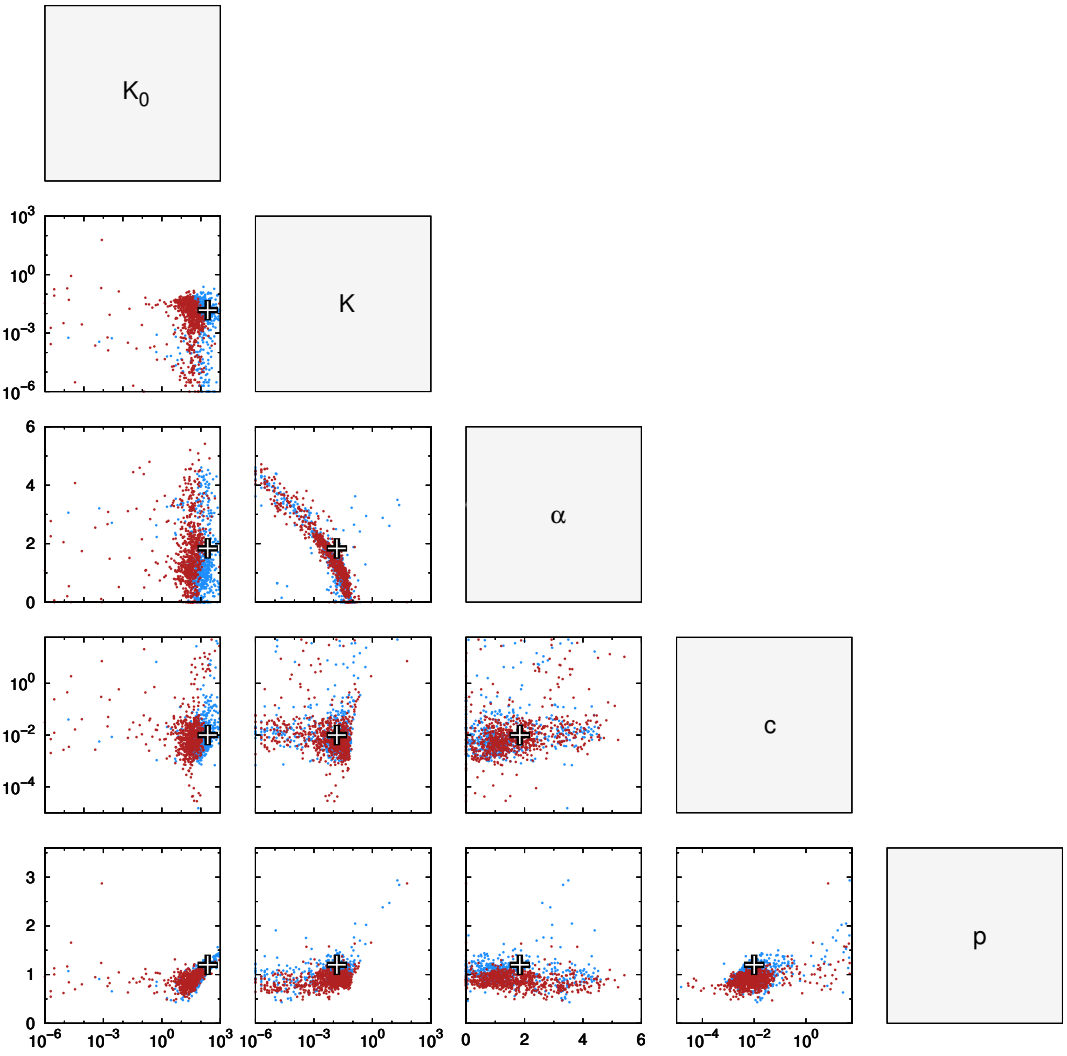

Figure 5.5: *Distribution of the estimated m-ETAS parameters. Blue points refer to the Maule, red points to the Tohoku-oki aftershock sequences. White crosses show the standard parameter values:* $K = 0.015$, $\alpha = 1.84$, $c = 0.01$, $p = 1.2$ *and* $K_0 = 224$.

and (b) it might point to some crustal properties, for example, coefficient of friction or elasticity of the material. As we do not use the first few days of seismicity for the local parameter inversion (for Maule $t_{start} = 32$ and for Tohoku-oki $t_{start} = 7.4$ days), we can exclude interpretation (a) in our case. During the ETAS parameter inversion we assume that c-value is the same for all events in the considered region and independent on the magnitude of the triggering event. That is why in our particular case the local c-values should point to the medium response. For example, the high c-value (see map in Figure 5.6e) could point to the low coefficient of friction due to the preexisting faults or due to the low differential shear stress (*Narteau et al.*, 2009) or it might be related to

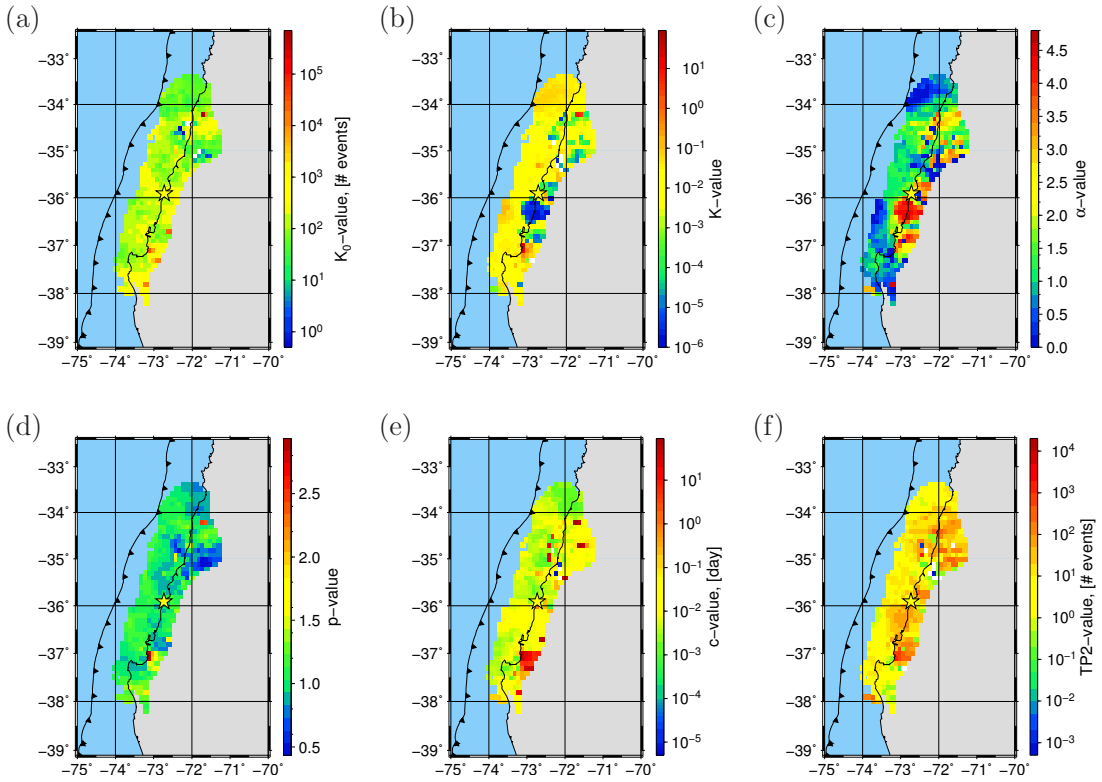

Figure 5.6: *The estimated spatial variation of the m-ETAS parameters K_0, K, α, c, p, and TP_2 for the Maule aftershock sequence. Initial conditions of the approach can be found in the Table 5.2. The white points on the maps represent zero values, if logarithmic scaled is applied. Yellow star indicates mainshock epicenter, black line with triangles shows the trench position.*

seismicity triggered by fluid migration, induced by coseismic static stress changes (*Hill and Prejean*, 2007; *Shimojo et al.*, 2014). A correspondence of region (3) to faults can not be determined due to the lack of available geological data. The region (4), existing only for the case of K and α parameters, might be an artifact due to the high correlation of these parameters.

In the case of the Tohoku-oki earthquake, we have geological information mostly for the on-shore areas. Consequently, we can only interpreted the "anomalous" parameters on the north from the Boso peninsula (approximate coordinates are $36.5°N$, $140.5°E$). This area coincides with the Tanakura Tectonic Line (*Saito*, 1992).

5.5.4 Aftershock Seismic Moment and Aftershock Density

Based on the catalog data and m-ETAS parameter estimations, we additionally calculate some physically meaningful properties, in particular, the seismic moment release M_0 and aftershock density D_{12} related to $m_{min} = 2.0$. The seismic moment distribution is calculated in the time interval $(0.0, t_{end}]$ (excluding the mainshock). We use again the maximum distance of 50 km from the grid point, however, the number of required events N is fixed to 100. We assume that seismic moment is concentrated at the aftershock epicenter. The information of the whole catalog is used. The seismic moment is

normalized according to the area of the aftershock occurrence A, so M_0 is an estimate of the seismic moment density.

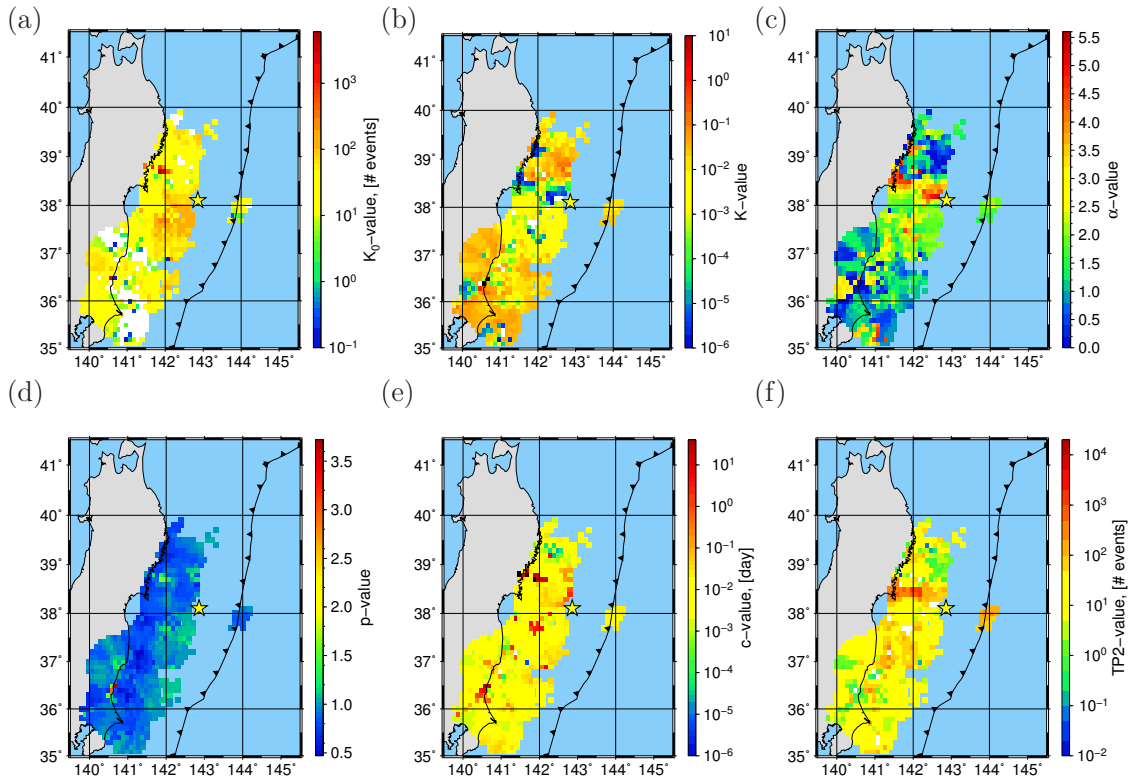

Figure 5.7: *The same as Figure 5.6 but now for the Tohoku-oki aftershock sequence.*

The resulting maps are shown in the Figure 5.8 for the Maule and the Tohoku-oki events. They indicating that the maximum seismic moment density M_0 locates in the areas of the largest aftershocks. The input of aftershocks with small magnitudes does not play a significant role with respect to the input of events with large magnitudes (*Zakharova et al.*, 2013). For this reason potential incompleteness for smaller magnitude events is insignificant and we used the whole catalogs including the smallest events for the seismic moment estimation.

For the total aftershock density D_{12} estimation, we count the number of aftershocks N with $m \geq m_c$ for each spatial point. By using the estimated spatial distribution of the magnitude of completeness m_c and the b-value, we correct for the number of aftershocks between m_{min} and m_c applying the Gutenberg-Richter law. In particular

$$D_{12}(m > m_{min}) = \frac{N10^{b(m_c - m_{min})}}{A}. \tag{5.16}$$

Based on the total (D_{12}) and primary (D_1) aftershock density we can estimate the density of the secondary aftershock D_2 per unit area as

$$D_2 = D_{12} - D_1. \tag{5.17}$$

The aftershock density distribution maps in Figure 5.9 show that the spatial distribution of the aftershock density is similar regardless of the aftershock order, but in both cases the maximal aftershock density of primary aftershocks D_1 is smaller than for the secondary one D_2. We calculate the percentage of the particular aftershock generation by summing the input of each point and dividing it on total number of aftershocks regardless to their generations. For example, in the case of primary aftershock activity the formula looks like $\frac{\sum_i D_{1i}}{\sum_i D_{12i}} 100\%$. Here the contribution of the primary aftershocks 26% and secondary events 74% for the Maule and 15% and 85% for the Tohoku-oki sequences. However, the input of the primary and the secondary aftershocks is approximately the same, when the spatial aftershock distribution is ignored and the ETAS parameters are inverted using only occurrence time of all the events in the catalog, that is $W_i = 1$. (see Figure 5.2). This shows that the ETAS estimations, based only on the time information, could introduce significant bias for the inverted parameters and, consequently, to the contribution of primary and the secondary seismicity.

The spatial distribution of the aftershocks is non-uniform. In particular, the Maule event triggered the highest number of events in the south and north direction from the mainshock epicenter. The Tohoku-oki aftershocks have the highest concentration to the north-west and south-west from the mainshock epicenter. However, in the case of the Tohoku-oki event it is not absolutely clear, if the relatively high off-shore magnitude of completeness (m_c up to 4.3) does not prevent the detection of the aftershock clusters off-shore. Both studied events have intensive crustal event activities. For the Maule case this activity is most pronounced in the Pichilemu cluster, located to the north from the mainshock epicenter (*Lieser et al.*, 2014). Similarly, the large crustal aftershock cluster triggered by the M=7.0 Fukushima event (south-west cluster) coincides with the high aftershock density area in the Tohoku-oki case.

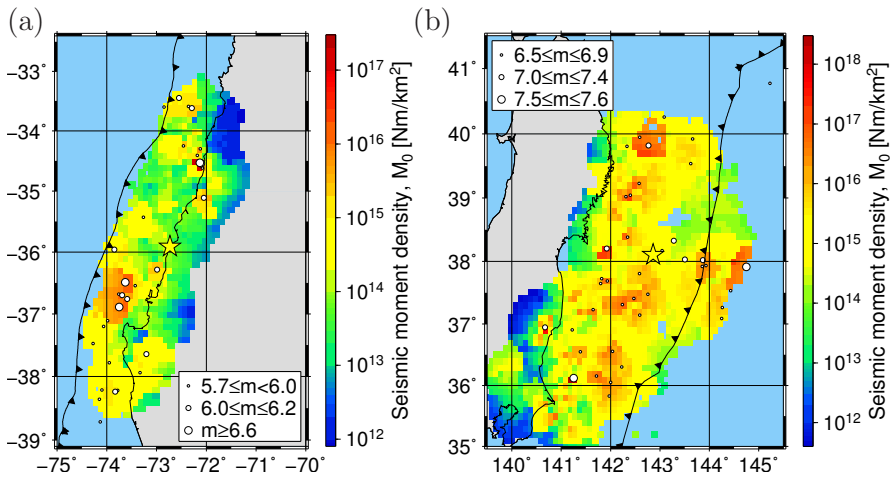

Figure 5.8: *Seismic moment release for (a) the Maule in the first* 106 *days and (b) the Tohoku-oki in the first* 100 *days of aftershock activities. The largest aftershock in the Maule sequence has a magnitude of 7.0. The maximum Tohoku-oki aftershock in the catalog is 7.6. White circles are the largest aftershocks, which are coded my the circle size according to the magnitude.*

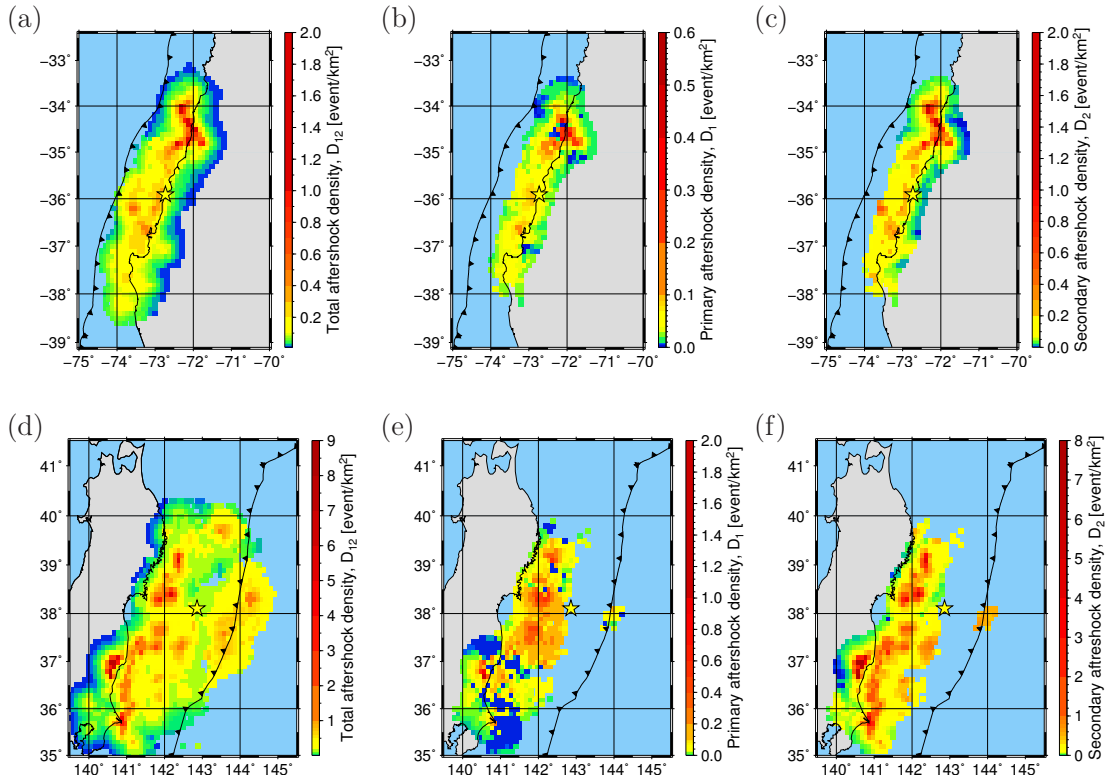

Figure 5.9: *Aftershock density in the case of the Maule and the Tohoku-oki aftershock sequences presented on the upper and the lower panels, respectively. (a,d) Total aftershock density, (b,e) primary aftershock density, (c,f) secondary aftershock density. All density values are calculated and corrected to* $m \geq 2.0$ *events using the estimated b-values and* m_c *for each spatial point. Yellow star indicates mainshock epicenter while the black line with triangles shows the trench position.*

5.5.5 Uncertainties of the Aftershock Parameters

We calculate the uncertainties of the aftershock parameters using two different methods (see Section 5.3.7): (i) by a Hessian matrix approach for the directly inverted ETAS parameters K_0, K, α, c and p; (ii) by error propagation method for the derived aftershock parameters D_1 and TP_2. To present the uncertainties we use the ratio between the calculated one standard deviation of the parameter and the parameter value $\frac{\Delta X}{X}100\%$ in percentage.

In the Figure 5.10 we show the relative uncertainties as a function of the number of points N required for the parameter inversion (with maximum radius of 50 km).

The uncertainties of the Tohoku-oki aftershock sequence are slightly higher than of the Maule event. In addition, the uncertainties of the aftershock parameters are in general large for both studied earthquake sequences. It might be a result of the finite space-time window selection (*Wang et al.*, 2010). At the same time the uncertainties of p- and α-values are on average smaller than for the other parameters. This outcome is in agreement with the results of *Veen* (2006) and *Wang et al.* (2010): for some ETAS parameters (for example K and c) the likelihood maximum is extremely flat; for others (p and α) it is usually relatively sharp. Of course large uncertainties point to the purely

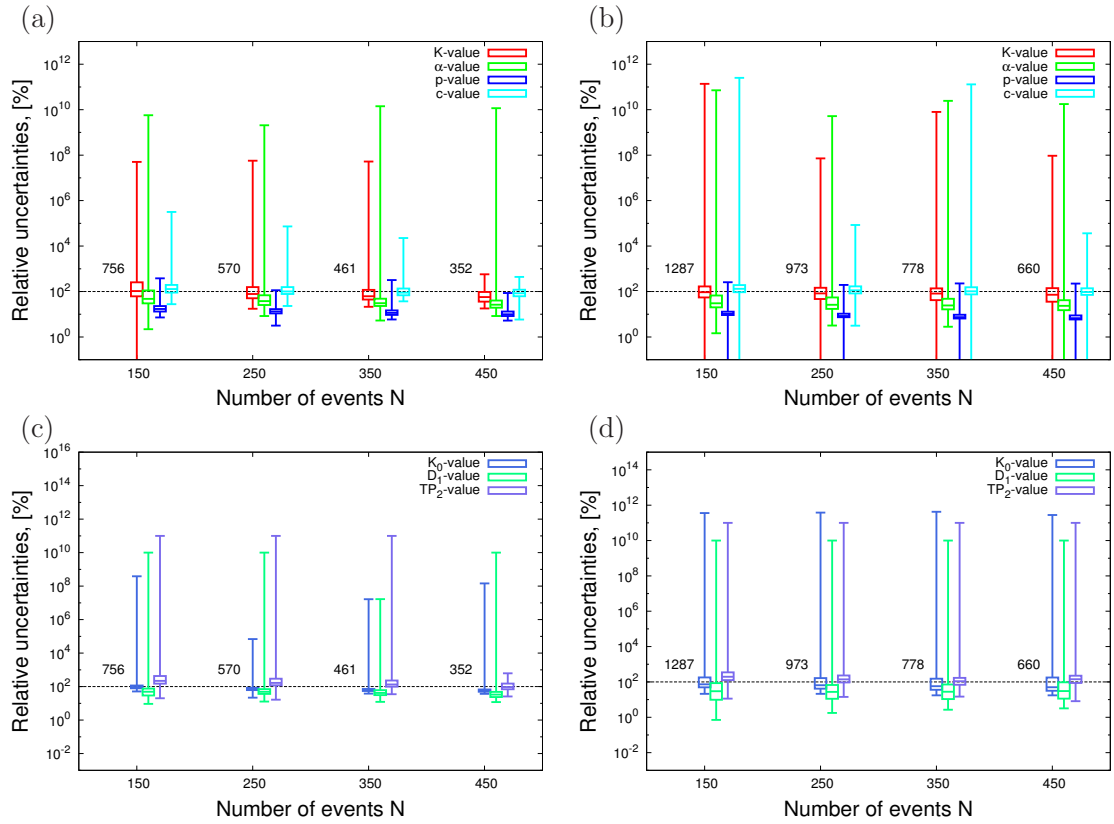

Figure 5.10: *Box plots of aftershock parameter relative uncertainties (a, c) for the Maule and (b, d) for the Tohoku-oki aftershock sequences with x as a function of the number of points N used in the calculation. The box plot whiskers indicate the minimum and the maximum values. The box plots for other parameters are shifted by 10% each at the x axis for clarity and the numbers near each box plot group show the amount of the estimated spatial points for the whole area. The bottom and the top of the box show the first and the third quartiles. The middle horizontal band inside the box corresponds to the median value (the second quartile).*

constrained parameters, however, the estimated ETAS parameters still contain useful information.

5.5.6 Correlations with the Physical Properties

To estimate a possible relation of the seismicity parameters with deformation patterns on the subduction interface, we calculate the correlation coefficients, with values between -1 (perfect anticorrelation) and +1 (perfect correlation), 0 shows no correlation. Though we present here only the results related to the Spearman rank correlation coefficient, we estimate the Pearson linear correlation coefficients as well. The main difference between aforementioned approaches is the ability of the rank correlation coefficient of Spearman to be less affected by the type of the samples distributions. To calculate the correlation coefficients and their significance between samples we use the numerical approach of *Press et al.* (1992). Results obtained using the Spearman method are similar to the results estimated by the linear correlation one.

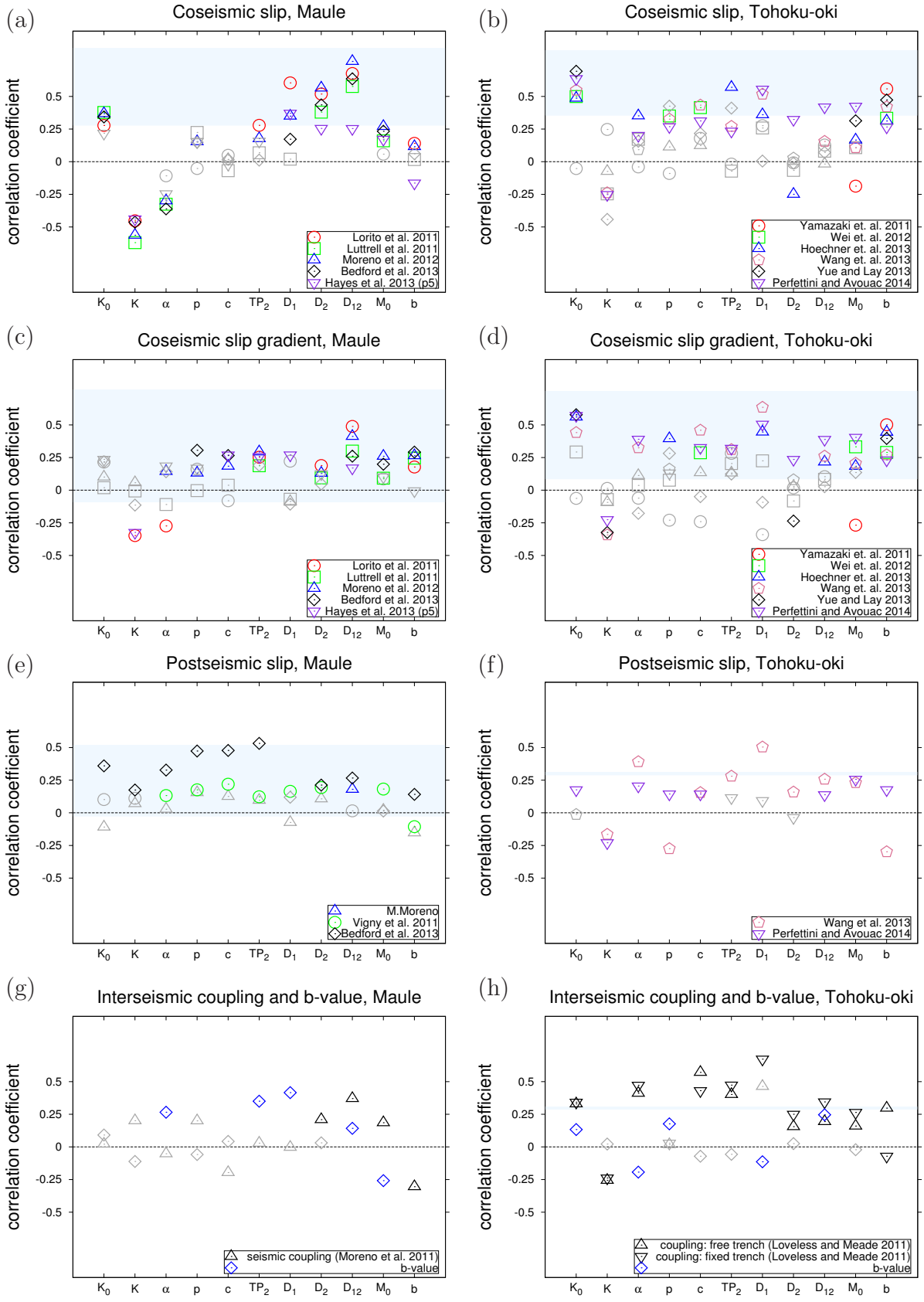
(a)
Coseismic slip, Maule
correlation coefficient
Lorito et al. 2011
Luttrell et al. 2011
Moreno et al. 2012
Bedford et al. 2013
Hayes et al. 2013 (p5)
(b)
Coseismic slip, Tohoku-oki
Yamazaki et. al. 2011
Wei et. al. 2012
Hoechner et. al. 2013
Wang et. al. 2013
Yue and Lay 2013
Perfettini and Avouac 2014
(c)
Coseismic slip gradient, Maule
(d)
Coseismic slip gradient, Tohoku-oki
(e)
Postseismic slip, Maule
M.Moreno
Vigny et al. 2011
Bedford et al. 2013
(f)
Postseismic slip, Tohoku-oki
(g)
Interseismic coupling and b-value, Maule
seismic coupling (Moreno et al. 2011)
b-value
(h)
Interseismic coupling and b-value, Tohoku-oki
coupling: free trench (Loveless and Meade 2011)
coupling: fixed trench (Loveless and Meade 2011)
b-value
K0 K α p c TP2 D1 D2 D12 M0 b

Figure 5.11: *Correlation coefficients for the Maule (left panels) and the Tohoku-oki (right panels) aftershock sequences. The correlation coefficients corresponding to different physical models are coded by different marker shapes. Coefficients are calculated for the 50 % best values (low uncertainties) in the case of $N = 250$ (Maule) and $N = 350$ (Tohoku-oki). The correlations between the geodetic models mentioned in the legend are marked by the blue shaded areas with lower and a upper limits corresponding to the minimal and maximal correlation coefficients, respectively. A bright color of the marker shows a significant correlation, meanwhile a light gray color corresponds to a non-significant correlation. The significance is checked by the P-value test, which has the reliability of 95%. Panels (a) and (b) are related to coseismic slip; (c) and (d) refer to coseismic slip gradient; (e) and (f) refer to postseismic slip; and (g) and (h) interseismic coupling, b-value. Both coupling models for Tohoku-oki are from Loveless and Meade (2011).*

Figure 5.11 shows the Spearman coefficient between different slip/locking models and the inverted aftershock parameters. Evidently, we calculate the correlation between b-value and aftershock parameters as well as between b-value and slip/locking models.

Coseismic slip. Correlation coefficients between coseismic slip models (Figure 5.11, panel a and b) and aftershock parameters show stronger correlation for the Maule than for the Tohoku-oki aftershock activity. In particular, the calculations yield significant correlation coefficients for the K_0, K, D_1, D_2, D_{12} and M_0 for the Maule case, meanwhile, for the Tohoku-oki case they are significant only for K_0, M_0 and b-value. We will mostly analyze the results, that show the same correlation trend for both aftershock sequences. In order to identify the most significant parameters for both aftershock series we consider only parameters which show high correlation for both earthquakes. These are in the case of coseismic slip the parameters K_0 and M_0. The seismic moment release is positively correlated with 8 and K_0 with 9 models out of 11.

The correlation between the coseismic slip and seismic moment density of the aftershocks showed that the largest aftershocks, occurred during the postseismic period, are located in the areas of maximal coseismic slip directly on subduction interface or above/below it. One of the interpretation of obtained correlation might be that the maximum coseismic slip areas have large unruptured asperities, however, due to the relatively low resolution of the slip models, these asperities might be not represented in the coseismic slip models. For example, *Lange et al.* (2014) showed that the size of aftershocks cannot be completely recovered from the inverted slip, due to smearing of the input signal amplitude during the inversion. We estimate the average slip patch size and the rupture area of the maximum aftershocks for both sequences using the *Wells and Coppersmith* (1994) approach. Here the models such as *Hoechner et al.* (2013) and *Yue and Lay* (2013) are unable to catch aftershock sizes up to the magnitude 7.0; and all other models (except, probably, for the *Moreno et al.* (2012) and *Lorito et al.* (2011)) up to $m = 6.7$. The second explanation might be related to the stress increase in the lithosphere directly above or below the maximum coseismic slip, which might lead to the aftershock triggering.

In the case of Tohoku-oki precisely located earthquake datasets based on Ocean-Bottom Seismograph (OBS) recordings (*Shinohara et al.*, 2012, e.g.), as well as analysis of focal mechanism data (*Asano et al.*, 2011) indicate that many of the Tohoku-oki aftershocks occurred within the overriding plate or subducting Pacific plate (i.e., above or below the mainshock co-seismic rupture). Such events - many of them of normal-fault or strike-slip type - may reflect changes in the stress field following the 2011 Tohoku-

oki earthquake (e.g., *Shinohara et al.* (2012) and the references therein). Nevertheless, other studies (*Ide et al.*, 2011; *Yagi and Fukahata*, 2011, e.g.) report relatively large normal fault aftershocks that occurred approximately at the depth of the plate interface and interpret such events as being due to slip overshoot during the 2011 Tohoku-oki earthquake. The overshoot could have been a consequence of nearly complete stress drop by the Tohoku-oki megathrust earthquake (*Hasegawa et al.*, 2011; *Yagi and Fukahata*, 2011). Therefore, our aftershock moment release distribution is consistent with these previous reports. Moreover, due to the limited resolution of slip models, which cannot image the true heterogeneity of the mainshock rupture, it may be also possible that some of the large aftershocks occurred on small unruptured (but highly stressed) patches, along the plate interface. In the case of the 2011 Tohoku-oki earthquake it is almost impossible to detect spatial heterogeneity of slip with a length scale of a few tens of kilometers from inversion analyses of geodetic and seismic data.

Conversely to our results related to the total aftershock density D_{12} (positive for both events, but significant only for Maule) and seismic moment density release M_0 with respect to maximum coseismic slip, *Das and Henry* (2003) did not find any universal dependency between the aftershock occurrence and the slip value. However, analyzing four strike-slip earthquakes *Woessner et al.* (2006) found that the aftershocks are located in the areas of low slip.

The K_0-values are positively correlated with the coseismic slip as well (9 models of 11). As the K_0 is a scaling factor for the primary aftershock activity, the established correlation might point to the dependency between primary aftershock occurrence and coseismic slip. The D_1 correlation, which is always positive, but not always significant, confirms this theory.

Although we do not see a clear correlation between coseismic slip and b-value for Maule, we indicate a positive correlation for all slip models in the case of Tohoku-oki. It might show that the high b-values after the Tohoku-oki mainshock represent a strong stress release in this area consistent with regions of high slip (*Tormann et al.*, 2015).

Coseismic slip gradient. For the Maule 2010 event *Hayes et al.* (2013) and *Agurto et al.* (2012) found that the aftershocks occurred in the areas of moderate-to-low slip gradients. Also *Das and Henry* (2003) and *Rietbrock et al.* (2012) showed that the aftershock distribution correspond to the areas of rapid transition between high and low coseismic slip. That is why we estimated the correlation coefficients between coseismic slip gradients and aftershock parameters. Our results show that there is indeed a positive correlation with the total aftershock density D_{12}. If the coseismic slip gradient coincides with the positive static stress changes, then a massive aftershock occurrence is expected in these ares (*Stein et al.*, 1992; *Steacy et al.*, 2005; *King*, 2007).

Furthermore, we find a positive correlation between b-value and coseismic slip gradient. If the slip gradient refers to the stress changes, then we have a contradiction with the theory that high b-value related to low stress levels.

Afterslip. Analyzing correlations with afterslip models we should pay attention to the fact that, the difference in the slab geometry (in particular depth), significantly influences the result of the afterslip location. This problem is more dominant in the case of afterslip models compared to coseismic slip, because afterslip has much smaller values as also indicated by the low correlation coefficients between the alternative inversions,

indicated by the blue area in Figure 5.11, panel e and f). However, we have some correlation coefficients, which are significant and have the same signs for almost all models. Namely, 4 models of 5 give a positive correlation coefficients with the c-value and the total aftershock density D_{12}. The correlation with the total aftershock density might point to the fact that the afterslip is an important factor for aftershock triggering. The c-value correlation with the postseismic slip might show that in the areas where the afterslip slip is large, the delay time of the aftershock decay tends to be longer than in the other regions. In other words, afterslip leads to a delayed and slower decaying aftershock activity in these regions, as seen in the applications of the rate-and-state frictional response model (*Cattania et al.*, 2015).

Seismic coupling. We have three models in the case of the interseismic coupling, one for the Maule (*Moreno et al.*, 2010) and two for the Tohoku-oki cases (*Loveless and Meade*, 2011). We obtain a positive correlation for the seismic moment release, total and secondary aftershock density. In particular the result that seismic moment release and the aftershock density are maximal in the regions that are highly coupled agrees with previous works which suggest that interseismic coupling is correlated with the coseismic slip (*Moreno et al.*, 2010).

b-value. The b-value shows significant correlations in the case of both aftershock sequences for the total aftershock density D_{12} (see Figure 5.11, panels g and h). High b-values might indicate (a) a inhomogeneous rocks (*Mogi*, 1962; *Scholz*, 1968) or (b) low stress (*Schorlemmer et al.*, 2005; *Scholz*, 2015). Inhomogeneous rocks tend to fracture more, which leads to inability of weak materials to accumulate high stresses and decreases the probability of a large fracture to occur. Consequently, highly fractured rock at low levels of stress could produce a large number of aftershocks.

5.5.7 Methods limitations

Although the depth statistics theoretically can be considered in the equation 5.5 used for the aftershock parameter inversion, in practice it causes technical difficulties with the integration. In addition, the hypocentral depth is often badly constrained because of the uncertainties in the velocity models. Thus we neglected the depth information in our study.

Another limitation is the large uncertainties of the deformation models, which we used for comparison. Due to the large uncertainties in the slip models (*Cattania et al.*, 2014), the resulting correlation coefficients are significantly scattered, which requires a more sophisticated result interpretation. This problem is even more dramatic in the case of models with a relatively small inversion values (afterslip) and in the case of a small amount of available models (postseismic slip and interseismic coupling models). Generally, in the case of a perfect correlation between parameters and slip models, we cannot expect higher correlation coefficients than that between alternative slip inversions. These values are the highest for coseismic and the lowest for the postseismic slip models (see values in 5.11 e,f marked by blue horizontal bars).

One more difficulty is related to the rank correlation coefficient of Spearman. Though this coefficient is able to catch some functional dependencies, it cannot pretend for a full dependency analysis. For example, we obtain a questionable positive correlation coeffi-

cient between afterslip models (*Wang et al.* (2013) and *Perfettini and Avouac* (2014)) in the case of the Tohoku-oki event, while visual inspection would indicate an anticorrelation.

5.6 Conclusion

In this work we focus on the spatial aftershock parameter distribution models for Maule 2010 and Tohoku-oki 2011 earthquakes. For this goal we modified the ETAS model, which now accounts for aftershock triggering by the extended mainshock heterogeneous rupture source. In addition, this model is able to distinguish between aftershock triggered directly by the main event and secondary seismicity. We showed that m-ETAS model has often smaller AIC values than the classical one. This result indicates that parameters obtained by the m-ETAS model represent seismicity used for the inversion, better than the usual ETAS approach. Therefore, using temporal and spatial seismicity occurrence, we calculated aftershock parameter distributions applying m-ETAS model. We consider a number of published slip models for both events in order to assess differences between the geodetic models. Almost all parameters show anomalies in the areas of preexisting fault systems, which were reactivated by the mainshock stress changes.

Besides the analysis of the aftershock parameter variations with geological settings, we estimated the correlation coefficients between the ETAS parameter and fault slip models. Though the majority of the direct aftershock parameters did not show any significant correlation with the deformation data, we found that some combined parameters correlate with slip models, seismic coupling and b-value. In particular, (1) coseismic slip is shown to be correlated with the aftershock seismic moment density and the K_0-value characterizing the direct aftershock triggering; (2) coseismic slip gradient shows significant correlations with the b-value and the total aftershock density; (3) postseismic slip is correlated with the ETAS c-value, α-value and aftershock density; (4) seismic coupling shows some dependence on the total and secondary aftershock density and seismic moment release; and the (5) b-value found to be correlated with the total aftershock density. These dependencies might be related to the stress changes, caused by the mainshock directly or due to the elastic relaxation of the media, by material properties and the crustal inhomogeneity.

Acknowledgments

This work was supported by the Helmholtz Graduate Research School GeoSim and the University of Potsdam. In addition we would like to acknowledge http://equake-rc.info/SRCMOD/ database for the coseismic slip models, used in the manuscript.

6

SEISMIC MOMENT RATIO OF AFTERSHOCKS WITH RESPECT TO MAINSHOCKS

Olga Zakharova[1], Sebastian Hainzl[1] and Christoph Bach[1]

[1] GFZ German Research Centre for Geosciences, Potsdam, Germany

Published in Journal of Geophysical Research: Solid Earth
Vol. 118, 5856-5864, doi10:.1002/2013JB010191

6.1 Abstract

Empirical Båth's law indicates that the earthquake process is self-similar and provides an opportunity to estimate the magnitude of the largest aftershock subsequent to a mainshock. However, the analysis of this relation is limited to a small magnitude range and also depends on the aftershock selection rules. As an alternative, we analyze in this paper, the cumulative seismic moment of aftershocks relative to the mainshock moment, because (i) it is a physical quantity that does not only take the largest aftershock into account; (ii) background activity can be considered and as a result estimations are less affected by selection rules; and (iii) the effects of the catalog cut-off magnitude can be corrected, what leads to larger magnitude range for the analysis. We analyze the global PDE USGS catalog (combined with CMT focal mechanisms) and find that the seismic moment release of aftershocks is on average approximately 5% of the mainshock seismic moment. We show that the results can be well fitted by simulations of the ETAS model. In particular, we test whether simulations constrained by predictions of the static stress-triggering model, proposing a break of self-similarity due to the finite seismogenic width, are in agreement with observations. Our analysis shows that the observed dependency on the mainshock magnitude as well as systematic variations with the mainshock fault plane solution can be both explained by the constraints based on the static stress-triggering.

6.2 Introduction

It is well known that earthquakes are strongly correlated in time and space. A good example of such a correlation is aftershock triggering by mainshock. The event dependence can be partly explained by stress changes and structural heterogeneity of the crust (*Stein*, 1999). In the present work we focus on the dependency between the magnitude of mainshocks and their aftershocks and aftershock cascading triggering. One important empirical feature of aftershock sequences is Båth's law (*Bath*, 1965). This law states that the magnitude difference Δm between a mainshock and its largest aftershock does not depend on the size of the mother event; although Δm varies a little with the region of interest (*Felzer et al.*, 2002; *Console*, 2003) and is different in strike-slip and reverse/normal faulting environments (*Tahir et al.*, 2012). According to Båth's law this magnitude difference is in general equal to 1.2.

The observation that Δm is constant indicates that the total number of aftershocks scales with $\sim 10^{bm_m}$ as a function of the mainshock magnitude m_m, where b is the b-value of the Gutenberg-Richter law. This is equivalent to a scaling with the seismic moment M_m of the mainshock according to $\sim M_m^{(2/3)b}$. In contrast, a break of the scaling is expected in physical models of earthquake triggering due to the limited size of the seismogenic depth (change of material properties with depth from brittle crust to viscous-elastic mantel). In particular, recent results of a clock advance model based on the static stress interaction suggest that the productivity of small mainshocks scales with $\sim M_m$, while that for larger events scales approximately according to $\sim M_m^{2/3}$ (*Hainzl et al.*, 2010b). Consequently, the empirical observation of Båth's law seems to disprove the static stress-triggering model.

However, it has to be taken into account that the quantity Δm has a rather limited resolution. In particular, it can be only analyzed in the magnitude range $m_m \geq m_c + 2$, where m_c represents the completeness magnitude of the analyzed catalog (*Helmstetter and Sornette*, 2003). Furthermore, the result is biased by cluster selection rules because of missed aftershocks or misinterpretation of independent background events as aftershocks. To minimize these problems, we focus in this study on the ratio R between the seismic moment released by aftershocks and by the mainshock. As shown in the following, this value, based on observations, can be corrected for background events and undetected smaller magnitude events. This enables the analysis of observed seismicity and its comparison with earthquake models in a significantly larger magnitude range.

We compare observations with simulations of the Epidemic Type Aftershock Sequence (ETAS) model (*Ogata*, 1988); in particular also to a model version in which the aftershock-trigger potential is constrained by the results of the scaling aspect of the static stress-triggering model. After introducing the applied methodologies in Section 6.3, we test in Section 6.4 several predictions of the restricted ETAS model, in particular the value of Δm and R as a function of the mainshock magnitude as well as their dependency on the focal mechanism. Our findings are finally discussed and summarized in Sections 6.5 and 6.6.

6.3 Methods

In the present work, we focus on two values of earthquake sequences - the magnitude difference between the mainshock and its largest aftershock

$$\Delta m = m_m - m_{a,max} \tag{6.1}$$

and the ratio R between the seismic moment released by all aftershocks and the mainshock. For the latter, we use the formula $M(m) = 10^{9.1+1.5m}$ (*Hanks and Kanamori*, 1979) and calculate the seismic moment released by the mainshock $M_m = M(m_m)$, before-mainshock activity $M_f = \sum_{i:t_i<t_m} M(m_i)$ (all events which occurred before the mainshock) and after-mainshock activity $M_a = \sum_{i:t_i>t_m} M(m_i)$ (all events in the sequence after the mainshock), where t_m is the mainshock occurrence time.

While the presence of the background events cannot be directly considered in the Δm-value, the influence of the background activity can be taken into account by calculating the difference $M_a - M_f$. However, it should be noted that M_f also includes potential foreshocks. Hence, the term $M_a - M_f$ can be interpreted as the excess of the after-mainshock seismic moment release relative to the before-mainshock release. For the estimation of the before- and after- mainshock seismic moment release, we use time windows $[-T, 0]$ and $[0, T]$, respectively. Thus the calculated ratio between triggered and mainshock seismic moment release is

$$R = \frac{M_a - M_f}{M_m}. \tag{6.2}$$

However, the resulting R value is an underestimation of the true value of the seismic moment ratio, because of missed events with magnitudes below the detection threshold m_c. This means, that the seismic moments of events with magnitudes $m < m_c$ are not considered in equation (6.2), but this can be corrected for a given b-value. Let us assume that the frequency-magnitude distribution of foreshocks and aftershocks is given by the Gutenberg-Richter law, 10^{a-bm}, where only the a-value is different between the foreshock and aftershock distribution. The ratio between the total seismic moment release and the observed one for foreshocks and aftershocks in the magnitude range $[m_c, m_m]$ is given by

$$C(m_m) = \frac{\int_{-\infty}^{m_m} 10^{9.1+1.5m} 10^{a-bm} dm}{\int_{m_c}^{m_m} 10^{9.1+1.5m} 10^{a-bm} dm} = \frac{1}{(1 - 10^{-(1.5-b)(m_m-m_c)})}$$

Because this correction factor is the same for fore- and aftershocks, the corrected unbiased value of the seismic moment release ratio is consequently $R_{corr}(m_m) = C(m_m)R(m_m)$.

Based on the seismic moment ratio, we are able to calculate an equivalent magnitude difference

$$\Delta m_{eff} = -\frac{\log_{10}(R_{corr})}{1.5} = m_m - m_{a,eff} \tag{6.3}$$

with the effective magnitude for the triggered activity

$$m_{a,eff} = \frac{\log_{10}\left[(M_a - M_f)C(m_m)\right] - 9.1}{1.5}. \tag{6.4}$$

The effective magnitude can be seen as a replacement of the magnitude $m_{a,max}$ in Båth's law ($\Delta m = m_m - m_{a,max}$), which takes the cumulative seismic moment release of all aftershocks into account. To avoid the situation, when $R = 0$, we calculate the effective magnitude difference Δm_{eff} from the average of R over all clusters. We analyze these quantities (Δm, R, and Δm_{eff}) for earthquake sequences in observational global data sets and ETAS simulations, which are both introduced in the following subsections.

6.3.1 Observational Data

We analyze the global USGS PDE catalog in combination with the catalog of CMT focal solutions. While the magnitudes are taken using the PDE catalog, the fault plane solutions are added from the CMT data set for that cases in which events could be matched. For the analyzed time period between 1973 and 2011, we used a cut-off magnitude of $m_c = 5.0$ and only consider shallow events with a depth less than 50 kilometers. The magnitude of completeness is equal to the cut-off magnitude.

To separate seismic events into mainshocks (independent earthquakes) and their respective foreshocks/aftershocks (dependent earthquakes), no unique procedure exists and several alternative cluster selection procedures have been introduced in the past. A summary of the most prominent clustering procedures is given by *Stiphout et al.* (2012). In our work, we follow the window-based procedure of *Tahir et al.* (2012) for cluster selection. According to this, an earthquake with magnitude m is defined as a mainshock, if it is the largest earthquake within the time period $[-T, +T]$ and a distance range $D(m)$. The spatial window is set to be a multiple of the rupture length, i.e. $D(m) = \kappa L(m)$, where $L(m) = 10^{-2.44+0.59m}$ is a subsurface rupture length for all types of focal mechanisms in kilometers (*Wells and Coppersmith*, 1994) and κ is a variable coefficient. The time interval for our subsequent analysis is $T = 1$ year, although typical aftershock sequences are longer. However, longer time intervals would lead to an enlarged contamination by background activity. Using the fixed time span of 1 year, we account for the same fraction of aftershocks independently of the mainshock magnitude. According to the Omori-Utsu law (*Utsu et al.*, 1995), this fraction of aftershocks $f_a = N_{after}(T = 1year)/N_{all}(T_{all})$ is e.g. equal to 0.97 and 0.95 for $p = 1.2$ and the total aftershock duration of $T_{all} = 10$ years and $T_{all} = 100$ years, respectively. The parameter κ is set in the range $[1, 5]$ in accordance with general observations of aftershock occurrences. The lower limit for κ can be defined according to the minimum area of the aftershock distribution, i.e. the radius of space window is equal to one rupture length. The upper boundary for the rupture length is less clear, because remote aftershock triggering is known to occur very far away and these events will be missed for smaller values of κ. However, increasing κ will also increase the number of independent background events that are wrongly identified as fore- or aftershocks. That is why we use different radii in the range between one and five rupture lengths in our cluster selection procedure and compare the corresponding results.

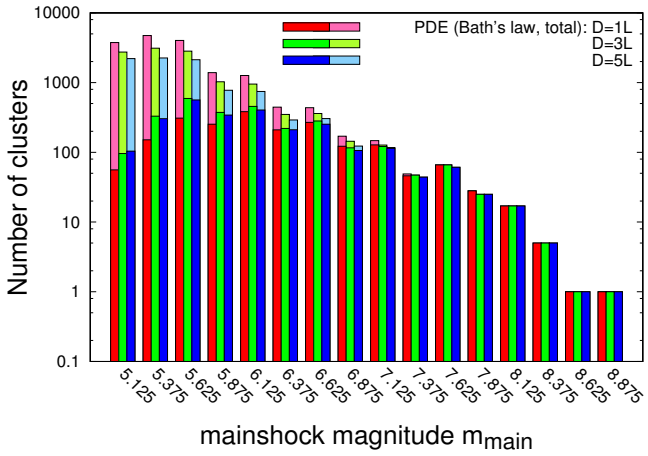

Figure 6.1: *The distribution of cluster numbers (PDE catalog) with respect to the magnitude of the mainshock and selection criteria. Each bar is related to the number of clusters, which are used for the calculations of the effective magnitude and seismic moment ratio. Dark colored bars indicate the number of mainshocks used for Båth's law estimation and include at least one aftershock. The magnitude value indicates the mean value of each bin with width 0.25.*

Not all the data can be used for the analysis of Båth's law because the calculation of Δm requires at least one aftershock in a cluster. To illustrate the number of clusters available for the different calculations, we present a histogram of the number of clusters with respect to the mainshock magnitude in Figure 6.1. Dark colors indicate the number of mainshocks, which can be utilized for the Δm value estimation, while the light colors show the number which can be used for all other calculations. We provide histograms for all applied spatial windows of the cluster selection. For magnitudes larger than 7.5 the number of clusters is the same for all types of analyses, while for smaller magnitudes less than 10% of the clusters can be used for the calculations related to Båth's law. In addition, Figure 6.2 shows the histograms for the number of clusters that we obtained after combining the PDE catalog with CMT solutions as a function of the mainshock rake and time, respectively.

6.3.2 ETAS Simulations

For comparison with the observed data, we additionally analyze Monte-Carlo simulations of the Epidemic Type Aftershock Sequence (ETAS), which is nowadays one of the standard models for describing the first-order statistical features of earthquake clustering (*Zhuang et al.*, 2012). This statistical model is constructed based on a number of well-established empirical laws. The temporal correlations are described by the Omori-Utsu law, which states that the rate of triggered aftershocks decays with time t relative to the mainshock according to (*Utsu et al.*, 1995)

$$n(t) = \frac{K}{(t+c)^p}, \tag{6.5}$$

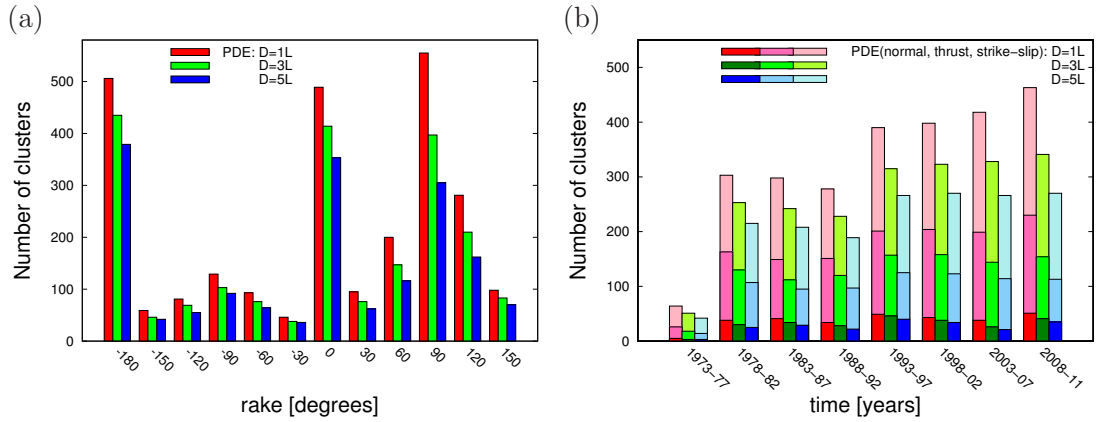

Figure 6.2: *Histograms of the number of clusters (PDE + CMT catalog) as a function of the rake of the mainshock (panel a) and the occurrence time (panel b) for different selection criteria. In panel b the different color shadings refer to the different rupture styles.*

where K, c and p are constant parameters. Furthermore, the aftershock productivity parameter K depends exponentially on the mainshock magnitude, $K \sim 10^{\alpha m_m}$. However, while the functional form is well established, the estimations of the parameter α vary largely between different estimation procedures (*Hainzl and Marsan*, 2008).

The ETAS model introduced by (*Ogata*, 1988) is based on these empirical relations and assumes that every earthquake has a potential to trigger its own aftershocks. There is no preestablished difference between mainshocks, foreshocks and aftershocks in the ETAS model. All events in the ETAS model are equivalent and events with smaller magnitudes can also generate earthquakes with larger magnitudes. Earthquakes are only retrospectively classified as mainshocks, fore- and aftershocks by their time occurrence in the cluster. As a consequence of the aforementioned, the earthquake rate λ at time t is described in the ETAS model by

$$\lambda(t) \quad = \quad \mu + \sum_{i:t_i<t} g(m_i) f(t-t_i) = \mu + \sum_{i:t_i<t} K_0 \, 10^{\alpha(m_i - m_{min})} \, (c + t - t_i)^{-p}, \qquad (6.6)$$

where μ is a constant background rate, K_0 is a constant and m_{min} is a minimum considered magnitude (*Ogata*, 1988).

We assume a minimum and maximum magnitude of $m_{min} = 3$ and $m_{max} = 9$ for our forward simulations and a doubly-truncated Gutenberg-Richter law for the magnitude distribution with a standard b-value of 1.

To avoid complications by incorrect earthquake classifications, we ignore the spatial component of the triggering process and thus account for all fore- and aftershocks independently of their distance to the mainshock. For event simulations in time span of one year we use the Monte-Carlo method. To determine one cluster, which consists of one simulated earthquake sequence, we use the following steps:

1. setting the first event of the simulated sequence to have a zero time and a magnitude randomly selected from the Gutenberg-Richter distribution;

2. performing a Monte-Carlo simulation of triggered activity initiated by the first

event within T;

3. removing all events with magnitudes less than cut-off magnitude $m_c = 5$ (unobserved seismicity);

4. defining the event with the maximum magnitude in the sequence as the mainshock;

5. classifying foreshocks as all events before and aftershocks as all events after this "mainshock".

The described procedure is applied to each simulated sequence. Note that the definition of mainshock, fore- and aftershocks is identical to that for the observational data set. However, each synthetic sequence is only related to correlated events containing no independent background activity. Thus our synthetic simulations correspond to the result of a perfect cluster selection procedure. In most simulations, the initial event is small and no events are simulated above m_c, but we typically simulated 10^8 sequences for each parameter set, leading to a sufficient statistics for mainshocks in the analyzed magnitude range $m_c < m_m < m_{max}$. Note that for simplicity, the duration of the total cluster was chosen to be $T = 1$ year. Thus the time period for aftershock selection can be smaller than T. However, because the majority of clusters has no or only a very short foreshock sequence, this is not crucial. We checked the results of ETAS simulations for a time window of $T = 2$ years to be sure that the results are stable.

For our simulations, the parameters of the Omori-Utsu law are set to some typical values, namely $c = 0.001$ days and $p = 1.2$. However, we find that the results do not depend significantly on this particular choice. In contrast, the productivity parameters K_0 and α are not directly fixed. Due to the large observational uncertainties and its impact regarding Båth's law, we explore different values of α in the range between 0.5 and 1.1. The best fit of the simulated data to the observed one in the case of Båth's law corresponds to $\alpha = 0.95$. Hereinafter we use $\alpha = 0.95$ for all ETAS simulations presented in this paper. Finally, for given parameters c, p, and α, we determine K_0 indirectly by setting the branching ratio r to a reasonable value.

One can describe the aftershock triggering as a branching process, where each mother event has its own "branch" of aftershocks (every event has only one precursor). The branching ratio r shows the average fraction of triggered events, which is the average number of daughter events per precursor event, and can be calculated by (*Helmstetter*, 2005)

$$r = \int_{m_{min}}^{m_{max}} \mathrm{pdf}(m) N_a(m) dm, \tag{6.7}$$

where $\mathrm{pdf}(m)$ is the probability density function of the earthquake magnitudes, which in the case of the doubly-truncated Gutenberg-Richter distribution becomes

$$\mathrm{pdf}(m) = \frac{\ln(10)\ b}{1 - 10^{-b(m_{max} - m_{min})}}\, 10^{-b(m - m_{min})}\ . \tag{6.8}$$

Furthermore, $N_a(m)$ is the average number of direct aftershocks triggered by an event

of magnitude m

$$N_a(m) = K_0 10^{\alpha(m-m_{min})} \int_0^\infty (c+t-t_i)^{-p} dt = \frac{K_0 10^{\alpha(m-m_{min})} c^{1-p}}{p-1} \quad (p>1)\,. \quad (6.9)$$

Consequently, the branching ratio is related to the model parameters according to

$$r = K_0 \frac{c^{1-p}}{p-1} \frac{b}{b-\alpha} \frac{1-10^{(\alpha-b)(m_{max}-m_{min})}}{1-10^{-b(m_{max}-m_{min})}} \quad (6.10)$$

Depending on the value of the branching ratio, it is possible to separate significantly different cases of model behavior: a branching ratio of $r > 1$ leads to exploding seismic sequences; $0 < r < 1$ describes a stationary regime with decaying aftershock sequences; while $r = 0$ implies that all events are independent and thus represents a Poisson process. The first case ($r > 1$) does not have any long-term observational evidence and the branching ratio value has a range $r \simeq 0.5 - 0.8$ according to observations (*Sornette and Werener*, 2005; *Shearer*, 2012). This range of values is also used to set K_0 in our forward simulations.

6.3.3 Restricted ETAS Simulations

In the case of the restricted ETAS simulations, we use constraints for the aftershock productivity based on the hypothesis of static stress triggering. For this purpose, we exploit the results of (*Hainzl et al.*, 2010b), who analyzed a simple clock-advance model. The model assumes that the total number of triggered events N_a in response to a Coulomb stress change ΔCFS is equal to the number of events which would have been triggered as independent events by an equivalent tectonic stress loading during a much longer time interval. In this case, the number of triggered aftershocks can be shown to be

$$N_a = \frac{V}{\langle M \rangle} \Delta CFS, \quad (6.11)$$

where V is a seismogenic volume and $\langle M \rangle$ is the average long-term seismic moment release per earthquake. The latter is related to the magnitude distribution (equation 6.8) and can be calculated using the following formula

$$\langle M \rangle \equiv 10^{9.1+1.5 m_{min}} \frac{b}{1.5-b} \frac{10^{(1.5-b)(m_{max}-m_{min})}-1}{1-10^{-b(m_{max}-m_{min})}} \quad [\mathrm{Nm}]. \quad (6.12)$$

The spatial distribution of ΔCFS depends on the rupture size and thus on the earthquake magnitude. However, the seismogenic depth D_{seis} interval, in which aftershocks can nucleate, is limited. This limitation of the seismogenic zone affects the trigger potential of large earthquakes and leads to a break of the scaling properties. According to numerical results of Hainzl et al. [2010], the cross-over magnitude m^* can be approximated by

$$m^* = \frac{\left(\log_{10}(W/4)^2 + 3.49\right)}{0.91}, \quad (6.13)$$

where $W = D_{seis}/sin(dip)$ is the maximum rupture width of earthquake ruptures in the

seismogenic zone for a given dip angle. This magnitude value separates approximately following two cases (*Hainzl et al.*, 2010b):

1. $m < m^*$ - a mainshock magnitude is less than m^*. All significant stress changes typically occur within the seismogenic zone and the aftershock number scales according to
$$N_a(m) = 2\frac{M(m)}{\langle M \rangle} = 2\frac{10^{9.1+1.5m}}{\langle M \rangle} \tag{6.14}$$
2. $m \geq m^*$ - a mainshock with a magnitude larger or equal to m^*. Parts of significant stress changes occur outside the seismogenic volume and leads to
$$N_a(m) = N_a(m^*)10^{1.07(m-m^*)}\,, \tag{6.15}$$
where $N_a(m^*)$ is given by Eq. 6.14.

These forecasts of the static stress-triggering model are now implemented in the ETAS model leading to the so-called restricted model version (RETAS). In particular, the function $g(m) = K_0 10^{\alpha(m-m_{min})}$ in equation (6.6) is now replaced by $N_a(m)/\int_0^\infty (c+t-t_i)^{-p}dt$, while all other simulation parameters $(c, p, b, m_{min}, m_{max}, m_c)$ remain the same. As a result we have the following equation for the RETAS model:

$$\lambda_R(t) = \mu + \sum_{i:t_i<t} \frac{N_a(m)}{\int_0^\infty (c+t-t_i)^{-p}dt}(c+t-t_i)^{-p} \tag{6.16}$$

where $N_a(m)$ is substituted depending on the event magnitude, with one of the formulas (6.14) and (6.15), respectively.

The model directly depends on the maximum rupture width W or alternatively on the width of the seismogenic depth layer D_{seis} and the dip. However, the results also depend significantly on m_{max} via $\langle M \rangle$. Thus to explore the dependence, we perform simulations with the RETAS model with three different parameter sets, roughly representing the three types of a focal mechanism: ($W = 10$ km, $m_{max} = 8.5$) - strike-slip; ($W = 20$ km, $m_{max} = 8.0$) - normal; ($W = 40$ km, $m_{max} = 9.0$) - reverse.

6.4 Results

6.4.1 Båth's Law

Båth's law states that the magnitude of the largest aftershock is approximately 1.2 magnitudes less than of the mainshock. In the Figure 6.3 we present the magnitude difference between the mainshock and the largest aftershock of the sequence as a function of a mainshock magnitude. The straight dashed black line corresponds to Båth's law ($m_m - m_{a,max} = 1.2$), while the results for the real catalog are shown by colored lines for different spatial cluster selection windows. They are the same for the Figure 6.3a and 6.3b, where the observations are compared to the results of the synthetic simulations of the standard and the restricted ETAS model, respectively. Note that in the case of the standard ETAS model, the α-value and the branching ratio r have been used as free parameters to optimize the fit to the observations because of the lack of physical

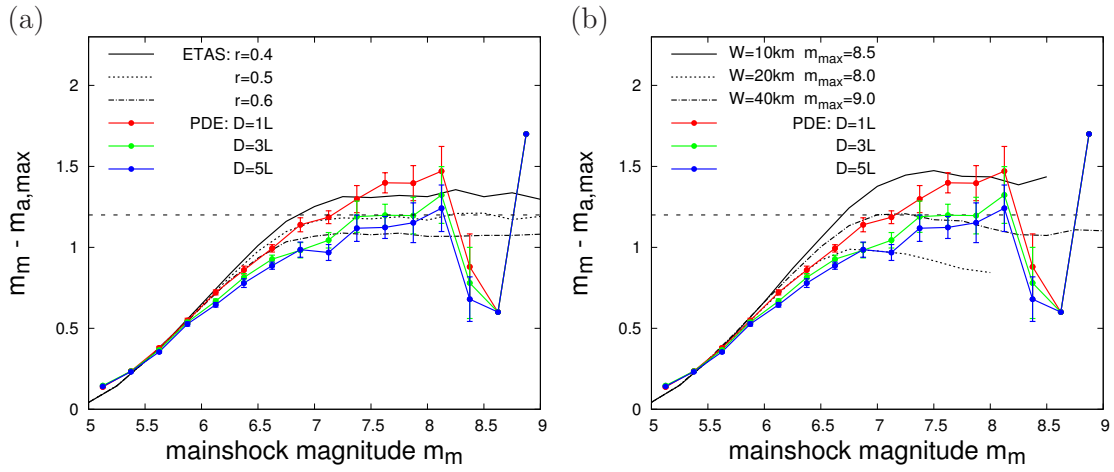

Figure 6.3: *The mean value of the magnitude difference between the mainshock and its largest aftershock for sequences with at least one aftershock. The observed values (colored dots) for different spatial selection windows according to (Tahir et al., 2012) are compared to ETAS simulations ($m_{min} = 3, m_{max} = 9, m_c = 5, b = 1.0, c = 0.001$ days, $p = 1.2, \alpha = 0.95$) (black lines). In panel (a), the aftershock productivity scales with $K_0 10^{\alpha m}$ and K_0 are calculated from the branching parameter r. In contrast, in panel (b), the productivity is restricted by the results of (Hainzl et al., 2010b). The set of parameters ($W = 10$ km, $m_{max} = 8.5$) corresponds to the strike-slip regime; ($W = 20$ km, $m_{max} = 8.0$) - normal; ($W = 40$ km, $m_{max} = 9.0$) - reverse.*

constraints. This leads to an α-value of 0.95 which is close to $b = 1$ and branching ratios between 0.4 and 0.6. In contrast, the restricted ETAS model (Figure 6.3b) depends only on the maximum width W of ruptures in the seismogenic zone and the maximum possible magnitude m_{max}. Thus the observations can be compared to simulations for reasonable values for different focal mechanisms.

Our analysis clearly demonstrates that Båth's law can only be examined in a small magnitude range. In particular, stable results for Båth's law can only be found in a repetition between 7 and 8 for the PDE catalog (see Figure 6.3). This can be explained by the absence of sufficient statistical data for events with magnitudes larger than 8. Here, the results for the synthetic catalog are less affected, because the number of simulated sequences can be increased to get stable results. The deviations of the curves for $m_m < 7$ are, on the other hand, the result of the fact that Δm cannot account for mainshocks that did not trigger any $m \geq m_c$ aftershock, because in this case the corresponding value is undefined. Thus Δm is the result of averaging only over sequences with $m_{a,max} \geq m_c$ and consequently $\Delta m \to 0$ for $m_m \to m_c$.

Furthermore, the results for the observational data are biased by the cluster selection rules. In contrast, we have no problems in the case of our simulations to properly select the dependent events, because we have, by construction, all triggered events above m_c in the catalogs without contamination with independent background events. Moreover, ETAS simulations do not have any spatial component, which could influence the cluster selection. In the present work we use only the information about magnitude and time of the events of a synthetic catalog. This is not the case for the PDE catalog analysis and the results are found to depend significantly on the selection parameters. Only a spatial selection window of $D = 3L$ gives a result close to 1.2 Δm, while the value is

around 1.4 for $D = L$ and 1.1 for $D = 5L$ (see Figure 6.3). Increasing of spatial windows leads not only to the larger number of distant aftershocks, but also for more and more independent events. Thus Δm will decrease necessarily towards 0 for $D \to \infty$. Vice versa, a significant number of aftershocks is missed for too small selection windows leading to an overestimation of Δm. Due to this interplay, an intermediate value of D has to be chosen, but anyway the choice remains arbitrary.

To show in which range observational data has larger uncertainties we calculated the standard deviation of all values of interest. For simulations we do not present any error estimation, because the result of the ETAS model is stable for a large number of simulations. The error estimation for the data was made using a bootstrap method with a Monte-Carlo procedure for data resampling. As events in the catalog are dependent (the magnitude and time of event determine its membership in the cluster), we apply a suitable resampling procedure - random sampling with replacement - by bootstrapping the earthquake clusters used for analysis. In the case of N clusters, we take randomly the same number of clusters from the subset of aftershock sequences using Monte-Carlo method. The random selection gives the replication of about 37% of original points. As a result, we estimate the errors (standard deviation), which take into account the epistemic uncertainty related to a lack of data. Figure 6.3 presents plus/minus one standard deviation of the magnitude difference in the all magnitude range. Error bars are reliable for $m_m \leq 8$; for the magnitudes $m_m > 8$ the standard deviation cannot be estimated correctly using bootstrap method, because too few observations are available for this range. The largest standard deviation for Δm is around 0.22.

The ETAS model result closest to Båth's law corresponds to a branching ratio 0.5 and $\alpha = 0.95$. For other α-values, Δm is slightly increasing ($\alpha < 0.95$) or decreasing ($\alpha > 0.95$) with increasing mainshock magnitudes above 7. For a higher branching ratio $r = 0.6$, Δm is underestimated and for a smaller one $r = 0.4$ it is overestimated. In contrast, the RETAS simulations do not depend on α and r. However, Figure 6.3b shows that also in this case of limited degrees of freedom the results are in a good agreement with the observations. The worst fit is observed for the "normal" fault type set of parameters ($W = 20$ km and $m_{max} = 8.0$), however, normal fault mainshocks are the smallest sample in the PDE-catalog above magnitude 7. In spite of the limitations, all simulations within the physical reasonable range show a rather good correspondence with Båth's law and the observed data.

6.4.2 Seismic Moment Ratio R and Effective Magnitude Difference Δm

The magnitude range which can be analyzed is significantly larger in the case of the seismic moment ratio $R_{corr}(m)$ and the effective magnitude difference Δm_{eff}. This becomes clear in Figure 6.4, where the results for the simulations of the ETAS and RETAS models are compared to the results of the PDE catalog. The reason is that also mainshocks with no aftershocks above m_c are taken into account. In these cases, the seismic moment of the aftershocks is zero. Furthermore, the cluster selection criteria are less critical, because subtracting the seismic moment released in the preceding time window, M_f, avoids a systematic effect of the included background activity. In fact the results for the three different spatial windows show no systematic trend for the PDE catalog. Quite

large fluctuations for the observed data are likely related to the relative small amount of mainshocks in the magnitude bins.

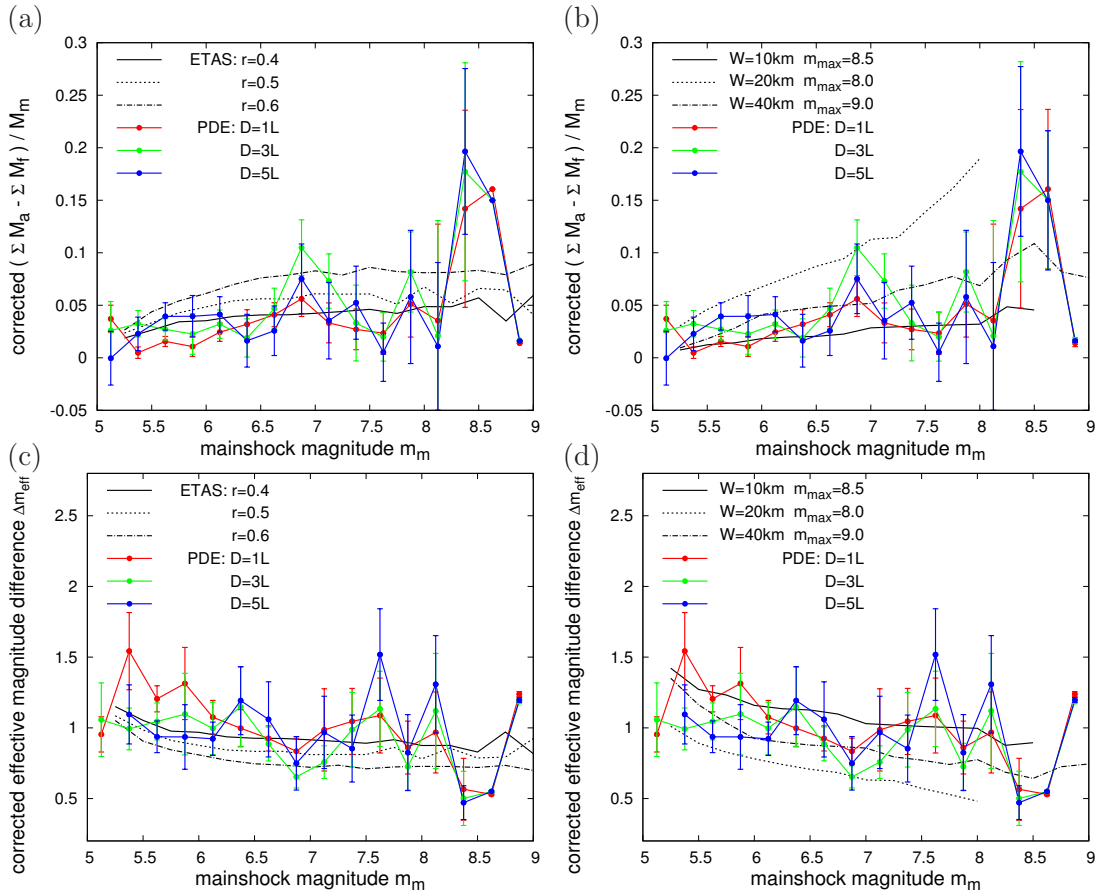

Figure 6.4: *The average corrected seismic moment ratio $R_{corr}(m)$ (plots a, b) and effective magnitude difference Δm_{eff} (plots c, d) as a function of the mainshock magnitude. For the description of the symbols and lines, see Figure 6.3.*

The comparison of the observed values with the synthetic data shows that both ETAS and RETAS reproduce the observations within one error interval. Overall, the RETAS model with less degrees of freedom can reproduce the general trend of the observed data even better, particularly in the case of the effective magnitude difference Δm_{eff} (Figure 6.4d). The values of Δm_{eff} are significantly smaller than Δm and range between 0.7 and 1, with a slight negative trend for increasing mainshock magnitudes.

Errors estimated for corrected seismic moment ratio R_{corr} and Δm_{eff} give one more indirect confirmation that these values can be analyzed in a wide range of magnitudes. For Figure 6.4a and 6.4b the standard deviation of R_{corr} is only slightly increasing up to magnitude 8, which shows that results are equally reliable. For Figure 6.4c and 6.4d errors are approximately in the same range for all magnitudes ($m_m \leq 8$). On average, errors are larger than in the case of Båth's law (see Figure 6.3), but remain smaller than ± 0.32.

6.4.3 Dependence on the Focal Mechanism

We analyze the sequence characteristics as a function of the rake of the mainshocks similar to the work of Tahir (Tahir, M., and J.-R. Grasso (2012), Faulting style controls on the Omori law parameters from global earthquake catalogs, *J. Geophys. Res.*, submitted). For this purpose, we evaluate the parameters in bins of 30°. It is found that the focal mechanisms have some obvious correlations with parameters such as the b-value, m_{max} (the maximum magnitude observed in the specific rake range), dip and seismic moment released by aftershock sequences (see Figure 6.5).

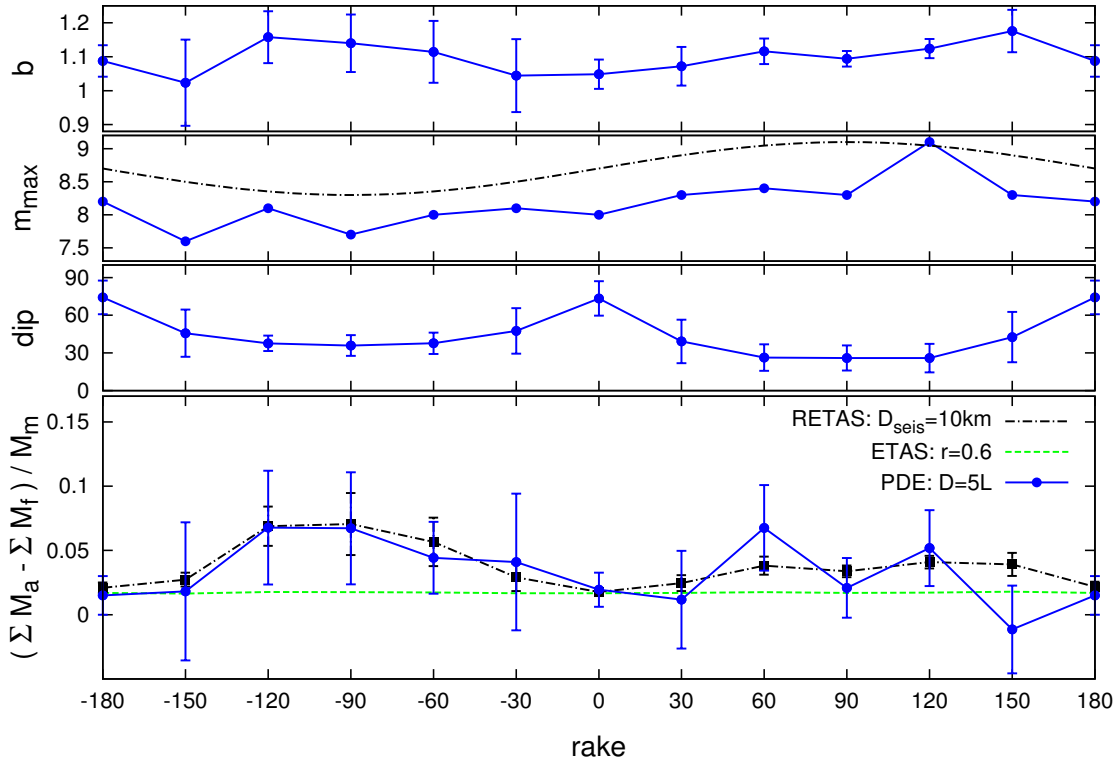

Figure 6.5: *Dependence of b-value, m_{max}, dip and the seismic moment ratio on the rake of the mainshock. The black line in the bottom figure refers to the results of restricted ETAS simulations based on Hainzl et al. [2010], where m^* is calculated from the dip-value and the assumed seismogenic depth D_{seis} according to $W = D_{seis}/sin(dip)$, and average long-term seismic moment release $\langle M \rangle$ is calculated based on the estimated b-value and m_{max} for each rake value. Because the observed maximum magnitudes are only a lower limit of the true value, we used a smoothed and shifted m_{max}-curve (black line). The values for the observational data are represented by blue dots. The green dashed line shows the result of standard ETAS simulations with the b-value as an input parameter (calculated for the case $D = 5L$) according to the rake of the mainshock.*

The standard ETAS model depends only on the b-value, on the contrary, the RETAS model explicitly depends on the dip, b, and m_{max}. The observed b-value is found to be unable to explain the variations of the R-ratio of the real data in the case of a standard ETAS model (see the green curve in 6.5). We therefore compare the observed variation of R with the R-values forecasted by the RETAS model based on the observed dip, b, and m_{max} values in each rake bin. Specifically, we use the dip, b, and m_{max} values as input to

calculate m^* and $\langle M \rangle$ and run 10^8 simulations to get the average seismic moment ratio for a given rake bin. We find that the RETAS model is overall in agreement within error bars with the observed data. For fitting, we used a depth of the seismogenic zone of $D_{seis} = 10$ km. Smaller or larger values would lead to a scaling of the resulting curve to smaller or larger R-values, respectively. The errors shown in Figure 6.5 for the RETAS model are smaller then for the observational data, because they are only related to the uncertainties of the b and dip input values.

The seismic moment released by aftershock activity is proportional to the number of events in the post-mainshock sequence. On its turn, the number of aftershocks (equation (6.11)) is controlled by two factors: the maximum rupture width W and the average seismic moment per earthquake which depends on b-value and the maximum magnitude. In response to these dependencies, the seismic moment ratio has a tendency to be the largest in the case of normal, intermediate for thrust and lowest for strike-slip faulting. This means that the amount of aftershock energy with respect to the mainshock magnitude seems to be the largest for normal faulting and the lowest for strike-slip faulting.

6.5 Discussion

The seismic moment ratio R and the corresponding effective magnitude difference Δm_{eff} (which are based on all clusters, but not only on the subsets with at least one aftershock) are shown to be superior to Δm, because these values are less affected by cluster selection rules and can be analyzed in a significantly larger magnitude range. However, similarly to Δm these parameters are strongly fluctuating for single aftershock sequences due to the power-law distribution of seismic moment release related to the Gutenberg-Richter magnitude distribution. Thus any forecast of these values for individual forecasts is subject to large uncertainties.

The average properties of a large sample of observed aftershock sequences can yield important insights into the physical processes underlying earthquake triggering. The best ETAS model needs $\alpha \approx b$ and a branching ratio of approximately 0.4 to explain the observations for the global data. Here it is important to emphasize that the branching parameter depends on the minimum earthquake magnitude. For practical reasons, we used in our simulations a minimum magnitude of 3, which is certainly above the true minimum earthquake magnitude m_0 in nature. According to (*Sornette and Werener*, 2005), the true branching ratio r can be estimated from the value $r(m_{min})$ obtained for simulations in the magnitude range $[m_{min}, m_{max}]$. For the special case $\alpha = b$ it is given by:

$$r = r(m_{min}) \frac{m_{max} - m_0}{m_{max} - m_{min}} \frac{1 - 10^{-b(m_{max} - m_{min})}}{1 - 10^{-b(m_{max} - m_0)}} \approx r(m_{min}) \frac{m_{max} - m_0}{m_{max} - m_{min}} \qquad (6.17)$$

This leads e.g. to a branching ratio of approximately 0.7 for $m_0 = -2$. Vice versa, the limit of $r = 1$ is related to an absolute minimum magnitude of about $m_0 = -6$.

This extrapolation implies a scale invariance of the trigger potential. However, we have shown in the last section that the RETAS model with a break of the scaling prop-

erties leads to similar or even better results. Additionally, the RETAS model can explain the observed dependence on the focal mechanism of the mainshock (rake-dependence). Thus the good agreement between the RETAS model and the observations indicates that static stress triggering could work. This would also imply that the trigger potential of small magnitude events is weaker than expected by the ETAS model and, consequently, the overall process is clearly sub-critical.

Besides aftershocks, aseismic postseismic deformation is often triggered by mainshocks. The aseismic moment release is sometimes several times larger than the aftershock moment. Thus it might be important to additionally include the aseismic moment release in the analysis of R and Δm_{eff}, which is in principal straightforward. However, this is difficult in practice and is left for future work, because the information related to postseismic deformations are not systematically recorded in earthquake catalogs.

6.6 Conclusion

The seismic moment released by aftershocks is shown to be an alternative diagnostic tool to characterize aftershock sequences. As demonstrated in the present paper, the seismic moment release ratio and the corresponding value of Δm_{eff} can be analyzed in a much wider range compared to the often used value of Δm, which is related to the magnitude difference between the mainshock and its largest aftershock. Our obtained results for global seismicity (PDE world catalog) indicate that the seismic moment released by aftershocks is approximately 5% the mainshocks seismic moment. Furthermore, the seismic moment release seems to be correlated with the focal mechanism, in particular with the rake of the mainshock. Both observations are used to test the agreement with the static stress-triggering hypothesis, which predicts that the total number of aftershocks is directly related to observable parameters such as the seismogenic width and the parameters of the magnitude distribution. Additionally, static stress triggering can explain a break of the aftershock productivity scaling, which is related to the finite width of the seismogenic zone. While the standard ETAS model based on scale-invariant triggering probabilities is found to reproduce the general features quite well, it does not explain the systematic variations with the focal mechanism. Furthermore, the productivity parameters of this model, K_0 and α, are free fitting parameters without any direct physical interpretation. In contrast, the ETAS model constrained by static stress triggering, the so-called RETAS model, is found to reproduce the observations even better, but without free fitting parameters. Our results indicate that the constraints derived from static stress triggering are in agreement with the data and that these results can be used to constrain the average total seismic moment released by aftershock sequences.

Acknowledgments

We acknowledge two anonymous reviewers and the Associate Editor for their helpful comments. Furthermore, are thankful to Álvaro González and Camilla Cattania for useful discussions. This work was supported by Helmholtz graduate research school GeoSim.

7

IMPACT OF ASEISMIC TRANSIENTS ON THE ESTIMATION OF AFTERSHOCK PRODUCTIVITY PARAMETERS

Sebastian Hainzl[1], Olga Zakharova[1] and David Marsan[2]

[1] GFZ German Research Centre for Geosciences, Potsdam, Germany
[2] Laboratoire de Géophysique Interne et Tectonophysique, Université de Savoie, France

Published in Bulletin of the Seismological Society of America
Vol. 103, No. 3, pp. 1723-1732, June 2013, doi: 10.1785/0120120247

7.1 Abstract

The epidemic-type aftershock sequence (ETAS) model has been shown to describe successfully the statistical seismicity properties, if earthquake triggering is related to tectonic forcing and earthquake-induced stress changes. However, seismicity is locally often dominated by stress changes related to transient aseismic processes. To avoid erroneous parameter estimations leading to biased forecasts, it is important to account for those transients. We apply a recently developed iterative algorithm based on the ETAS model to identify the time-dependent background and ETAS-parameters simultaneously. We find that this procedure works well for synthetic data sets if catalog errors are appropriately considered. However, ignoring the time-dependence leads to significantly biased parameter estimations. In particular, the α-value describing the magnitude-dependence of the triggering kernel can be strongly underestimated if transients are ignored. Low α-values have been previously found for swarm activity, for which transient aseismic processes are expected to play a major role. These observed anomalously low α-values might thus indicate the importance of transient forcing, rather than being due to differences in the earthquake-earthquake trigger mechanism. To explore this, we apply the procedure systematically to earthquake clusters detected in southern California and to earthquake swarm activity in Vogtland/Western Bohemia. While low α-values are mostly shown to be a consequence of catalog errors and time-dependent forcing but not related to different earthquake-earthquake interaction mechanisms, some significant low values are observed in high heat flow areas in California, confirming the existence of thermal control on earthquake triggering.

7.2 Introduction

Interactions between earthquakes have been long recognized to be an important mechanism for earthquake triggering. A large fraction of earthquakes in instrumental catalogs are aftershocks (*Reasenberg*, 1985), which can be explained by stress changes of previous events (*Dieterich*, 1994; *Harris*, 1998; *Stein*, 1999). Vice versa, earthquakes which cannot be attributed to any preceding earthquake are likely to be related to aseismic sources. Usually those events are associated to the stationary aseismic process of stress build-up due to constant tectonic plate motions. While this might be correct on long-time scales, transient aseismic forcing such as magma intrusion (*Toda et al.*, 2002), fluid flow (*Miller et al.*, 2004) or slow slip events (*Holtkamp and Brudzinski*, 2011) are frequently occurring on short-time scales. Because these aseismic processes are usually not directly observable, aseismic transients are generally ignored in seismicity modeling and forecasting. However, modeling of transient aseismic triggering is not only important because it can help to retrieve important information about the underlying mechanism, but also because the estimation of seismicity parameters can be - as we will show - strongly biased if the transients are ignored. This can directly affect our ability for short-time forecasting or seismic hazard assessment because both rely on a proper knowledge of the earthquake-earthquake interactions to model the clustering properties or decluster the seismicity, respectively.

An important seismicity parameter is the α-parameter, which determines how the number of aftershocks depends on ensemble average on the mainshock magnitude m. While there is good empirical evidence that this number grows exponentially with m as $\sim e^{\alpha m}$, the exact value of α varies substantially between empirical studies, in particular, between windows-based cluster definitions and epidemic type aftershock sequence (ETAS) model fits. The former class yields typically values around $\ln(10)$ (*Helmstetter*, 2005), although Christophersen and Smith (2008) showed that the inferred α-value is up to the specific choice of dependence of the spatial windows on the mainshock magnitude. An $\alpha = \ln(10)$ value gives a 10^m-scaling, which can be expected for static stress triggering (*Hainzl et al.*, 2010b). In this case, α would be also close to the observed exponent of the Gutenberg-Richter law describing the frequency of earthquakes as a function of magnitude, $N(m) \propto 10^{-bm} = e^{-\ln(10)bm}$, i.e $\alpha \approx \ln(10)b$. This would imply self-similarity of the triggering process, in particular, the cumulative effect of earthquakes in different magnitude bins would be the same. However, those window-based α-estimations are resulting from the comparison of the total aftershock productivity of many mainshocks with different magnitudes. More sophisticated models, which differentiate between direct and secondary aftershock activity, can estimate the α-parameter for individual sequences and often find significantly smaller α-values (*Ogata*, 1992; *Marsan and Lengliné*, 2008). Hainzl et al. (2008) showed that an underestimation of α can result in the latter case from assuming spatial isotropy of aftershock occurrence, which in fact aligns along the mainshock rupture. They also demonstrated the severe effect of such a parameter-bias on forecasts of ongoing aftershock sequences. However, the anisotropic aftershock distributions cannot explain small observed α-values, which result from estimations based only on time and magnitude information without using the hypocenter information. In particular, very small values, $\alpha < 1$, are found for swarm

activity, e.g. in Japan and Central Europe, and water-injection induced seismicity (*Ogata*, 1992; *Hainzl and Ogata*, 2005; *Lombardi et al.*, 2006; *Lei et al.*, 2008). These results could have important consequences for triggering mechanisms, because the cumulative effect of smaller events in earthquake swarms would then dominate compared to that of larger earthquakes. It is important to stress that low α-values, if they are real and the scaling holds for the whole magnitude range, would preclude earthquake forecasting: since small shocks then dominate the triggering budget, a reliable forecast would require precise knowledge of these small sources, down to the smallest possible rupture length, a more than challenging task.

In this study, we show that small α-values inverted by means of the space-independent ETAS model do not necessarily point to differences in the earthquake-earthquake interaction mechanism; they can simply result from neglecting underlying aseismic transients. This might explain the observed small α-values in the cases of earthquake swarms or induced seismicity, where aseismic sources such as fluid flows are expected or known.

We firstly introduce in section *Method* the recently developed approach by Marsan et al. (2012), which we used for detecting time-dependent aseismic forcing. A detailed analysis of synthetic earthquake sequences is presented in Sec. *Synthetic tests* to illustrate the effect of ignoring transient forcing in seismicity parameter estimations. Then we apply the methodology to recent swarm activity in Western Bohemia and earthquake clusters in southern California (Sec. *Applications*). Finally, our results are discussed and summarized in last two sections.

7.3 Method

Our approach is only based on the time and magnitude information (t_i, m_i with $i = 1, \dots N$) for an earthquake sequence in a given spatial region. Although this implies the application of somewhat arbitrary spatial selection criteria in practice and ignores more detailed information of primary and secondary spatial clustering, this restriction is based on good reasons: Firstly, the parameterization of the spatial probability function would be ambiguous, because the form of the spatial decay is still controversially debated (*Felzer and Brodsky*, 2010; *Richards-Dinger et al.*, 2010; *Marsan and Lengliné*, 2010) and the extension of earthquake ruptures, which leads to anisotropic aftershock clustering, cannot be appropriately taken into account based on catalog informations. The latter has been shown to result in strong biases of the parameter estimations, in particular, an underestimation of the α-value (*Hainzl and Marsan*, 2008). Furthermore, the problem of location errors and the additional need to quantify the unknown spatial component of the aseismic forcing term oppose an alternative use of a space-time model.

The applied method for detecting and accounting for time-dependent background forcing has been recently introduced by Marsan et al. (2012) and further tested and applied in Marsan and Enescu (2012). The rational is to separate the background forcing rate $\mu(t)$ and the contribution $\nu(t)$ related to earthquake-earthquake triggering, where the observed earthquake rate $\lambda(t)$ is assumed to be a linear superposition of both terms, $\lambda(t) = \mu(t) + \nu(t)$. The interaction term $\nu(t)$ is modeled using the epidemic type after-

shock sequence (ETAS) model (*Ogata*, 1988)

$$\nu(t) = \sum_{i:t_i<t} Ke^{\alpha(m_i-m_c)}(c+t-t_i)^{-p} \quad , \tag{7.1}$$

where c and p are the parameters of the Omori-Utsu aftershock decay law (*Utsu et al.*, 1995). The constants K and α describe the magnitude-dependent aftershock productivity and m_c is the lower magnitude cut of the analyzed catalog.

The algorithm for the model estimation consists of the following steps:

(0) Start with non-zero constant background rate $\mu(t) = \mu_0$

(1) Estimate the ETAS-parameters K, α, c, p by maximizing the log-likelihood (LL) value.

(2) Calculate probabilities that the events belong to background:

$$w_i = \mu(t_i)/(\mu(t_i) + \sum_{k:t_k<t_i} Ke^{\alpha(m_k-m_c)}(c+t_i-t_k)^{-p})$$

(3) Estimate the time-dependent background rate using the n-nearest neighbors:

$$\mu(t_i) = \sum_{k=i-n/2}^{i+n/2} w_k/(t_{i+n/2} - t_{i-n/2})$$

(4) Repeat with step (1) until convergence of both the ETAS parameters and the background rate is reached.

To select the appropriate smoothing window n, the Akaike Information Criterion (AIC) is used: n must minimize $AIC = 2(N/n - LL(n))$. Here N/n is a proxy for the number of free parameters in $\mu(t)$, and penalizes models with small n values that allow $\mu(t)$ to vary too quickly.

7.4 Synthetic Tests

We firstly analyze the effect of time-dependent aseismic forcing and catalog incompleteness for synthetic simulations, where the underlying dynamics is known. For that purpose, we performed ETAS simulations with a set of typical triggering parameters $K = 0.015, \alpha = 1.84, c = 0.01$ days,$p = 1.2$ and Gutenberg-Richter distributed magnitudes with a b-value of 1 in the magnitude range [0, 4]. These parameters refer to a theoretical branching parameter of about 0.8, which means that on average 80% of the earthquakes in the catalogs are aftershocks (*Helmstetter*, 2005). However, this value is reached only on long-time scales, while most short catalogs consist of only small magnitude events leading to a smaller percentage of aftershocks. Here, the aftershock percentage exceeds typically 50%. For the background term $\mu(t)$ of the ETAS model, we test three different versions described below. In each case, we analyzed 100 random independent simulations for a statistical evaluation. A summary of all parameters and definitions of our synthetic simulations is shown in Table 7.1.

description		values
time-intervals	catalog	$[-100:100]$ days
	LL-optimization	$T = [0:100]$ days
magnitudes		$0 \leq m \leq 4$; Gutenberg-Richter distributed with $b = 1$
ETAS-parameter	triggering	$K = 0.015, \alpha = 1.84, c = 0.01$ days, $p = 1.2$
	background-events	$N_b = 100$ or 500 in T
	ETAS-0	$\mu(t) = N_b/T$
	ETAS-1*	$\mu(t) = (N_b/T)(0.3 + (0.7/50)(1.0 - \cos(2\pi(t/50 - 0.5)))H(t-25)H(75-t)$
	ETAS-2*,†	$\mu(t) = (N_b/T)(0.3 + 0.7K\exp(-\alpha M_m)(c+t-50)^{-p}H(t-50)$ with $M_m = ln\left(N_b(p-1)/(K(c^{p-1} - (c+50)^{p-1}))\right)/\alpha$

* H denotes the Heaviside function.

†The choice of M_m is such that a mainshock of magnitude M_m occurring at $t = 50$ days would on average trigger N_b direct aftershocks in the following 50 days (remaining duration of the catalog).

Table 7.1: *Characteristics and parameters of the ETAS-simulations.*

7.4.1 Effect of Time Dependence

We explored the effect of two different types of time-dependent aseismic forcing on the parameter estimation. In one kind of simulations (ETAS-1), the temporal changes of the background forcing are smooth. The second type (ETAS-2) simulates the effect expected for an underlying aseismic stress step such as related to slow slip events. In this case, the aseismic transient triggering is modeled by a Omori-Utsu-type decaying rate. Two examples of ETAS-1 and ETAS-2 simulations are shown in Figure 7.1. In addition to these two types, we also analyzed simulations with constant background rate (ETAS-0) for comparison.

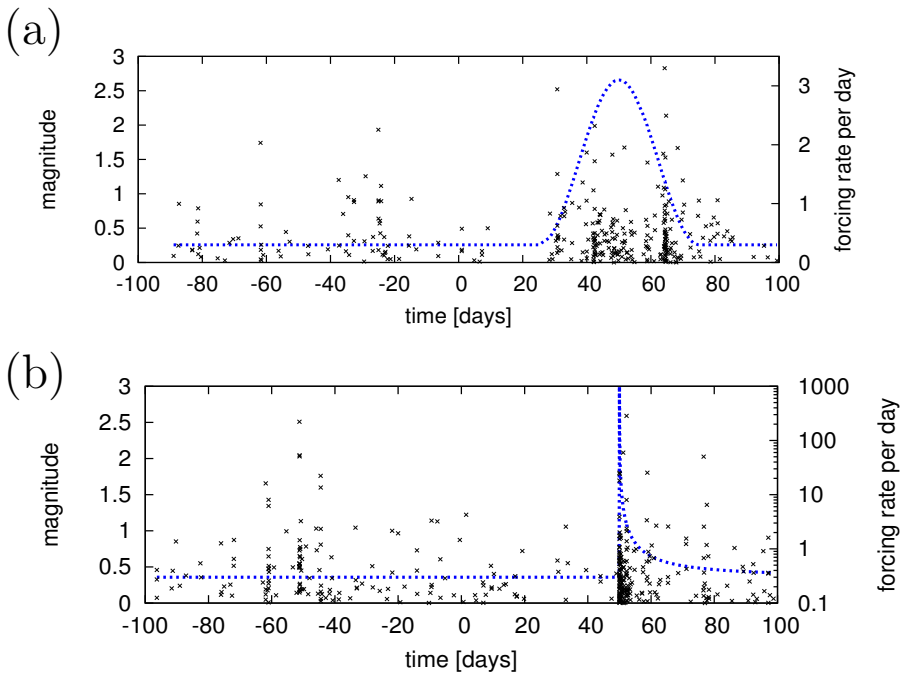

Figure 7.1: *Examples of tested ETAS simulations: (a) transient triggering with smooth transient forcing (ETAS-1) and (b) with mainshock-type aseismic forcing (ETAS-2). Both simulations consists of 100 background events. The dotted lines refer to the true background forcing rates.*

For each of these simulations, we estimated the ETAS-parameters on the one hand with the standard approach assuming constant background forcing and, on the other hand, with the new iterative method taking potential time-dependent forcing into account (see Sec. *Method*). The results for $N_b = 500$ background events are shown in Figure 7.2. Along with those for smaller data sets ($N_b = 100$), our findings can be summarized in the following way:

(i) In the case of the ETAS-0 simulations with constant background forcing, both methods yield similar unbiased estimations of the true underlying parameters. In particular, the time-dependent method by Marsan et al. (2012) correctly identifies in almost all the cases the constant background rate, even in the case of small data sets (100 background events).

(ii) Vice versa, in the case of the simulations with time-dependent forcing (ETAS-1 and ETAS-2), the method by Marsan et al. (2012) find a time-dependent forcing as preferred solution in almost all cases. Thus, the new method is able to detect aseismic transients in these data sets.

(iii) The estimation of the ETAS-parameters assuming constant background forcing yields strongly biased aftershock productivity parameters if aseismic forcing is present. In particular, the parameters K and α are biased, while the Omori-Utsu parameters c and p are less affected. K is overestimated and α is significantly underestimated. As a consequence, the estimated background rate is only in the order of 20% of the true value.

(iv) In the same case, the new method yields almost unbiased estimates. In particular, the α-value is well-recovered with moderate uncertainties.

It should be noted that, independent of aseismic transients, correlations between estimated ETAS parameters exist in general. In particular, both Omori-Utsu parameters c and p are strongly correlated (*Holschneider et al.*, 2012), while the estimations of both productivity parameters K and α are anti-correlated. The latter results from the fact that the total number of observed events is fixed. However, single parameter estimations are distributed symmetrically around the true values in the case of unbiased results, while they are systematically shifted in the case of biased estimations.

7.4.2 Effect of Catalog Errors

Besides transient forcing, catalog problems can also lead to biases in parameter estimates, in particular towards low α-values. To show this, we analyzed ETAS simulations (ETAS-0), which were artificially manipulated to represent three different types of catalog problems, namely (i) underestimated completeness; (ii) time-varying completeness; and (iii) missing events directly after earthquakes. Namely:

(i) Underestimated (time-independent) completeness implies that the data set is incomplete at low magnitudes. We simulate this by removing earthquakes according to a probability $\mathrm{erfc}((m - m_c)/\sqrt{2}\sigma_m)$ with $\sigma_m = 0.5$, where erfc is the complementary error function. This means e.g. that a $m = m_c + 0.5$ event remains in the catalog with a probability of 0.68 and a magnitude $m = m_c + 1$ event with probability

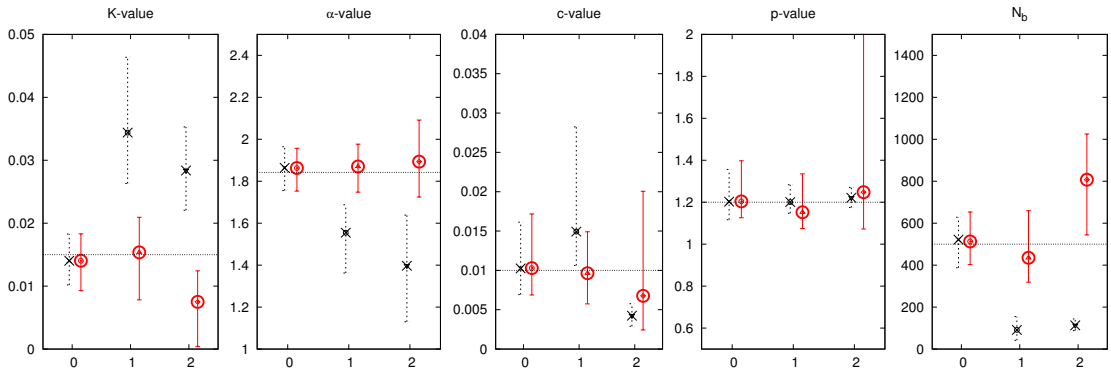

Figure 7.2: *Inversion results for ETAS-simulations with constant forcing (ETAS-0, left in each plot) and transient forcing (middle: ETAS-1 and right: ETAS-2). Crosses indicate the inversion results assuming constant background rate, while circles refer to results if potential time-dependent forcing is considered. We only show here the results with $N_b = 500$ background events; simulations with 100 background earthquakes yield similar results, albeit with larger error bars. The true parameters of the simulations are indicated by the horizontal line. In all cases, symbols refer to the median value of 100 simulations while the error bars show the range between the 10% and 90% quantiles.*

of 0.95. This erfc-shape is empirically found when investigating the probability of earthquake detection in regional earthquake catalogs (e.g. Ogata and Katsura 1993; Daniel et al., 2008).

(ii) Time-dependent incompleteness: All earthquakes with $m \leq m_c + 0.5$ are removed in the time window between 35 and 65 days.

(iii) Incompleteness after events: To account for the observed incompleteness of catalogs after mainshocks (*Kagan*, 2004), we adopt the estimated incompleteness function for California, $m_{cut}(m, \Delta t) = m - 4.5 - 0.75 \log_{10}(\Delta t)$, where Δt is the time (in days) after an earthquake with magnitude m (*Helmstetter*, 2006). We removed all earthquakes from the simulated catalogs for which the magnitude m_i does not fulfill the condition $m_i \geq m_{cut}(m_j, t_i - t_j)$ related to any preceding earthquake $j < i$.

Examples for all three cases are shown in Figure 7.3. Note that the considered incompleteness disturbs the frequency-magnitude distribution of the earthquakes and would lead to biased b-value estimations. However, this does not directly affect our parameter estimations, because the ETAS model fitting is only based on the observed earthquake magnitudes and needs no specification of the b-value. As we will see in the following, the parameter estimations are nevertheless affected by the catalog incompleteness, if not appropriately considered.

For statistical evaluation, we again analyzed 100 synthetic catalogs in each case. The estimated ETAS-parameters are summarized in Table 7.2. In particular, we found that removing about half of the events from the catalog in case (i) leads only to a lowering of K but not to any bias in the other parameters. Thus this case cannot be responsible for low α-values. However, the other two cases lead to a significant underestimation of the α-parameter. This can be understood because in case (ii) the missing events in the time period of 30 days have a similar effect as a decrease of the background rate during

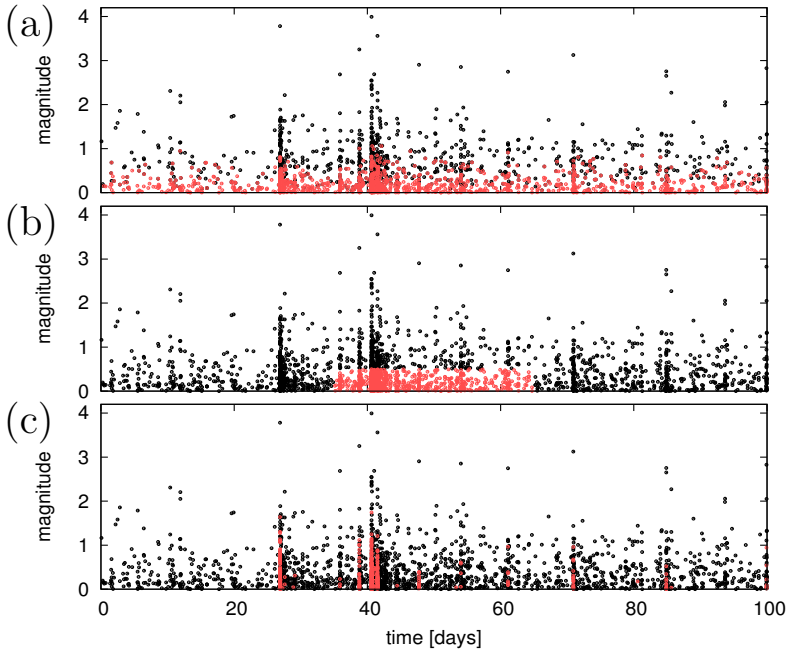

Figure 7.3: *Examples of earthquake catalogs artificially corrupted to represent realistic catalog problems. Light points refer to events deleted from the analyzed catalogs. The plots (a) to (c) refer to case (i) to (iii) in the text and Tab. 7.2, respectively.*

	type of missing events	K [$K_{10\%}$ $K_{90\%}$]	α [$\alpha_{10\%}$ $\alpha_{90\%}$]	c [$c_{10\%}$ $c_{90\%}$] [days]	p [$p_{10\%}$ $p_{90\%}$]
(i)	time-independent incompleteness	0.008 [0.005 0.011]	1.84 [1.71 1.97]	0.012 [0.006 0.018]	1.20 [1.05 1.32]
(ii)	incomplete time period	0.030 [0.015 0.047]	1.45 [1.05 1.80]	0.010 [0.006 0.016]	1.15 [1.02 1.33]
	...with LL-space restriction	0.011 [0.007 0.016]	1.91 [1.73 2.10]	0.017 [0.005 0.039]	1.32 [1.03 1.56]
(iii)	incomplete first aftershocks	0.018 [0.012 0.026]	1.71 [1.53 1.88]	0.017 [0.008 0.025]	1.28 [1.13 1.41]
	...for $c = 0.0007$ day; $K = 0.008$	0.014 [0.009 0.021]	1.54 [1.35 1.71]	0.0011 [0.0007 0.0015]	1.20 [1.12 1.27]
	...with LL-space restriction	0.008 [0.006 0.010]	1.87 [1.74 1.98]	0.0008 [0.0005 0.0010]	1.21 [1.14 1.27]

* The true parameters are that given in Tab.7.1, only in the last two cases of (iii), the c and K-value are changed to increase the effect of incompleteness.

Table 7.2: *Estimated ETAS-parameters for synthetic catalogs with artificially removed events representing typical catalog problems.**

this time. In case (iii), the scaling of the incompleteness time period with the mainshock magnitude lowers the apparent productivity of larger events compared to that of lower magnitudes. In the latter case, the bias of α is however quite small as long as c is not very small (e.g. a median value of $\alpha = 1.71$ instead of the true underlying value of 1.84 is estimated in our standard case of $c = 0.01$ days), but becomes significant for small c-values. We repeated the analysis for simulations with $c = 0.0007$ days (1 min) for which we rescaled the K-value to 0.008 to restore approximately the same branching parameter. In this case, the maximum likelihood method yields a value of 1.54.

This analysis shows that catalog errors of type (ii) and (iii) both lead to significant biases in the α-estimation. However, while missing earthquakes in case (iii) can go unnoticed, errors of type (ii) are relatively obvious and can be avoided by simply correcting the magnitude of completness. Alternatively, the likelihood space can be reduced, i.e. by restricting the number of earthquakes and/or the time-interval for which the pa-

rameters are optimized. In particular, we investigated two restrictions of the likelihood space, while the observation space (used for the calculation of the rate function, Eq. 7.1) remains the same: optimization is only done for (a) larger earthquakes, $m \geq m_c + 0.5$ (applied to case ii), and (b) events outside the incompletely recorded time-periods directly after earthquakes (applied to case iii). We find that these restrictions help to avoid the bias in the parameter estimation (see Tab. 7.2). Thus for the applications in the following section, we applied both restrictions to the likelihood space.

7.5 Application

7.5.1 Western Bohemia Swarms

Episodic occurrence of earthquake swarms is well-known in the region in West Bohemia/Vogtland, Central Europe, with the most intensive earthquake activity recorded in the years 1896/97, 1903, 1908/09, 1985/86, 2000, and 2008. Since 1994, the Novy Kostel area has been monitored by the local seismic network WEBNET providing high quality data, which enable detailed studies of the triggering mechanisms and driving forces of the West Bohemia/Vogtland swarms based on seismicity data. Due to the presence of close-by CO_2 emanations and observed correlations of their isotopic content with swarm activity (*Bräuer et al.*, 2007), episodic intrusions of fluid or magma are likely to be one of the driving forces of the observed earthquake clusters. This interpretation was confirmed by analysis of the seismicity showing a systematic temporal changes of the clustering properties and frequency-magnitude distribution during swarm activity (*Hainzl and Fischer*, 2002), as well as hypocenter migration (*Parotidis*, 2003; *Dahm et al.*, 2008).

Applying the ETAS-model to the year 2000 earthquake swarm, Hainzl and Ogata (2005) found a low α-value and a strong time-dependence of the background forcing. However, they chose rather arbitrarily a smoothing time window of 10 days and fixed the ETAS-triggering parameters for their analysis. We thus reanalyze the same swarm activity with the new methodology of Marsan et al. (2012). In addition to the year 2000 swarm, we also investigated the latest large swarm, which occurred in 2008. In both cases, we analyzed the earthquake data provided by the WEBNET. The frequency-magnitude distribution of both swarms is shown in Figure 7.4(a). The overall distributions can be approximately fitted by a b-value of about 1, but a closer inspection reveals a kink at $m \approx 1.5$. This magnitude seems to separate two different regimes: $b \approx 1.25$ for $m > 1.5$ and $b \approx 0.9$ for $m \leq 1.5$ with an estimated magnitude of completeness being around 0.5. The data set consists of 2450 events in the year 2000 and 2563 events in the year 2008 with $M_L \geq 0.5$. The temporal occurrence of the events is shown in Figure 7.4 (b) and (c).

All results of our ETAS-model analysis are summarized in Table 7.3. The analysis of the activity with the standard ETAS-model (constant background rate) yields very low α-values, namely 0.55 and 0.28 for the year 2000 and 2008 swarms, respectively. As demonstrated in the last section, these estimations might be affected by partial incompleteness of the catalog and time-dependent aseismic forcing. Therefore we firstly restricted the likelihood space to magnitudes above 1.5, where the kink in the frequency

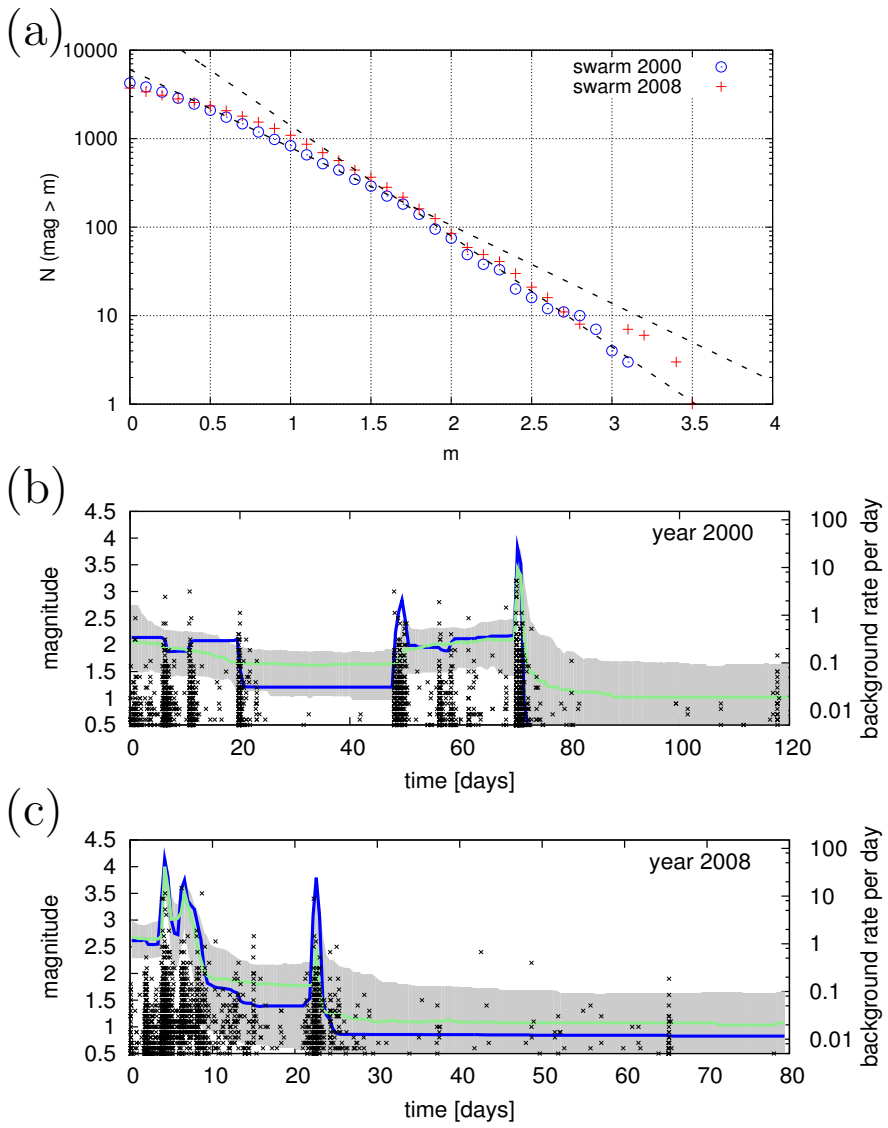

Figure 7.4: *Western Bohemia swarm activity observed in the year 2000 and 2008: (a) the frequency-magnitude distributions (b-values of 0.88 and 1.25 indicated by dashed lines); (b) and (c) observed magnitudes (points) and inverted background rates (lines) as a function of time. The dark lines refer to the results for the original data, while the light lines refer to the median and the gray shaded areas to the intervals between the 10% and 90% quantiles of the bootstrap results.*

year	background	background fraction	K	α	c [days]	p
2000	constant*	0.4%	0.0185	0.55	0.00048	1.35
	... with LL-space restriction†	2%	0.0050	1.50	0.00026	1.33
	$\mu(t)$ ‡	11%	0.0036	1.41	0.00026	1.37
2008	constant*	0.2%	0.0269	0.28	0.00041	1.29
	... with LL-space restriction †	0.6%	0.0065	1.55	0.00081	1.37
	$\mu(t)$ ‡	19%	0.0045	1.56	0.00045	1.36

* inversion based on constant background forcing without restrictions of the likelihood space.
† inversion based on constant background forcing with additional restrictions of the likelihood space.
‡ inversion accounting for time-dependent background forcing with restricted likelihood space.

Table 7.3: *Results for the estimated ETAS parameters in the case of the earthquake swarms in Western Bohemia.*

magnitude distribution is observed, while events with magnitudes between 0.5 and 1.5 are only used for the calculation of the rate function. Additionally we excluded the potentially incomplete time periods directly after earthquakes, where we used again the empirical incompleteness function of Helmstetter et al. (2006) (see Sec. *Effect of catalog errors*). As a result, the α-values significantly increase to values of 1.50 and 1.55. Besides potential incompleteness, we cannot exclude the possibility that this strong increase can also indicate some real differences in nucleation and interaction of the $m < 1.5$ swarm events, which might be indicated by their apparently different b-value.

Accounting additionally for time-dependent background forcing does not further increase the values, with $\alpha = 1.41$ and 1.56 then. Nevertheless, the inversion reveals a significant time-dependence of the aseismic forcing with a strong variation of the background forcing rate during both swarms (see lines in Figure 7.4). The optimal smoothing window size is found to be $n = 26$ and 30 for the year 2000 and 2008 swarms, respectively. To test the stability of the inversion results, we bootstrap the data. In particular, we used the inverted background rates and ETAS parameters to simulate 100 synthetic catalogs and then estimated the ETAS parameters and background rates in each case for the same smoothing windows. The corresponding median values as well as the 10% and 90% quantiles of the bootstrap results are added in Figure 7.4, indicating that the general trend is robust, although large uncertainties are involved. The standard deviations of the α-estimations for the bootstrap are 0.16 (swarm 2000) and 0.15 (swarm 2008). While the inversion based on the assumption of a constant background indicates only a negligible percentage of background events of 0.4% and 0.2%, a much higher percentage of 11% and 19% (with standard deviations of 4% in both cases) is found to be related to aseismic forcing after appropriately taking the time-dependence into account.

7.5.2 California Clusters

We used the catalog downloaded from the Southern California Earthquake Data Center (SCEDC) between 1980/1/1 and 2011/12/31 with 101,930 earthquakes with magnitude $m \geq 2$. The magnitude cutoff is used in accordance to the magnitude of completeness defined by the constraint that 95% of the events can be modeled by a power-law fit

of the frequency-magnitude distribution, following the procedure of Wiemer and Wyss (2000). In this data set, we limit our search for mainshocks to the square area defined by latitude $32.50° - 37.00° N$ and longitude $113.58° - 121.76° W$.

The separation into clusters is done in agreement with the method used by Enescu et al. (2009). An event is considered as indicator of a cluster if at least 100 events occurred within a temporal $\pm T$ and spatial $r \leq R$ window around it. Furthermore, this event has to be the largest event within the same spatiotemporal window to separate aftershock activity related to some preceding events. We consider only clusters, where the largest earthquake magnitude is between 3.5 and 6.0, because the use of circular spatial windows is considered only appropriate for the triggering zones of $m \leq 6$ events. We used a time window of $T = 100$ days and the search radius R is taken to be 5 times of the estimated fracture length L, where L is assumed to scale with the earthquake magnitude according to $L = 0.01\,10^{0.5m}$ km (Working Group on California Earthquake Probabilities, 2003; Helmstetter et al., 2005). Our selection criteria yields 36 clusters. For each of them we use, if available in the catalog, the seismicity of the 1000 days preceding the cluster in the same region as input information for the calculation of the ETAS rates. The so-called observation space is therefore: $[-1100 : 100]$ days and $m \geq 2$.

The parameter estimations might be affected by partial incompleteness of the catalog and time-dependent aseismic forcing as shown in our synthetic tests (see Sec. *Synthetic tests*). To test this, we firstly analyzed the clusters assuming constant background forcing without any additional restrictions for the likelihood space. This unrestricted LL-space is defined as $[-100 : 100]$ days and $m \geq 2$. In a second step, we still assumed a constant background forcing, but restricted the likelihood space to $m \geq 2.5$ and excluded the potentially incomplete time periods after earthquakes according to the results from Helmstetter et al. (2006) described in Sec. *Effect of catalog errors*. In the final step, we additionally allow for time-dependent background forcing in the parameter inversion. For all three cases, the results for the inverted ETAS-parameters are summarized in Table 7.4. A systematic change of the parameters is observed. In particular, the α-value is found to increase from a median value of 1.65 to 1.96 in agreement with our observations in the synthetic tests. Thus the α-values converge to the values estimated for stacked aftershock activity, for which e.g. Helmstetter et al. (2005) found $\alpha_{10} = 1.05 \pm 0.05$ related to the basis of 10, which is equivalent to $\alpha = 2.4 \pm 0.1$. Although the stacking procedure relates all aftershocks to the mainshock and measures therefore the dressed activity in contrast to the ETAS parameters, which are related to the direct (undressed) aftershock activity, the results of both approaches are expected to be in the same range. Furthermore, an α-value around 2.3 would be also in agreement with results for static stress triggering models (Hainzl et al. 2010). Because of this, we now ask the question the other way around: How many of the clusters are in agreement with a value of $\alpha = 2.3$, that means, a 10^m-scaling? To answer this question, we repeated our analysis for restricted LL-space and allowed time-dependent background forcing with fixed $\alpha = 2.3$. Clearly this always leads to a worse fit with a smaller LL-value, because the fitting has one free parameter less. For the judgment of the significance of allowing α to deviate from 2.3, we use again the Akaike information criterion. We find that 21 out of the 36 clusters can be best described by $\alpha = 2.3$. Thus the majority of clusters can be described by a 10^m-scaling of the productivity. In the other cases, we further identified the clusters,

where the difference in the AIC-value is at least 2, i.e. $\Delta AIC = AIC_{\alpha=2.3} - AIC \geq 2$. Note that $\exp(-\Delta AIC/2)$ can be interpreted as the relative probability that the $\alpha = 2.3$ model minimizes the (estimated) information loss (*Burnham and Anderson*, 2002). Nine clusters are found with $\Delta AIC \geq 2$; two of them with $\alpha > 2.3$ and 7 with $\alpha < 2.3$. These deviations from 2.3 seem to be not random. In particular, we find that the clusters with significant low α-values correlate well with areas of high heat flow. This is shown in Figure 7.5, where the estimated α-values are plotted as a function of the heat flow measurement closest to the mainshock. In particular, the four areas with highest heat flow are all related to significant low α-values (bold points). This trend compares well with observations of low α-values ($\alpha \approx 1.6$) on oceanic transform faults (*McGuire et al.*, 2005), for which high heat flow is expected (*Behn et al.*, 2007). Our results verify the results of Enescu et al. (2009) who found already correlations between high heat flow and low α-values. However, the past study did neither consider partial incompleteness nor account for potential aseismic forcing. Our new results indicate that the previous results were no artefacts related to those factors.

		K [$K_{10\%}$ $K_{90\%}$]	α [$\alpha_{10\%}$ $\alpha_{90\%}$]	c [$c_{10\%}$ $c_{90\%}$] [days]	p [$p_{10\%}$ $p_{90\%}$]
(a)	constant background*	0.023 [0.000029 0.040]	1.65 [0.91 2.87]	0.0057 [0.00023 0.033]	1.06 [0.85 1.27]
(b)	... with LL-space restriction†	0.011 [0.000004 0.027]	1.75 [1.00 3.41]	0.0033 [0.00011 0.030]	1.11 [0.88 1.29]
(c)	$\mu(t)$ ‡	0.005 [0.000001 0.024]	1.96 [0.84 3.40]	0.0028 [0.00001 0.032]	1.20 [0.99 1.54]

* inversion based on constant background forcing without restrictions of the likelihood space.
† inversion based on constant background forcing with additional restrictions of the likelihood space.
‡ inversion accounting for time-dependent background forcing with restricted likelihood space.

Table 7.4: *Median values and quantiles of the estimated ETAS parameters for the 36 earthquake clusters in California.*

7.6 Discussion

Our analysis shows that the maximum likelihood estimation of the ETAS-parameters can be strongly affected by catalog problems and aseismic transients. While possible catalog problems can be considered by appropriate restrictions of the LL-space in the standard ETAS-model applications, the latter issue needs more sophisticated approaches such as the iterative ETAS-based algorithm by Marsan et al. (2012) used in this paper.

In addition to the two discussed issues, a number of other problems have been previously shown to have also influence on the results of earthquake clustering models. In our study, we ignored the spatial information of the earthquake catalogs in order to avoid some of these problems, in particular the bias resultant from anisotropic aftershock clustering (*Hainzl and Marsan*, 2008) or space-dependent background seismicity (*Harte*, 2012). Nevertheless, other problems cannot be avoided such as missing links in magnitude, space and time. Notably the missed triggering effect from events smaller than the cut-off magnitude is important (*Sornette and Werener*, 2005). Unobserved events can trigger events above the threshold giving rise to apparently independent background events that seem to increase the constant background rate to an apparent rate. Although this can strongly affect the estimation of the background level, the bias for the trigger parameters K, c, α, and p does not exceed a few percent (*Wang et al.*, 2010), which is much

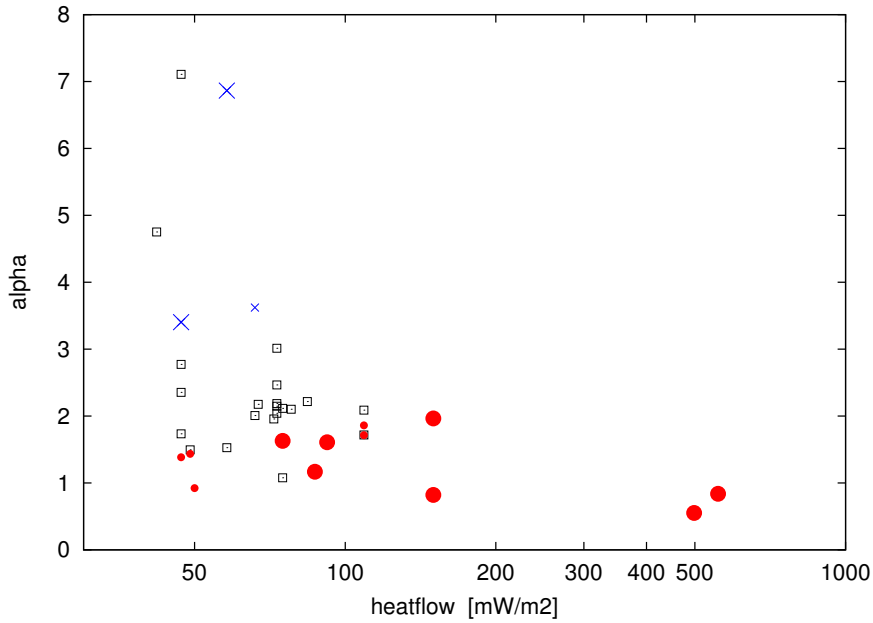

Figure 7.5: *Scatter plot of estimated α-values and the spatially closest heat-flow values in California. Squares indicate clusters which can be explained by* $\alpha = 2.3$*, i.e.* $\Delta AIC = AIC_{2.3} - AIC \leq 0$*, while the other symbols indicate clusters, where the Akaike information criteria points to a different α-value:* $\alpha < 2.3$ *(circles) and* $\alpha > 2.3$ *(crosses). Large symbols refer to those clusters with higher significance,* $\Delta AIC \geq 2$*.*

smaller than the bias observed in our analysis. Finally, Touati et al. (2011) showed that a high background rate can mask the earthquake triggering behavior. However, this seems to have only minor effects in our case because our approach has been demonstrated to yield robust estimations for synthetic simulations (see section *Synthetic tests*). In comparison, catalog problems and aseismic transients, as discussed in this paper, seem to have a stronger impact on the estimation of the trigger parameters and should therefore not be ignored in future studies.

7.7 Conclusion

While earthquake interactions are known to be responsible for a large fraction of recorded seismicity, the corresponding seismicity parameters describing the aftershock productivity are not well-constrained and a matter of ongoing debate. In particular, the α-parameter determining the magnitude-dependence of the trigger potential is crucial for identifying the underlying triggering mechanism and for forecasting ongoing earthquake sequences. Previous analysis of stacked seismicity resulted in significantly higher values than ETAS-based inversions. Our analysis now demonstrates that α can be strongly underestimated by the ETAS model, if potential catalog problems and aseismic transients are ignored. This might especially explain the previously observed small α-values in the case of earthquake swarms and water-injection induced seismicity, where transient forcing is expected or known (*Ogata*, 1992; *Hainzl and Ogata*, 2005; *Lei et al.*, 2008).

Our applications to earthquake swarms in Western Bohemia and earthquake clusters in California indicate a significant increase of the α-parameter after accounting for potential incompleteness and transient aseismic forcing. The majority of earthquake clusters in California become compatible with $\alpha = \beta = \ln(10)b \approx 2.3$. Thus both estimation procedures, the ETAS and the stacking approach, lead to concordant results. This is not trivial because one method estimates the parameter on basis of secondary aftershock triggering within an individual sequence, while the other method compares the cumulative productivity of different mainshocks. Furthermore, $\alpha = \beta$ implies that the impact of lower magnitude events is not as strong as previously thought. And finally, $\alpha \approx 2.3$ would be in agreement with estimations for static stress triggering (*Hainzl et al.*, 2010b).

However, some of the analyzed seismicity clusters show significantly smaller α-values also after accounting for incompleteness and transient aseismic forcing. Both analyzed earthquake swarms in Western Bohemia have similar values of $\alpha = 1.4 - 1.5$ and seven clusters in California show significant deviations to smaller α-values. These clusters show clear correlations with regions of higher heat flow. Thus proper accounting for incompleteness and transient aseismic forcing can help to avoid artificial parameter estimations as well as to detect true variations of the earthquake interaction mechanism.

Data and Resources

The heat flow data are taken from the USGS online heat flow database:
http://earthquake.usgs.gov/research/borehole/heatflow/table.php (accessed at February 2012). The California earthquake catalog has been downloaded from the Southern California Earthquake Data Center
(SCEDC, http://www.data.scec.org/eq-catalogs/date_mag_loc.php; accessed at February 2012). The WEBNET swarm catalogs have been provided by Tomas Fischer.

Acknowledgments

We are grateful for the helpful comments of two anonymous reviewers. The work was partially supported by the FP7 EU-REAKT, the BMBF-PROGRESS and the ANR ASEISMIC projects. The second author was supported by the Helmholtz-graduate school GeoSim.

GFZ German Research Centre for Geosciences
Telegrafenberg
14473 Potsdam
Germany
hainzl@gfz-potsdam.de
olgaza@gfz-potsdam.de
(S.H., O.Z.)

Laboratoire de Géophysique Interne et Tectonophysique
UMR CNRS 5559

Université de Savoie
73376 Le Bourget du Lac
France
david.marsan@univ-savoie.fr
(D.M.)

8

CONCLUSION AND OUTLOOK

8.1 Summary of Main Conclusions

Time dependent seismic hazard assessment requires appropriate seismicity models accounting for earthquake clustering (aftershock activity) on short-time scales. While the general empirical properties of aftershock occurrences are known, the parameters of the empirical laws are less constrained. My study helps to characterize the average seismic moment release of aftershocks per mainshock, the influence of seismic transients on the aftershock parameter estimation and the spatial variation of aftershock within one mainshock rupture area. However I also show that the interpretation of some obtained results remain unclear due to limited data sets and technical limitations as well as our poor knowledge of the underlying physical processes. In the following I discuss the obtained results in more details.

8.1.1 Spatial Distribution of Aftershock Parameters on a Scale of One Aftershock Sequence

The stress distribution and properties of the material play a dominant role in earthquake nucleation. The tectonic loading is approximately uniform, however, due to the crustal inhomogeneity, the stress distribution in a rock volume on a local scale might be very heterogeneous. Nonetheless, at the moment we do not have a detailed information about the local stress state as well as the crustal properties. Using a simple assumption that some information about crustal heterogeneity is presented in available slip and interseismic coupling models of the mainshock rupture area on the one side, and the aftershock distribution on the other side, I perform an analysis of the correlation between aftershock parameters and geodetic inversion models. For the aftershock parameter estimation I use a modification of the ETAS model (m-ETAS), which accounts for the mainshock rupture extension and apply this model to two aftershock sequences, in particular, to Mw8.8 Maule (Chile, 2010) and Mw9.0 Tohoku (Japan, 2011).

My detailed study of spatial aftershock parameter distribution in Chapter 5 demonstrates the following results:

- The m-ETAS model outperform the classical ETAS one, when the spatial component of aftershock distribution is taken into account.
- The obtained aftershock parameters distributed in space show anomalous values in the areas of the reactivated crustal fault systems.

- Due to large uncertainties in the estimated seismicity parameters as well as in the slip models the obtained results for the aftershock parameter correlation with slip models have a large scatter.
- In general the obtained correlation between aftershock parameters and geodetic data has the same trend for both analyzed sequences.
- I find almost no significant correlation between the individual aftershock parameters and geodetic inversion data, but some significant results for combined parameter describing the density of first- and higher-order aftershocks and their productivity.
- I find that seismic moment is positively correlated with the coseismic slip, which might be explained by (1) unruptured asperities in the coseismic slip area, not represented in the slip models due to their low resolution or (2) seismic moment might be maximal due to crustal seismicity above/below the subduction interface.
- Coseismic slip gradients, which are indicative for large stress changes, are positively correlated with the total aftershock density and b-value.
- The observed positive correlation of the postseismic slip, total aftershock density, c- and α-values might indicate that afterslip is an important factor in the aftershock triggering process.
- Interseismic coupling is positively correlated with the total and secondary aftershocks density and seismic moment density. While the correlation of seismic moment and total aftershock density is expected for a consistent magnitude probability density distribution, it is not clear, why secondary aftershocks but not primary aftershocks show this correlation. One of the reasons might be an unrepresentative sample of slip models.
- b-value shows positive correlation with total aftershock density. This dependency might be explained by the inhomogeneity of the rock, which prevents material to accumulate large stresses.

In general the results consist of large uncertainties, due to the poor quality of the geodetic models and a high magnitude of completeness in off-shore regions e.g. in case of the Tohoku aftershock sequence. However, the developed m-ETAS model might reveal correlations to other physical quantities in future studies. Also the obtained ETAS parameters maps might help to improve future regional hazard forecasts in the analyzed region.

8.1.2 Seismic Moment Release of Aftershocks

The main question, of the study reported in Chapter 6, is related to seismic moment release of aftershock sequences, in particular, seismic moment ratio variation with the rake of the mainshock. For this study we used global as well as synthetic data sets selecting events by space-time window approach. Due to the short observational period of seismicity and relatively high magnitude of completeness for the used global catalogs,

the obtained results have some fluctuations. However, the results of long synthetic catalogs are steady, therefore we compare our observational results with the results of the classical and restricted ETAS (RETAS) models.

The main conclusions of this study are:

- The cumulative seismic moment release of aftershocks is about five percent of the mainshock one.
- The seismic moment release ratio depends on the focal mechanism of the mainshock. In particular, for the normal mainshock faulting it is maximal, intermediate for thrust events and minimal for strike-slip ones.
- The estimated effective magnitude difference Δm_{eff} does not have the sample bias introduced by the cut magnitude (unlike for the Båth law), due to our ability to account for events smaller than m_{comp} and mainshocks having no aftershocks.
- The classical ETAS model simulations based on predefined branching ratios show a good correspondence with the results of observational data for the Båth law and m_{eff}, but cannot explain the variations of the seismic moment release with the rake of the mainshock.
- The ETAS model constrained by observations for static Coulomb stress triggering cannot only reproduce the Båth law and observed m_{eff} values, but can additionally explain the observed variations with the focal mechanism.

This study showed that knowledge of the focal mechanism and magnitude of the mainshock give a possibility to estimate the average seismic moment release of an aftershock sequence. It also indicates that the input in cumulative seismic moment of small events within one aftershock sequence is minor in comparison with seismic moment of the largest aftershocks. Furthermore, the success of the physics-constrained ETAS model indicates that hybrid models can significantly improve probabilistic seismicity forecasts.

8.1.3 Influence of Aseismic Forces and Different Types of Catalog Incompleteness on the Aftershock Parameter Estimation

My coauthors and I focus on the estimation of aftershock parameters for seismicity when aseismic transients or catalog incompleteness are present. Here we applied an ETAS model modification which accounts for changes of the background activity with time. As discussed in detail in Chapter 7, we obtain the following results:

- The α-value, which is decisive for the magnitude dependency is underestimated of the aftershock productivity, when the catalog is incomplete or when aseismic transients are ignored.
- The model application to the swarms in western Bohemia and earthquake cluster in California shows that the background rate significantly changes with time in many cases and that its consideration lead to an increase of the estimated α-value.
- α-values are smaller in regions of high heat flow (California).

- Consideration of the time dependent background rate in the ETAS model helps to identify the true interaction properties of earthquakes, which is important to improve seismic hazard forecasts.

Though in this work we show only the application of the time dependent ETAS model in the case of the natural seismicity, this model is also applicable for induced seismicity (*Lei et al.*, 2013, e.g.).

In this work my coauthors and I made successful steps towards the understanding of some aftershock properties. The principal application of this research might take place on a probabilistic level. In particular, obtained distributions of the aftershock parameter in space and the amount of seismic moment release theoretically could be used in the tasks of probabilistic seismic hazard analysis. In addition the time dependent ETAS model is useful for the unbiased rate calculation in the presence of aseismic sources or incompleteness issues of earthquake catalogs and unbiased parameter estimation for future seismic hazard studies: e.g. it might be applied for some regions of poor data set (incomplete catalogs) without introducing biases in the estimated aftershock parameters.

8.2 Suggestions for Further Work

Some more work can be done in the framework of the research presented in this thesis. Two main directions are: (1) testing the forecasting ability of the statistical models and (2) improving the understanding of stress/material inhomogeneity using aftershock sequences or the input of different physical processes on the aftershock occurrence.

For example:

- The m-ETAS model could be tested for its forecasting ability in the Collaboratory for the Study of Earthquake Predictability (CSEP) testing environment (http://www.cseptesting.org/centers/eth/details). The RETAS is already submitted in one of the CSEP centers by Sebastian Hainzl.

- One of the processes, which influences triggering of the aftershock activity, is afterslip and postseismic relaxation. Therefore it would be useful to look for some correlation between seismic moment release of aftershocks and the total afterslip moment.

- Is it any relation between aftershock sequence duration and the tectonic loading rate?

- One of possible continuations of this study related to the spatial aftershock distribution might be an investigation of depth-dependency between estimated aftershock properties triggered by the strike slip events and tomographic inversions of the region.

- Seismicity in crustal volumes is non-uniform, due to the crustal inhomogeneity, changes of the material properties with depth and plate interaction. Therefore the development of a 3D-ETAS model would be very useful for better understanding of aftershock properties in the vicinity of the mainshock fault and at some distance

from it (for example, the reactivation of crustal activity above mainshock rupture plane in the subduction zone).

- Tectonic loading leads to background events triggering. Large background events can significantly change the stress level in the medium, which leads (a) to aftershock triggering and (b) to medium relaxation. However, it is still remains unclear, if the rate and style of tectonic loading plays a direct role for these two process as well. In particular one specific question about relation between aftershock duration and tectonic loading rate might be addressed in the future studies.

BIBLIOGRAPHY

Agurto, H., A. Rietbrock, I. Ryder, and M. Miller (2012), Seismic-afterslip characterization of the 2010 M W 8.8 Maule, Chile, earthquake based on moment tensor inversion, *Geophysical Research Letters*, *39*(20), n/a–n/a, doi: 10.1029/2012GL053434.

Aki, K. (1965), Maximum likelihood estimate of b in the formula log N=a-bM and its confidence limits, *Bull. Earthquake Res. Inst Univ. Tokyo*, *43*, 237–239.

Aron, F., J. Cembrano, F. Astudillo, R. W. Allmendinger, and G. Arancibia (2014), Constructing forearc architecture over megathrust seismic cycles: Geological snapshots from the Maule earthquake region, Chile, *Geological Society of America Bulletin*, *127*(3-4), 464–479, doi: 10.1130/B31125.1.

Asano, Y., T. Saito, Y. Ito, K. Shiomi, and H. Hirose (2011), Spatial distribution and focal mechanisms of aftershocks of the 2011 off the Pacific coast of Tohoku Earthquake, *Earth, Planets and Space*, *63*(7), 669–673, doi: 10.5047/eps.2011.06.016.

Bath, M. (1965), Lateral inhomogeneities of the upper mantle, *2*(d), 483–514.

Bedford, J., M. Moreno, J. C. Baez, D. Lange, F. Tilmann, M. Rosenau, O. Heidbach, O. Oncken, M. Bartsch, A. Rietbrock, A. Tassara, M. Bevis, and C. Vigny (2013), A high-resolution, time-variable afterslip model for the 2010 Maule Mw = 8.8, Chile megathrust earthquake, *Earth and Planetary Science Letters*, *383*, 26–36, doi: 10.1016/j.epsl.2013.09.020.

Behn, M. D., M. S. Boettcher, and G. Hirth (2007), Thermal structure of oceanic transform faults, *Geology*, *35*(4), 307–310, doi: 10.1130/G23112A.1.

Bräuer, K., H. Kämpf, U. Koch, S. Niedermann, and G. Strauch (2007), Seismically induced changes of the fluid signature detected by a multi-isotope approach (He, CO2, CH4, N2) at the Wettinquelle, Bad Brambach (central Europe), *Journal of Geophysical Research: Solid Earth*, *112*(4), doi: 10.1029/2006JB004404.

Burnham, K., and D. Anderson (2002), *Model Selection and Miltimodel Inference: A Practical Infromation-Theoretic Approach*, paragraph 6.4.5 pp., Springer-Verlag NewYork, Berlin, Heidelberg.

Cattania, C., S. Hainzl, L. Wang, F. Roth, and B. Enescu (2014), Propagation of Coulomb stress uncertainties in physics-based aftershock models, *Journal of Geophysical Research: Solid Earth*, pp. 1–19, doi: 10.1002/2014JB011183.Received.

Cattania, C., S. Hainzl, L. Wang, B. Enescu, and F. Roth (2015), Aftershock triggering by postseismic stresses : A study based on Coulomb rate-and-state models, *Journal of Geophysical Research: Solid Earth*, pp. 1–20, doi: 10.1002/2014JB011500.The.

Cheloni, D., N. D'Agostino, and G. Selvaggi (2014), Interseismic coupling, seismic potential, and earthquake recurrence on the southern front of the Eastern Alps (NE Italy), *Journal of Geophysical Research: Solid Earth*, *119*(Figure 1), 4448–4468, doi: 10.1002/2014JB010954.

Chlieh, M., H. Perfettini, H. Tavera, J.-P. Avouac, D. Remy, J.-M. Nocquet, F. Rolandone, F. Bondoux, G. Gabalda, and S. Bonvalot (2011), Interseismic coupling and seismic potential along the Central Andes subduction zone, *Journal of Geophysical Research*, *116*(B12), B12,405, doi: 10.1029/2010JB008166.

Christophersen, A., and E. G. C. Smith (2008), Foreshock rates from aftershock abundance, *Bulletin of the Seismological Society of America*, *98*(5), 2133–2148, doi: 10.1785/0120060143.

Console, R. (2003), Båth's law and the self-similarity of earthquakes, *Journal of Geophysical Research*, *108*(B2), 2128, doi: 10.1029/2001JB001651.

Dahm, T., T. Fischer, and S. Hainzl (2008), Mechanical intrusion models and their implications for the possibility of magma-driven swarms in NW Bohemia Region, *Studia Geophysica et Geodaetica*, *52*, 529–548, doi: 10.1007/s11200-008-0036-9.

Dahm, T., D. Becker, M. Bischoff, S. Cesca, B. Dost, R. Fritschen, S. Hainzl, C. D. Klose, D. Kühn, S. Lasocki, T. Meier, M. Ohrnberger, E. Rivalta, U. Wegler, and S. Husen (2012), Recommendation for the discrimination of human-related and natural seismicity, *Journal of Seismology*, *17*(1), 197–202, doi: 10.1007/s10950-012-9295-6.

Das, S., and C. Henry (2003), Spatial relation between main earthquake slip and its aftershock distribution, *Reviews of Geophysics*, *41*(3), 1013, doi: 10.1029/2002RG000119.

Dieterich, J. (1994), A constitutive law for rate of earthquake production and its application to earthquake clustering, *Journal of Geophysical Research*, *99*(B2), 2601–2618.

Dieterich, J., V. Cayol, and P. Okubo (2000), The use of earthquake rate changes as a stress meter at Kilauea volcano., *Nature*, *408*(6811), 457–60, doi: 10.1038/35044054.

Ekström, G., M. Nettles, and A. Dziewonski (2012), The global CMT project 2004-2010: Centroid-moment tensors for 13,017 earthquakes, *Physics of the Earth and Planetary Interiors*, *200-201*, 1–9, doi: 10.1016/j.pepi.2012.04.002.

Enescu, B., J. Mori, M. Miyazawa, and Y. Kano (2009), Omori-Utsu Law c-Values Associated with Recent Moderate Earthquakes in Japan, *Bulletin of the Seismological Society of America*, *99*(2A), 884–891, doi: 10.1785/0120080211.

Eneva, M., and G. L. Pavlis (1991), Spatial distribution of aftershocks and background seismicity in central California, *Pure and Applied Geophysics PAGEOPH*, *137*(1-2), 35–61, doi: 10.1007/BF00876888.

Farías, M., D. Comte, S. Roecker, D. Carrizo, and M. Pardo (2011), Crustal extensional faulting triggered by the 2010 Chilean earthquake: The Pichilemu Seismic Sequence, *Tectonics*, *30*(6), 1–11, doi: 10.1029/2011TC002888.

Felzer, K. R., and E. E. Brodsky (2010), Decay of aftershock density with distance does not indicate triggering by dynamic stress., *Nature*, *467*(7315), 583–586, doi: 10.1038/nature09402.

Felzer, K. R., T. W. Becker, R. E. Abercrombie, G. Ekström, and J. R. Rice (2002), Triggering of the 1999 M W 7.1 Hector Mine earthquake by aftershocks of the 1992 M W 7.3 Landers earthquake, *Journal of Geophysical Research*, *107*(B9), 2190, doi: 10.1029/2001JB000911.

Gutenberg, B., and C. F. Richter (1944), Frequence of earthquakes in California, *BSSA*, *34*, 185–188.

Hainzl, S., and T. Fischer (2002), Indications for a successively triggered rupture growth underlying the 2000 earthquake swarm in Vogtland/NW Bohemia, *Journal of Geophysical Research*, *107*(B12), 1–9, doi: 10.1029/2002JB001865.

Hainzl, S., and D. Marsan (2008), Dependence of the Omori-Utsu law parameters on main shock magnitude: Observations and modeling, *Journal of Geophysical Research: Solid Earth*, *113*(B10), B10,309, doi: 10.1029/2007JB005492.

Hainzl, S., and Y. Ogata (2005), Detecting fluid signals in seismicity data through statistical earthquake modeling, *Journal of Geophysical Research*, *110*(B5), B05S07, doi: 10.1029/2004JB003247.

Hainzl, S., G. Zöller, and J. Kurths (1999), Similar power laws for foreshock and aftershock sequences in a spring-block model for earthquakes, *Journal of Geophysical Research*, *104*(B4), 7243, doi: 10.1029/1998JB900122.

Hainzl, S., S. Steacy, and D. Marsan (2010a), Theme V - Models and Techniques for Analyzing Seismicity Seismicity Models Based on Coulomb Stress Calculations, (November), 1–25, doi: 10.5078/corssa-32035809.

Hainzl, S., G. B. Brietzke, and G. Zöller (2010b), Quantitative earthquake forecasts resulting from static stress triggering, *Journal of Geophysical Research*, *115*(B11), B11,311, doi: 10.1029/2010JB007473.

Hainzl, S., Y. Ben-Zion, C. Cattania, and J. Wassermann (2013), Testing atmospheric and tidal earthquake triggering at Mt. Hochstaufen, Germany, *Journal of Geophysical Research: Solid Earth*, *118*(10), 5442–5452, doi: 10.1002/jgrb.50387.

Hainzl, S., J. Moradpour, and J. Davidsen (2014), Static stress triggering explains the empirical aftershock distance decay, *Geophysical Research Letters*, pp. n/a–n/a, doi: 10.1002/2014GL061975.

Hanks, T. C., and H. Kanamori (1979), A moment magnitude scale, *Journal of Geophysical Research B: Solid Earth*, *84*(B5), 2348–2350, doi: 10.1029/JB084iB05p02348.

Harris, R. A. (1998), Introduction to Special Section: Stress Triggers, Stress Shadows, and Implications for Seismic Hazard, *Journal of Geophysical Research*, *103*(B10), 24,347, doi: 10.1029/98JB01576.

Harte, D. S. (2012), Bias in fitting the ETAS model: a case study based on New Zealand seismicity, *Geophysical Journal International*, *192*(1), 390–412, doi: 10.1093/gji/ggs026.

Hasegawa, A., K. Yoshida, and T. Okada (2011), Nearly complete stress drop in the 2011 Mw 9.0 off the Pacific coast of Tohoku Earthquake, *Earth, Planets and Space*, *63*(7), 703–707, doi: 10.5047/eps.2011.06.007.

Hayes, G. P., E. Bergman, K. L. Johnson, H. M. Benz, L. Brown, and A. S. Meltzer (2013), Seismotectonic framework of the 2010 February 27 Mw 8.8 Maule, Chile earthquake sequence, *Geophysical Journal International*, *195*(2), 1034–1051, doi: 10.1093/gji/ggt238.

Helmstetter, A. (2005), Importance of small earthquakes for stress transfers and earthquake triggering, *Journal of Geophysical Research*, *110*(B5), B05S08, doi: 10.1029/2004JB003286.

Helmstetter, A. (2006), Comparison of Short-Term and Time-Independent Earthquake Forecast Models for Southern California, *Bulletin of the Seismological Society of America*, *96*(1), 90–106, doi: 10.1785/0120050067.

Helmstetter, A., and D. Sornette (2003), Båth's law derived from the Gutenberg-Richter law and from aftershock properties, *Geophysical Research Letters*, *30*(20), 2069, doi: 10.1029/2003GL018186.

Hill, D. P., and S. G. Prejean (2007), Treatise on Geophysics, *Treatise on Geophysics*, *4*, 493–525, doi: 10.1016/B978-044452748-6.00046-8.

Hoechner, A., M. Ge, A. Babeyko, and S. Sobolev (2013), Instant tsunami early warning based on real-time GPS - Tohoku 2011 case study, *Natural Hazards and Earth System Sciences*, doi: 10.5194/nhess.

Holschneider, M., C. Narteau, P. Shebalin, Z. Peng, and D. Schorlemmer (2012), Bayesian analysis of the modified Omori law, *Journal of Geophysical Research*, *117*(B6), B06,317, doi: 10.1029/2011JB009054.

Holtkamp, S. G., and M. R. Brudzinski (2011), Earthquake swarms in circum-Pacific subduction zones, *Earth and Planetary Science Letters*, *305*(1-2), 215–225, doi: 10.1016/j.epsl.2011.03.004.

Ide, S., A. Baltay, and G. C. Beroza (2011), Shallow dynamic overshoot and energetic deep rupture in the 2011 Mw 9.0 Tohoku-Oki earthquake., *Science (New York, N.Y.)*, *332*(6036), 1426–9, doi: 10.1126/science.1207020.

Imanishi, K., R. Ando, and Y. Kuwahara (2012), Unusual shallow normal-faulting earthquake sequence in compressional northeast Japan activated after the 2011 off the Pacific coast of Tohoku earthquake, *Geophysical Research Letters*, *39*(9), 1–7, doi: 10.1029/2012GL051491.

Kagan, Y. Y. (2004), Short-term properties of earthquake catalogs and models of earthquake source, *Bulletin of the Seismological Society of America*, *94*(4), 1207–1228, doi: 10.1785/012003098.

Kagan, Y. Y., and D. D. Jackson (2000), Probabilistic forecasting of earthquakes, *Geophysical Journal International*, *143*(2), 438–453, doi: 10.1046/j.1365-246X.2000.01267.x.

Kato, A., S. Sakai, and K. Obara (2011), A normal-faulting seismic sequence triggered by the 2011 off the Pacific coast of Tohoku Earthquake: Wholesale stress regime changes in the upper plate, *Earth, Planets and Space*, *63*(7), 745–748, doi: 10.5047/eps.2011.06.014.

King, G., C. King, R. S. Stein, and J. Lin (1994), Static Stress Changes and the Triggering of Earthquakes, *Bulletin of the Seismological Society of America*, *84*(3), 935–953, doi: 10.1016/0148-9062(95)94484-2.

King, G. C. P. (2007), Fault Interaction , Earthquake Stress Changes , and the Evolution of Seismicity, *Treatise on Geophysics, Earthquake Seismology*, *4*, 225–255.

Lange, D., F. Tilmann, S. E. Barrientos, E. Contreras-Reyes, P. Methe, M. Moreno, B. Heit, H. Agurto, P. Bernard, J.-P. Vilotte, and S. Beck (2012), Aftershock seismicity of the 27 February 2010 Mw 8.8 Maule earthquake rupture zone, *Earth and Planetary Science Letters*, *317-318*(February 2010), 413–425, doi: 10.1016/j.epsl.2011.11.034.

Lange, D., J. R. Bedford, M. Moreno, F. Tilmann, J. C. Baez, M. Bevis, and F. Kruger (2014), Comparison of postseismic afterslip models with aftershock seismicity for three subduction-zone earthquakes: Nias 2005, Maule 2010 and Tohoku 2011, *Geophysical Journal International*, *199*(2), 784–799, doi: 10.1093/gji/ggu292.

Legrand, D., A. Tassara, and D. Morales (2012), Megathrust asperities and clusters of slab dehydration identified by spatiotemporal characterization of seismicity below the Andean margin, *Geophysical Journal International*, *191*, 923–931, doi: 10.1111/j.1365-246X.2012.05682.x.

Lei, X., G. Yu, S. Ma, X. Wen, and Q. Wang (2008), Earthquakes induced by water injection at ∼3 km depth within the Rongchang gas field, Chongqing, China, *Journal of Geophysical Research: Solid Earth*, *113*(10), 1–12, doi: 10.1029/2008JB005604.

Lei, X., S. Ma, W. Chen, C. Pang, J. Zeng, and B. Jiang (2013), A detailed view of the injection-induced seismicity in a natural gas reservoir in Zigong, southwestern Sichuan Basin, China, *Journal of Geophysical Research: Solid Earth*, *118*(8), 4296–4311, doi: 10.1002/jgrb.50310.

Lengliné, O., B. Enescu, Z. Peng, and K. Shiomi (2012), Decay and expansion of the early aftershock activity following the 2011, M w9.0 Tohoku earthquake, *Geophysical Research Letters*, *39*(17), 6–11, doi: 10.1029/2012GL052797.

Lieser, K., I. Grevemeyer, D. Lange, E. Flueh, F. Tilmann, and E. Contreras-Reyes (2014), Splay fault activity revealed by aftershocks of the 2010 Mw8.8 Maule earthquake, central Chile, *Geology*, *42*(9), 823–826, doi: 10.1130/G35848.1.

Lippiello, E., L. De Arcangelis, and C. Godano (2009), Role of static stress diffusion in the spatiotemporal organization of aftershocks, *Physical Review Letters*, *103*(3), 2–5, doi: 10.1103/PhysRevLett.103.038501.

Lombardi, A. M., W. Marzocchi, and J. Selva (2006), Exploring the evolution of a volcanic seismic swarm: The case of the 2000 Izu Islands swarm, *Geophysical Research Letters*, *33*(7), 2–5, doi: 10.1029/2005GL025157.

Lorito, S., F. Romano, S. Atzori, X. Tong, A. Avallone, J. McCloskey, M. Cocco, E. Boschi, and A. Piatanesi (2011), Limited overlap between the seismic gap and coseismic slip of the great 2010 Chile earthquake, *Nature Geoscience*, *4*(3), 173–177, doi: 10.1038/ngeo1073.

Loveless, J. P., and B. J. Meade (2011), Spatial correlation of interseismic coupling and coseismic rupture extent of the 2011 Mw = 9.0 Tohoku-oki earthquake, *Geophysical Research Letters*, *38*(17), n/a–n/a, doi: 10.1029/2011GL048561.

Luttrell, K. M., X. Tong, D. T. Sandwell, B. A. Brooks, and M. G. Bevis (2011), Estimates of stress drop and crustal tectonic stress from the 27 February 2010 Maule, Chile, earthquake: Implications for fault strength, *Journal of Geophysical Research*, *116*(B11), B11,401, doi: 10.1029/2011JB008509.

Marsan, D., and O. Lengliné (2008), Extending earthquakes' reach through cascading., *Science (New York, N.Y.)*, *319*(5866), 1076–1079, doi: 10.1126/science.1148783.

Marsan, D., and O. Lengliné (2010), A new estimation of the decay of aftershock density with distance to the mainshock, *Journal of Geophysical Research: Solid Earth*, *115*(9), 1–16, doi: 10.1029/2009JB007119.

Marsan, D., E. Prono, and A. Helmstetter (2013), Monitoring Aseismic Forcing in Fault Zones Using Earthquake Time Series, *Bulletin of the Seismological Society of America*, *103*(1), 169–179, doi: 10.1785/0120110304.

Marzocchi, W., and L. Sandri (2003), A review and new insights on the estimation of the b -value and its uncertainty, *Annals of Geophysics*, *46*(December).

Marzocchi, W., M. Murru, A. M. Lombardi, G. Falcone, and R. Console (2012), Daily earthquake forecasts during the May-June 2012 Emilia earthquake sequence (northern Italy), *Annals of Geophysics*, *55*(4), 561–567, doi: 10.4401/ag-6161.

McGarr, A. (2014), Journal of Geophysical Research: Solid Earth, *Journal of Geophysical Research: Solid Earth*, pp. 1–12, doi: 10.1002/2013JB010597.Received.

McGuire, J. J., M. S. Boettcher, and T. H. Jordan (2005), Foreshock sequences and short-term earthquake predictability on East Pacific Rise transform faults., *Nature*, *434*(7032), 457–461, doi: 10.1038/nature03621.

Melnick, D., B. Bookhagen, H. P. Echtler, and M. R. Strecker (2006), Coastal deformation and great subduction earthquakes, Isla Santa María, Chile (37° S), *Bulletin of the Geological Society of America*, *118*(11-12), 1463–1480, doi: 10.1130/B25865.1.

Melnick, D., M. Moreno, M. Motagh, M. Cisternas, and R. L. Wesson (2012), Splay fault slip during the Mw8.8 2010 Maule Chile earthquake, *Geology*, *40*(3), 251–254, doi: 10.1130/G32712.1.

Mignan, A., and J. Woessner (2012), Theme IV - Understanding Seismicity Catalogs and their Problems Estimating the magnitude of completeness for earthquake catalogs, (April), doi: 10.5078/corssa-00180805.

Mignan, A., M. J. Werner, S. Wiemer, C.-C. Chen, and Y.-M. Wu (2011), Bayesian Estimation of the Spatially Varying Completeness Magnitude of Earthquake Catalogs, *Bulletin of the Seismological Society of America*, *101*(3), 1371–1385, doi: 10.1785/0120100223.

Miller, S. a., C. Collettini, L. Chiaraluce, M. Cocco, M. Barchi, and B. J. P. Kaus (2004), Aftershocks driven by a high-pressure CO2 source at depth., *Nature*, *427*(6976), 724–727, doi: 10.1038/nature02251.

Mogi, K. (1962), Magnitude-frequency relation for elastic shocks accompanying fractures of various materials and some related problems in earthquakes., *Bull. Earthquake Res. Inst.*, *40*, 831–853.

Moradpour, J., S. Hainzl, and J. Davidsen (2014), Nontrivial decay of aftershock density with distance in Southern California, *Journal of Geophysical Research: Solid Earth*, *119*(7), 5518–5535, doi: 10.1002/2014JB010940.

Moreno, M., M. Rosenau, and O. Oncken (2010), 2010 Maule earthquake slip correlates with pre-seismic locking of Andean subduction zone., *Nature*, *467*(7312), 198–202, doi: 10.1038/nature09349.

Moreno, M., D. Melnick, M. Rosenau, J. Bolte, J. Klotz, H. Echtler, J. Baez, K. Bataille, J. Chen, M. Bevis, H. Hase, and O. Oncken (2011), Heterogeneous plate locking in the South-Central Chile subduction zone: Building up the next great earthquake, *Earth and Planetary Science Letters*, *305*(3-4), 413–424, doi: 10.1016/j.epsl.2011.03.025.

Moreno, M., D. Melnick, M. Rosenau, J. Baez, J. Klotz, O. Oncken, A. Tassara, J. Chen, K. Bataille, M. Bevis, A. Socquet, J. Bolte, C. Vigny, B. Brooks, I. Ryder, V. Grund, B. Smalley, D. Carrizo, M. Bartsch, and H. Hase (2012), Toward understanding tectonic control on the Mw 8.8 2010 Maule Chile earthquake, *Earth and Planetary Science Letters*, *321-322*, 152–165, doi: 10.1016/j.epsl.2012.01.006.

Morgan, M. G., and M. Henrion (1990), *Uncertainty: a guide to dealing with uncertainty in quantitative risk and policy analysis.*, 332 pp., Cambridge Univercity Press.

Narteau, C., S. Byrdina, P. Shebalin, and D. Schorlemmer (2009), Common dependence on stress for the two fundamental laws of statistical seismology., *Nature*, *462*(7273), 642–5, doi: 10.1038/nature08553.

Ogata, Y. (1983), Estimation of the parameters in the modified omori formula for aftershock frequencies by the maximum likelihood procedure., *Journal of Physics of the Earth*, *31*(2), 115–124, doi: 10.4294/jpe1952.31.115.

Ogata, Y. (1988), Statistical Models for Earthquake Occurrences and Residula Analysis for Point Processes, *Jornal of American Statistical Association*, *83*(401), 9–27.

Ogata, Y. (1992), Detection of precursory relative quiescence before great earthquakes through a statistical model, *Journal of Geophysical Research*, *97*(B13), 19,845, doi: 10.1029/92JB00708.

Ogata, Y. (1998), Space-time point-process models for earthquake occurrences, *Ann. Inst. Statist. Math.*, *50*(2), 379–402.

Ogata, Y. (2011), Significant improvements of the space-time ETAS model for forecasting of accurate baseline seismicity, *Earth, Planets and Space*, *63*(3), 217–229, doi: 10.5047/eps.2010.09.001.

Parotidis, M. (2003), Pore-pressure diffusion: A possible triggering mechanism for the earthquake swarms 2000 in Vogtland/NW-Bohemia, central Europe, *Geophysical Research Letters*, *30*(20), 10–13, doi: 10.1029/2003GL018110.

Parsons, T., R. S. Stein, R. W. Simpson, and P. A. Reasenberg (1999), Stress sensitivity of fault seismicity: A comparison between limited-offset oblique and major strike-slip faults, *Journal of Geophysical Research*, *104*(B9), 20,183, doi: 10.1029/1999JB900056.

Passarelli, L., F. Maccaferri, E. Rivalta, T. Dahm, and E. Abebe Boku (2012), A probabilistic approach for the classification of earthquakes as 'triggered' or 'not triggered', *Journal of Seismology*, *17*(1), 165–187, doi: 10.1007/s10950-012-9289-4.

Perfettini, H., and J. P. Avouac (2014), The seismic cycle in the area of the 2011 Mw9.0 Tohoku-Oki earthquake, *Journal of Geophysical Research: Solid Earth*, *119*, doi: 10.1002/2013JB010697.Received.

Press, W. H., S. A. Teukolsky, W. T. Vetterling, and B. P. Flannery (1992), *Numerical Recipes in C: The Art of Scientific Computing.*, 2 ed., Cambridge Univercity Press, New York, NY, USA.

Reasenberg, P. (1985), Second-Order Moment of Central California Seisnicity, 1969-1982, *Journal of Geophysical Research*, *90*(B7), 5479–5495.

Reasenberg, P. a., and R. W. Simpson (1992), Response of regional seismicity to the static stress change produced by the loma prieta earthquake., *Science (New York, N.Y.)*, *255*(5052), 1687–90, doi: 10.1126/science.255.5052.1687.

Reid, H. F. (1910), The mechanics of the earthquake, the California earthquake of April 18, 1906, *Tech. rep.*, Carnegie Institution of Washington, Washington D.C.

Richards-Dinger, K., R. S. Stein, and S. Toda (2010), Decay of aftershock density with distance does not indicate triggering by dynamic stress., *Nature*, *467*(7315), 583–586, doi: 10.1038/nature09402.

Rietbrock, A., I. Ryder, G. Hayes, C. Haberland, D. Comte, S. Roecker, and H. Lyon-Caen (2012), Aftershock seismicity of the 2010 Maule Mw=8.8, Chile, earthquake: Correlation between co-seismic slip models and aftershock distribution?, *Geophysical Research Letters*, *39*(8), n/a–n/a, doi: 10.1029/2012GL051308.

Saito, S. (1992), Stratigraphy of Cenozoic strata in the southern terminus area of Boso Peninsula, Central Japan., *Contributions of Institute of Geology and Paleontology, Tohoku University*, (93), 1–37.

Sawazaki, K., and B. Enescu (2014), Imaging the high-frequency energy radiation process of a mainshock and its early aftershock sequence: The case of the 2008 Iwate-Miyagi Nairiku earthquake, Japan, *Journal of Geophysical Research: Solid Earth*, pp. 5814–5829, doi: 10.1002/2014JB011151.Received.

Schaff, D. P., G. C. Beroza, and B. E. Shaw (1998), Postseismic response of repeating aftershocks, *Geophysical Research Letters*, *25*(24), 4549, doi: 10.1029/1998GL900192.

Scholz, C. H. (1968), The frequency-magnitude relation of microfracturing in rock and its relation to earthquakes., *Bulletin of the seismological society of America*, *58*(1), 399–415.

Scholz, C. H. (2015), On the stress dependence of the earthquake b value, *Geophysical Research Letters*, pp. 1–4, doi: 10.1002/2014GL062863.Received.

Scholz, C. H., and J. Campos (2012), The seismic coupling of subduction zones revisited, *Journal of Geophysical Research*, *117*(B5), B05,310, doi: 10.1029/2011JB009003.

Schorlemmer, D., S. Wiemer, and M. Wyss (2005), Variations in earthquake-size distribution across different stress regimes., *Nature*, *437*(7058), 539–42, doi: 10.1038/nature04094.

Schurr, B., G. Asch, S. Hainzl, J. Bedford, A. Hoechner, M. Palo, R. Wang, M. Moreno, M. Bartsch, Y. Zhang, O. Oncken, F. Tilmann, T. Dahm, P. Victor, S. Barrientos, and J.-P. Vilotte (2014), Gradual unlocking of plate boundary controlled initiation of the 2014 Iquique earthquake, *Nature*, doi: 10.1038/nature13681.

Shao, G., X. Li, C. Ji, and T. Maeda (2011), Focal mechanism and slip history of the 2011 Mw9.1 off the Pacific coast of Tohoku Earthquake, constrained with teleseismic body and surface waves, *Earth, Planets and Space*, *63*(7), 559–564, doi: 10.5047/eps.2011.06.028.

Shearer, P. M. (2012), Space-time clustering of seismicity in California and the distance dependence of earthquake triggering, *Journal of Geophysical Research*, *117*(B10), B10,306, doi: 10.1029/2012JB009471.

Shimojo, K., B. Enescu, Y. Yagi, and T. Takeda (2014), Fluid-driven Seismicity Activation in Northern Nagano Region After the 2011 M9.0 Tohoku-oki Earthquake, *Geophysical Research Letters*, (1), n/a–n/a, doi: 10.1002/2014GL061763.

Shinohara, M., Y. Machida, T. Yamada, K. Nakahigashi, T. Shinbo, K. Mochizuki, Y. Murai, R. Hino, Y. Ito, T. Sato, H. Shiobara, K. Uehira, H. Yakiwara, K. Obana, N. Takahashi, S. Kodaira, K. Hirata, H. Tsushima, and T. Iwasaki (2012), Precise aftershock distribution of the 2011 off the Pacific coast of Tohoku Earthquake revealed by an ocean-bottom seismometer network, *Earth, Planets and Space*, *64*(12), 1137–1148, doi: 10.5047/eps.2012.09.003.

Sornette, D., and M. J. Werener (2005), Constraints on the size of the smallest triggering earthquake from the epidemic-type aftershock sequence model, Båth's law, and observed aftershock sequences, *Journal of Geophysical Research*, *110*(B8), B08,304, doi: 10.1029/2004JB003535.

Steacy, S., J. Gomberg, and M. Cocco (2005), Introduction to special section: Stress transfer, earthquake triggering, and time-dependent seismic hazard, *Journal of Geophysical Research B: Solid Earth*, *110*(5), 1–12, doi: 10.1029/2005JB003692.

Stein, R. S. (1999), The role of stress transfer in earthquake occurrence, *Nature*, *402*, 605–609.

Stein, R. S., G. C. King, and J. Lin (1992), Change in failure stress on the southern san andreas fault system caused by the 1992 magnitude = 7.4 landers earthquake., *Science (New York, N.Y.)*, *258*(5086), 1328–32, doi: 10.1126/science.258.5086.1328.

Stiphout, T. V., J. Zhuang, D. Marsan, S. S. Service, and E. T. H. Zurich (2012), Theme V - Models and Techniques for Analyzing Seismicity Seismicity Declustering, (February), 1–25, doi: 10.5078/corssa-52382934.

Tahir, M., and J.-R. Grasso (2012), Faulting style controls on the Omori law parameters from global earthquake catalogs.

Tahir, M., J.-R. Grasso, and D. Amorèse (2012), The largest aftershock: How strong, how far away, how delayed?, *Geophysical Research Letters*, *39*(4), L04,301, doi: 10.1029/2011GL050604.

Toda, S. (2002), Response of the San Andreas fault to the 1983 Coalinga-Nuñez earthquakes: An application of interaction-based probabilities for Parkfield, *Journal of Geophysical Research*, *107*(B6), doi: 10.1029/2001JB000172.

Toda, S., R. S. Stein, and T. Sagiya (2002), Evidence from the AD 2000 Izu islands earthquake swarm that stressing rate governs seismicity., *Nature*, *419*(6902), 58–61, doi: 10.1038/nature00997.

Tormann, T., B. Enescu, J. Woessner, and S. Wiemer (2015), Randomness of megathrust earthquakes implied by rapid stress recovery after the Japan earthquake, *Nature Geoscience*, *8*(2), 152–158, doi: 10.1038/ngeo2343.

Utsu, T. (1961), A statistical study on the occurence of aftershocks, *Geophys. Mag.*, *30*, 521–605.

Utsu, T. (1966), A statistical significance test of the difference in b-value between two earthquake groups., *Jornal of Physics of the Earth*, *14*, 37–40.

Utsu, T., and A. Seki (1955), Relation between the area of aftershock region and the energy of the mainshock, *Zisin (J. Seism. Soc. Japan)*, *2*(7), 233–240.

Utsu, T., Y. Ogata, and R. S. Matsu'ura (1995), The centenary of the Omori formula for a decay law of aftershock activity, *Jornal of Physics of the Earth*, *43*, 1–33.

Veen, A. (2006), Some Methods of Assessing and Estimating Point Processes Models for Earthquake Occurrences, Ph.D. thesis, University of California.

Vigny, C., a. Socquet, S. Peyrat, J.-C. Ruegg, M. Métois, R. Madariaga, S. Morvan, M. Lancieri, R. Lacassin, J. Campos, D. Carrizo, M. Bejar-Pizarro, S. Barrientos, R. Armijo, C. Aranda, M.-C. Valderas-Bermejo, I. Ortega, F. Bondoux, S. Baize, H. Lyon-Caen, a. Pavez, J. P. Vilotte, M. Bevis, B. Brooks, R. Smalley, H. Parra, J.-C. Baez, M. Blanco, S. Cimbaro, and E. Kendrick (2011), The 2010 Mw 8.8 Maule megathrust earthquake of Central Chile, monitored by GPS., *Science (New York, N.Y.)*, *332*(6036), 1417–21, doi: 10.1126/science.1204132.

Wang, L., J. Liu, J. Zhao, and J. Zhao (2013), Co- and Post- seismic modeling of the 2011 M9 Tohoku-Oki earthquake, and its impact on China mainland., *Earthquake (in Chinise)*, *33*(4), 238–246.

Wang, Q., F. P. Schoenberg, and D. D. Jackson (2010), Standard Errors of Parameter Estimates in the ETAS Model, *Bulletin of the Seismological Society of America*, *100*(5A), 1989–2001, doi: 10.1785/0120100001.

Wei, S., R. Graves, D. Helmberger, J.-P. Avouac, and J. Jiang (2012), Sources of shaking and flooding during the Tohoku-Oki earthquake: A mixture of rupture styles, *Earth and Planetary Science Letters*, *333-334*, 91–100, doi: 10.1016/j.epsl.2012.04.006.

Wells, D. L., and K. J. Coppersmith (1994), New Empirical Relationships among Magnitude, Rupture Length, Rupture Width, Rupture Area, and Surface Displacement, *Bulletin of the seismological society of America*, *84*(4), 974–1002.

Woessner, J., D. Schorlemmer, S. Wiemer, and P. M. Mai (2006), Spatial correlation of aftershock locations and on-fault main shock properties, *Journal of Geophysical Research*, *111*(B8), B08,301, doi: 10.1029/2005JB003961.

Woessner, J., S. Hainzl, W. Marzocchi, M. J. Werner, A. M. Lombardi, F. Catalli, B. Enescu, M. Cocco, M. C. Gerstenberger, and S. Wiemer (2011), A retrospective comparative forecast test on the 1992 Landers sequence, *Journal of Geophysical Research*, *116*(B5), B05,305, doi: 10.1029/2010JB007846.

Yagi, Y., and Y. Fukahata (2011), Rupture process of the 2011 Tohoku-oki earthquake and absolute elastic strain release, *Geophysical Research Letters*, *38*(19), 1–5, doi: 10.1029/2011GL048701.

Yamazaki, Y., T. Lay, K. F. Cheung, H. Yue, and H. Kanamori (2011), Modeling near-field tsunami observations to improve finite-fault slip models for the 11 March 2011 Tohoku earthquake, *Geophysical Research Letters*, *38*(7), n/a–n/a, doi: 10.1029/2011GL049130.

Yue, H., and T. Lay (2013), Source Rupture Models for the Mw 9.0 2011 Tohoku Earthquake from Joint Inversions of High-Rate Geodetic and Seismic Data, *Bulletin of the Seismological Society of America*, *103*(2B), 1242–1255, doi: 10.1785/0120120119.

Zakharova, O., S. Hainzl, and C. Bach (2013), Seismic moment ratio of aftershocks with respect to main shocks, *Journal of Geophysical Research: Solid Earth*, *118*(11), 5856–5864, doi: 10.1002/2013JB010191.

Zhuang, J., D. Harte, M. J. Werner, S. Hainzl, and S. Zhou (2012), Theme V - Models and Techniques for Analyzing Seismicity Basic models of seismicity: Temporal models, doi: 10.5078/corssa-79905851.

APPENDIX A

SLIP AND COUPLING MODELS DERIVED FROM GEODETIC DATA

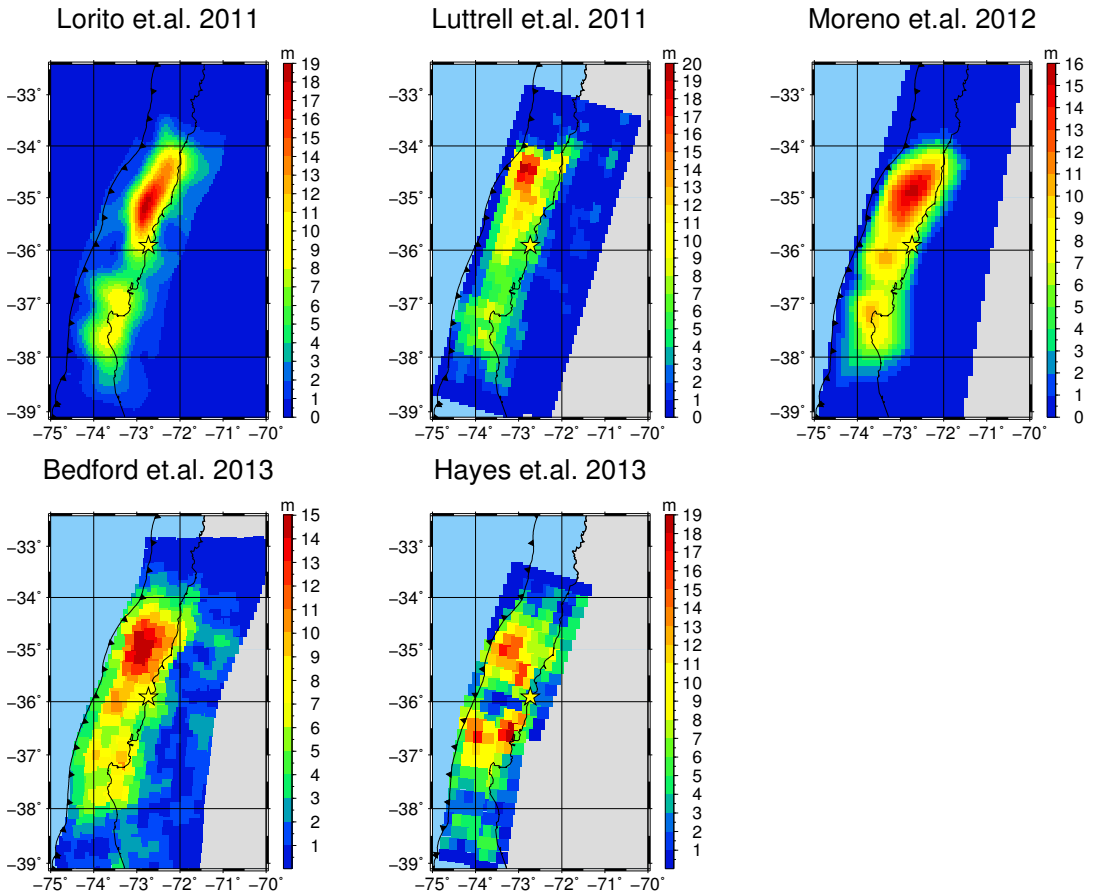

Figure A.1: *The coseismic slip models for the Maule earthquake.*

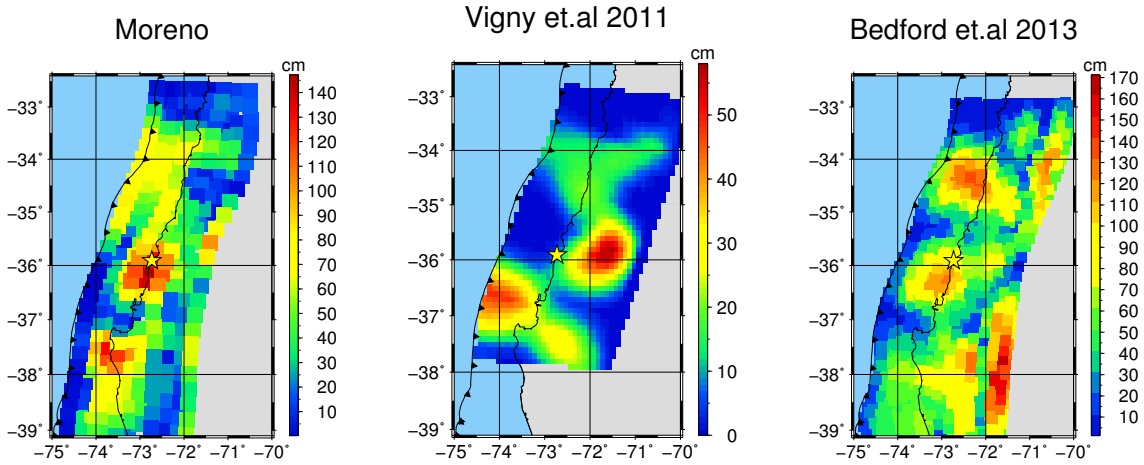

Figure A.2: *The postseismic slip models for the Maule earthquake. The model of Moreno a very early version of the afterslip, the model of Vigny et al. (2011) includes 12 days of GPS observation, meanwhile the model of Bedford et al. (2013) contain an information of one year observations.*

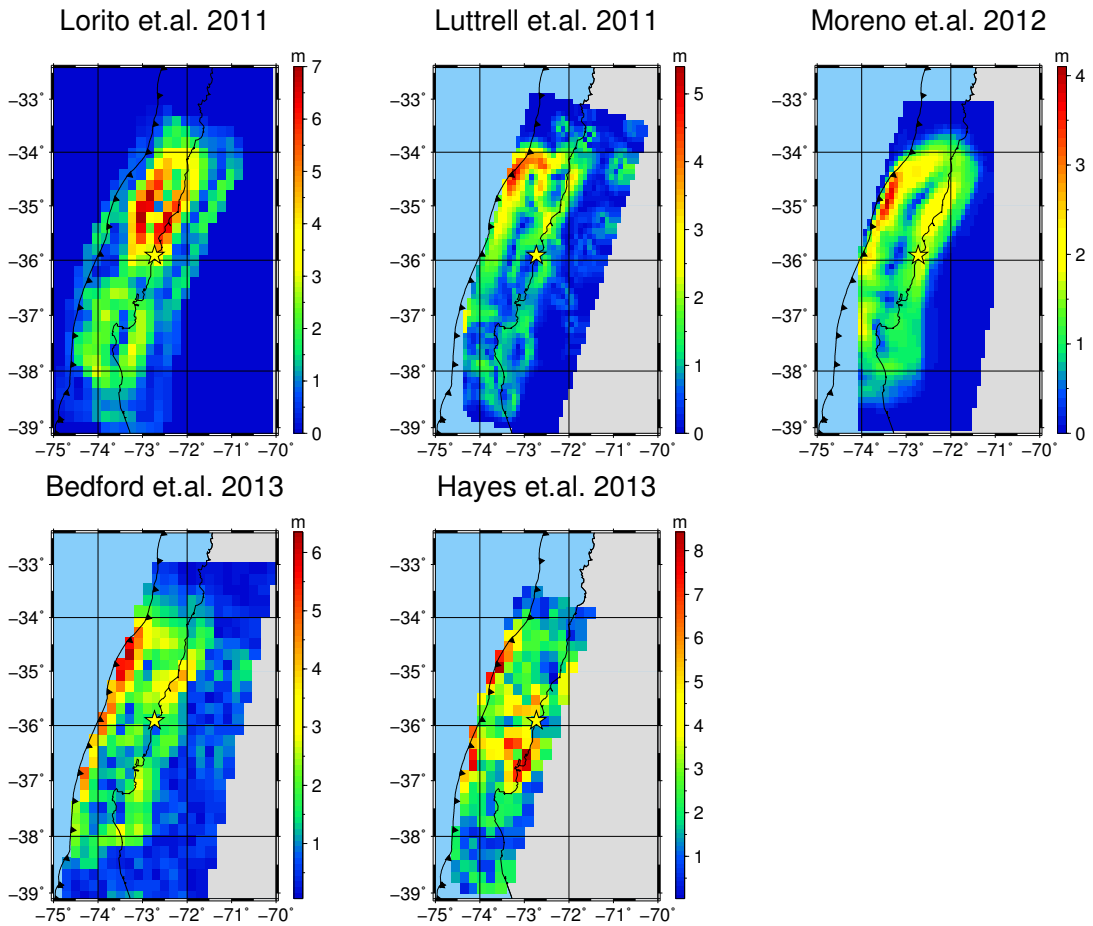

Figure A.3: *The coseismic slip gradient models for the Maule earthquake.*

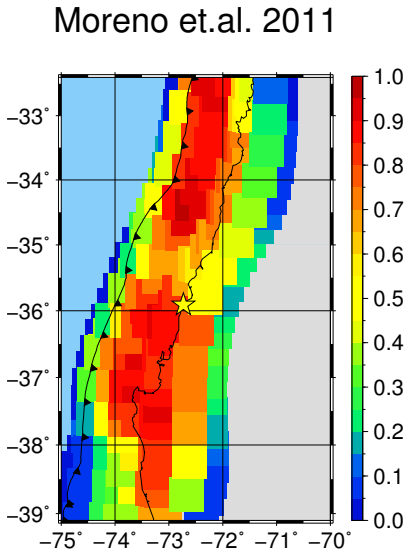

Figure A.4: *The interseismic coupling model of Moreno et al. (2011) for the Maule earthquake area.*

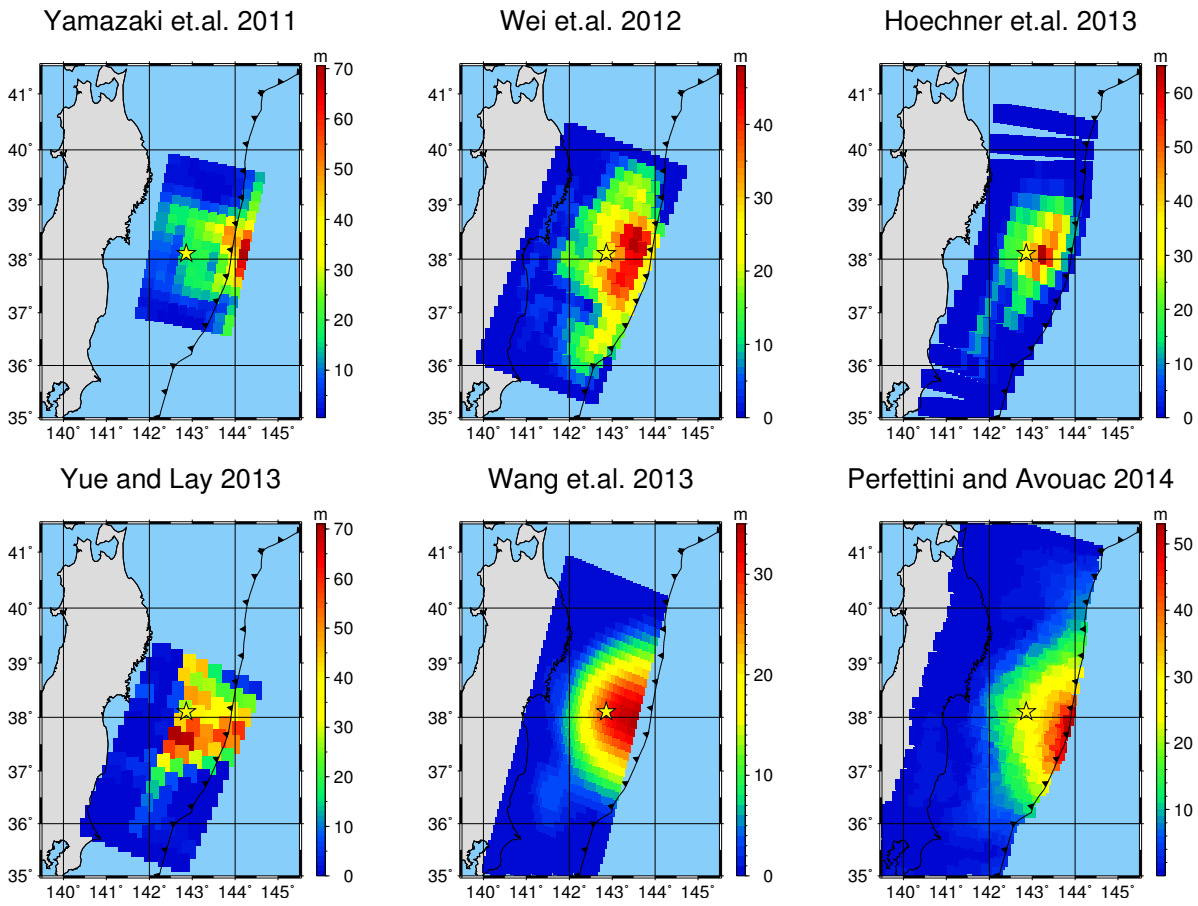

Figure A.5: *The coseismic slip models for the Tohoku-oki earthquake.*

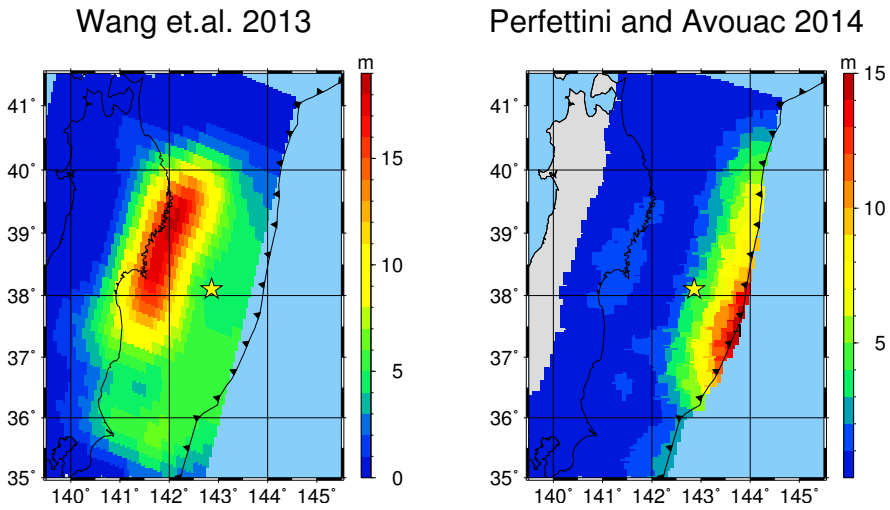

Figure A.6: *The postseismic slip models for the Tohoku-oki earthquake.*

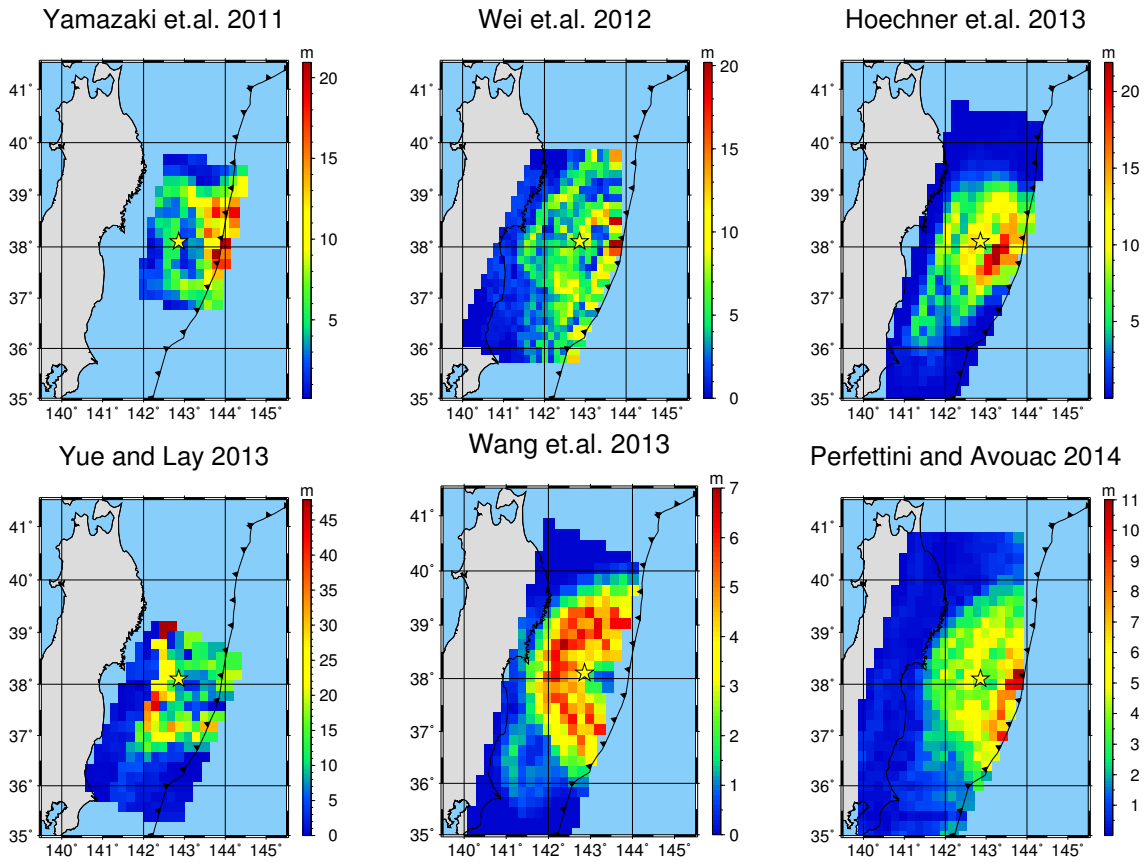

Figure A.7: *The coseismic slip gradient models for the Tohoku-oki earthquake.*

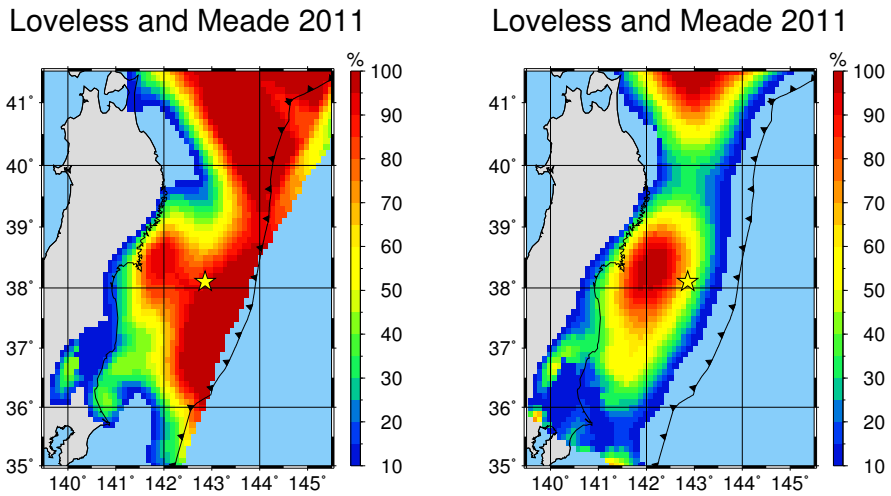

Figure A.8: *The interseismic coupling models of Loveless and Meade (2011) for the Tohoku-oki earthquake region. (1) Free trench; (2) Fixed trench.*

ACKNOWLEDGEMENTS

Financial support for my doctoral study was gratefully received from the graduate research school GeoSim and the University of Potsdam. Additionally, Prof. T. Dahm entrusted me with the invaluable opportunity of an interesting student assistant job funded by the University of Hamburg, which allowed me to learn programming in "Python" and seismic signal processing. Thanks are also to Prof. T. Dahm for a PhD seminar, which helped me to broaden my scientific view in the field of seismology.

I had a great opportunity to share my office with four absolutely different and very unique people: Katrin with her never ending positivity and good mode, Christophchik with his calmness and funny comments on my life attitude, Camilla with her scientific/traveling enthusiasm and her ability to be spontaneous, Flaminia with her very gentle character and self-irony. Moreover, Camilla, Christoph and Katrin helped me to absorb such necessary basics of science, traveling, English/German skills and many other things. I learned from you A LOT!

My working life would not be so amazing without my evening visits of office 112 in House 6 and chats with its inhabitants: Djamil, Marius, Nasim and Nima.

I am also grateful to people of Section 2.1 distributed all over our Helmholzstrasse 6/7 buildings and especially to Michele, Ade, Birger (a friend of all PhD students), Annamaria, Shahid, Alvaro, TB and Kevin.

Greetings from my thesis and thanks for an interesting time and support during my PhD to my close friends outside of the GFZ: Galina, Polina, Antonia, Stephan K., Katja, Mishanya, Janich and Elmira.

Support over the years of my family was important for me! Special thanks go to my MUM, my grandma, my two sisters Katya and Nyusya, aunt Olya, Zhuzhik and Ri!

Finally, I am thankful to my wonderful SUPERvisor, Sebastian Hainzl, who always found time to support me scientifically and psychologically, helped me to significantly improve my writing English and oral German and have never created any pressure for me! The most important thing that I learned from Sebastian is HOW TO BE HAPPY!

All of you helped me (directly or indirectly) to enter an incredible world of science with its probabilistic thinking, technical approaches to problems and, in general, showed me a new side of life, which I did not know before!

HURRAY, MY DEARS!!! I HAVE FINISHED MY THESIS!!!

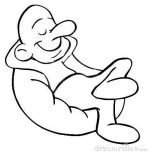

DECLARATION

I herewith declare that the work "Analysis and modeling of transient earthquake patterns and their dependence on local stress regimes" in this present thesis is my own work without any help from third parties and without the use of any aids beyond those given. The thesis consists no material previously published by another person. This work has not been submitted in Germany or abroad to any other examination board in this or similar form.

Potsdam, December 7, 2015

_____

Olga Zakharova